# DIPLOMOVÁ PRÁCE

1998

Tomáš LAŠTOVIČKA

Faculty of Mathematics and Physics
Charles University, Prague
1998


# Analysis of *ep* inelastic scattering registered with the H1 detector at the collider HERA.

Diploma thesis
submitted by

Tomáš Laštovička

Supervisor: Doc. Ing. Josef Žáček, DrSc.

Prohlašuji, že jsem diplomovou práci vypracoval samostatně s použitím uvedené literatury. Souhlasím se zapůjčením diplomové práce.

V Praze, 14.4.1998

# Contents

# Introduction

Most of our knowledge about the structure of matter was obtained by scattering experiments such as the electron-hadron scattering. As stable, charged and point-like objects whose interactions are well understood, electrons are an ideal probe to study more complex objects.

In the late sixties, high energy electron-proton scattering at the Stanford Linear Accelerator Centre (SLAC) provided the first evidence for substructure within the proton [1]. The inelastic cross section was observed to show much weaker dependence on the square of four-momentum transfered ($Q^2$), than the elastic cross section. This was interpreted as the effect of the scattering of the electrons off point-like objects within the proton. These objects were called partons and, in the quark-parton-model (QPM), are identified with quarks carrying spin $\frac{1}{2}\hbar$ and charge equal to multiplies of one third of the elementary charge $e$. Further experiments showed, that the proton consists not only of quarks but also of gluons, which are the exchanged particles of the strong interaction and carry, together with sea quarks, half of the momentum of the nucleon. The proton is conveniently understood in terms of structure functions, which are dependent on the momentum distribution of charged objects within the proton.

The electron proton collider HERA at DESY, Hamburg, is the most recent facility for the study of proton structure. Operational since 1992, HERA is the first accelerator to store beams of electrons and protons, which collide at a very high centre of mass energy allowing the structure of the proton to be studied in entirely new kinematic region, particularly at high $Q^2$ and low $x$, which has been extended by several orders of magnitude with respect to the one reached in previous experiments.

The H1 experiment, the apparatus of which is situated at HERA, was designed to study electron-proton collisions in this new domain. In order to exploit the possible kinematic regions allowed by HERA, the H1 collaboration has upgraded parts of its detector during 1994/95, for example a new backward calorimeter (Spacal) and a drift chamber (BDC) designed to measure scattered electrons with good energy and spatial resolution, down to very small scattering angles. The requirement of a precise calibration of the Spacal calorimeter demands careful checking of behaviour of each cell in the calorimeter during data taking and the accurate re-calibration of all data in the final data reconstruction.

The measurement of the proton structure function $F_2(x, Q^2)$ has already been performed by the H1 collaboration and the gluon density for proton has been determined [2, 3]. The accumulated luminosity for 1997 runs strongly exceeds that from all previous running periods. It is expected that the precision of the determination of $F_2$ from this data will be strongly improved. The aim of the thesis is the extraction of $F_2$ from data which were recorded in 1997. Our results presented in this thesis are preliminary only since they were based on a limited number of preprocessed data and on the Monte Carlo simulations of the H1 detector for 1996 running conditions. During the preparation of this thesis the final data processing and a new simulations have not yet been available.

This thesis is organized as follows: An introduction to the theory of Deep Inelastic Scattering is given in Chapter 1. Chapter 2 describes the HERA accelerator and the H1 detector. A description of the Spacal detector is given in Chapter 3 along with the kinematic peak calibration method and the calibration results. Chapter 4 contains the description of the data treatment. The results of the measurement of the proton structure function $F_2(x, Q^2)$ are presented in Chapter 5.

# Chapter 1

# Physics at HERA

## 1.1 Deep Inelastic Scattering

Deep Inelastic lepton-nucleon Scattering (DIS) has played a dominant role in the understanding of the basic structure of the matter. The scattering amplitude is dominated by the processes shown in Figure 1.1 (a) and (b).

Neutral Current (NC) DIS (Figure 1.1 (a) ) proceeds via the exchange of a neutral electroweak gauge boson between the electron and a quark inside the proton. The exchanged boson is either photon or a $Z^0$ boson. However, since the propagator has a form $1/(Q^2 + M^2)$, where $M$ is the mass of the boson, $Z^0$ contribution to the NC DIS is negligible until the square of four-momentum transfer $Q^2$ approaches the mass of the $Z^0$ squared, i.e. $M^2_{Z^0} \sim 10^4\,\mathrm{GeV}^2$. Indeed, throughout the kinematic region where $Q^2 < 5000\,\mathrm{GeV}^2$, $Z^0$ exchange does not contribute more than 5% to the NC cross section. The high center of mass energy at HERA allows the transferred momentum to be very high, making the weak exchange boson $Z^0$ visible (due to the fact that $Q^2 \geq M^2_{Z^0}$ is achievable) and

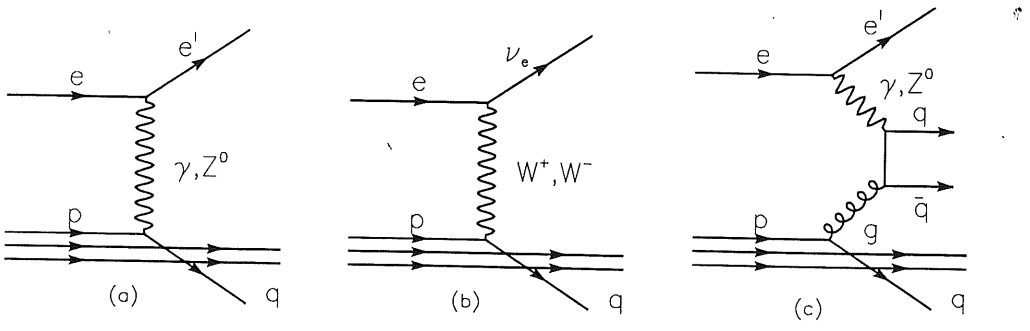


Figure 1.1: Feynmann diagrams for basic $ep$ scattering; (a) NC DIS, (b) CC DIS and (c) gamma($Z^0$)-gluon fusion

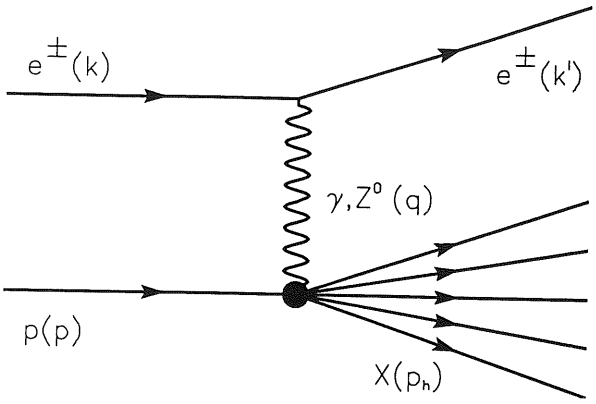


Figure 1.2: Schematic representation of NC $ep$ scattering. The four-momenta of the incoming and scattered lepton are $k$ and $k'$ respectively. The four-momentum of incoming proton is denoted $p$ and the hadronic final state four-momentum is $p_h$. The exchanged boson carries the four-momentum $q$.

resolving structures down to $10^{-18}$ m.[1]

Charged Current (CC) DIS (Figure 1.1 (b)) proceeds via the exchange of a charged boson $W^{\pm}$. The final state neutrino is unobserved. It leads to a characteristic imbalance in the transverse momentum $p_T$ of the final state. This is also a primary hint for separating the CC DIS from the NC DIS. As in the case of $Z_0$ exchange in NC DIS, the $W^{\pm}$ is massive ($M_W^2 \simeq 6400\,\mathrm{GeV}^2$), the propagator suppresses the CC cross section except at very large momentum transfered.

## 1.2 Kinematics of Events

Neutral current DIS process of inclusive electron-proton scattering is illustrated in Figure 1.2 along with definition of kinematic variables.

The event kinematics is unambiguously defined by two of the three Lorentz invariant variables

$$Q^2 = -q^2 = -(k - k')^2 \tag{1.1}$$

$$x = -\frac{q^2}{2p.q} \tag{1.2}$$

$$y = \frac{p.q}{p.k} \tag{1.3}$$

The most common combinations are $(x, y)$ and $(x, Q^2)$. In addition, it is convenient to define following Lorentz invariant variables

$$s = (k + p)^2 \tag{1.4}$$

[1] Corresponds to the square of four-momentum transferred $Q^2 \sim 10^5\,\mathrm{GeV}^2$.

$$W^2 = (q + p)^2 \tag{1.5}$$

The physical interpretation of these variables is the following:

- $Q^2$ - square of the four-momentum transferred, defines the resolution by which the electron probes the structure of the proton
- $x$ - Björken scaling variable, in naive QPM the fraction of the nucleon momentum carried by the struck quark
- $y$ - scaling variable, the fraction of the electron energy lost by the scattering in the proton rest frame
- $s$ - square of the centre of mass energy
- $W$ - total mass of the hadronic final state or invariant mass of the system boson-proton.

Neglecting the masses of particles, the variables are related via the expressions

$$Q^2 = xys \tag{1.6}$$

$$s = 4E_e E_p \tag{1.7}$$

$$W^2 = \frac{1-x}{x} Q^2 \tag{1.8}$$

where $E_e$ and $E_p$ denotes the energies of the incident electron and proton respectively. The beam energies at HERA are $E_e = 27.6\,\text{GeV}$ and $E_p = 820\,\text{GeV}$, therefore the centre of mass energy $\sqrt{s} \simeq 300\,\text{GeV}$. Since $x$ and $y$ acquire values between 0 and 1 the $Q^2$ is limited by the value of $\sim 90000\,\text{GeV}^2$. In the limit of $Q^2 = 0$ the exchanged photon is called *real* and its lifetime becomes infinite.

Kinematical equations can be demonstrated in the $(x, Q^2)$ plane by the isolines of constant electron scattering angle $\theta_e$ and energy $E_e$ as is shown in Figure 1.3 (top left)[2] or by the isolines of constant $y$ (bottom right). The accessible kinematic range is restricted by the condition $0 < y < 1$; the case of $y = 1$ is in the Figure 1.3 represented by the diagonal lines.

## 1.3 Reconstruction of $x$ and $Q^2$

A precise reconstruction of $x$ and $Q^2$ from the final state is essential for structure function measurement at HERA [4]. There is a number of methods for reconstruction of the kinematic variables using both the scattered electron and the hadronic final state.

[2]The angular acceptance of old backward calorimeter BEMC is shown. The new calorimeter Spacal provides wider $\theta$ range up to 177.8°, corresponding to $Q^2$ down to $1\,\text{GeV}^2$.

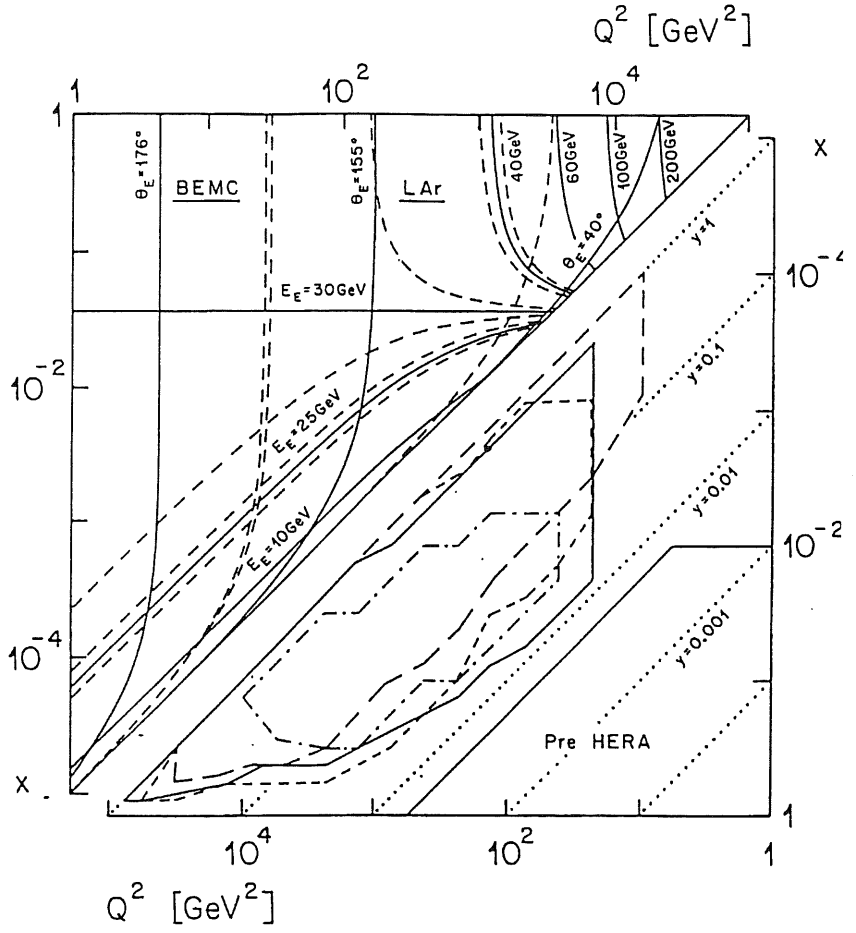


Figure 1.3: The HERA kinematics in the $(x, Q^2)$ plane. Top left: contour plots; bottom right: domains [9].

### 1.3.1 Electron Method

This method is methodically the simplest one. It uses only the energy $E'_e$ and the polar angle $\theta_e$ of the scattered electron. The most strict limit to a precise measurement is coming from the absolute energy calibration. The absolute energy scale must be known at the 1% level in order to assure a systematic shift of the differential cross section smaller than 10% everywhere in the kinematics region. In the case of neglecting both electron and proton masses, the basic formulae are

$$y_e = 1 - \frac{E'_e}{E_e} \sin^2 \frac{\theta_e}{2} \tag{1.9}$$

$$Q^2_e = 4E'_e E_e \cos^2 \frac{\theta_e}{2} = \frac{E'^2_e \sin^2 \theta_e}{1 - y_e}. \tag{1.10}$$

The variable $x$ is calculated as $x_e = Q_e^2/sy_e$ (see Eq.(1.6)). From kinematic equations (1.9),(1.10) we obtain the following relations for measurement errors

$$\frac{\delta Q^2}{Q^2} = \frac{\delta E}{E} \oplus \tan\frac{\theta_e}{2}\delta\theta_e \tag{1.11}$$

$$\frac{\delta x}{x} = \frac{1}{y}\frac{\delta E}{E} \oplus \tan\frac{\theta_e}{2}(x\frac{E_p}{E_e} - 1)\delta\theta \tag{1.12}$$

$$\frac{\delta y}{y} = \frac{1-y}{y}\frac{\delta E}{E} \oplus \frac{1-y}{y}\cot\frac{\theta_e}{2}\delta\theta_e \tag{1.13}$$

The kinematic reconstruction from the electron variables is independent of the hadronic final state. For the $x, Q^2$ measurement the following consequences can be drawn

- the $x$ and $y$ resolutions are poor for low $y$ (due to the factor $1/y$)
- the $Q^2$ resolution is good for most of the HERA kinematic range (except at high $\theta_e$ due to the factor $\tan\theta_e/2$)
- if the effective incoming electron energy is reduced by emission of a real photon the effect is not taken into account in the former equations, leading to a biased event kinematics for this type of events.

### 1.3.2 Hadronic Flow Method

The kinematic variables can be reconstructed from the hadronic final state. A method to determine $x$ and $Q^2$, proposed by A. Blondel and P. Jacquet [5], does not require any jet identification algorithm or proton structure hypothesis. Replacing the momentum transfer $q$ in equation (1.3) by $(p_h - p)$, where the $p_h$ is the four-momentum of the total outgoing hadronic final state, gives

$$y = \frac{p.(p_h - p)}{p.k} \tag{1.14}$$

with

$$p_h = \sum_h (E_h, p_{xh}, p_{yh}, p_{zh}) \tag{1.15}$$

Finally we obtain

$$y_{JB} = \sum_h \frac{E_h - p_{zh}}{2E_e} \tag{1.16}$$

$$Q^2_{JB} = \frac{p_t^2}{1-y} = \frac{(\sum \vec{p_{th}})^2}{1-y} \tag{1.17}$$

where $p_t$ is the total transverse momentum of the hadronic flow and $\vec{p_{th}}$ is the transverse momentum of the hadron $h$. In analogy with the electron method, the variable $x$ is calculated as $x_{JB} = Q^2_{JB}/sy_{JB}$.

It can be seen from the equations (1.16) and (1.17) that the variables $y$ and $Q^2$ defined by J-B method are well tailored for the HERA detectors, because the hadrons emitted into the very forward region contribute only very little to the measured $y, Q^2$.

### 1.3.3 Combined Methods

From the measured energies and angles one can combine another methods of the $Q^2, x, y$ reconstruction, namely the *mixed method* and the *double angle method* which can provide the required precision. Both methods are influenced differently by the detector effects.

The *mixed method* combines the measurement of $Q^2$ from electron method and $y$ by hadronic flow method (Jacquet-Blondel method) and leads to the using of the relations:

$$y_{mix} = y_{JB} \tag{1.18}$$

$$Q^2_{mix} = Q^2_e \tag{1.19}$$

$$x_{mix} = \frac{Q^2_e}{sy_{JB}} \tag{1.20}$$

In the *double angle method* one can make use of both the electron and the hadronic final state angles, i.e. $\theta$ and $\gamma$ respectively. The reconstructed variables are calculated from the following relations:

$$y_{DA} = \frac{\sin\theta(1-\cos\gamma)}{\sin\gamma + \sin\theta - \sin(\theta+\gamma)} \tag{1.21}$$

$$Q^2_{DA} = 4E^2_e \frac{\sin\gamma(1+\cos\theta)}{\sin\gamma + \sin\theta - \sin(\theta+\gamma)} \tag{1.22}$$

$$x_{DA} = \frac{E_e}{E_p} \frac{\sin\gamma + \sin\theta + \sin(\theta+\gamma)}{\sin\gamma + \sin\theta - \sin(\theta+\gamma)} \tag{1.23}$$

This method is rather insensitive to the energy response of the detector and it is widely used for the energy calibration purposes.

## 1.4 Structure Functions

The inclusive cross section of the NC process $ep \to eX$ is given as

$$\sigma \propto L^{\mu\nu} W_{\mu\nu} \tag{1.24}$$

where $L^{\mu\nu}$ is the QED lepton tensor and $W_{\mu\nu}$ is the hadronic tensor, which describes the interaction between the exchanged photon and the proton. Consideration of the requirements of Lorentz invariance and current conservation lead to the following expression:

$$\frac{d^2\sigma}{dxdQ^2} = \frac{4\pi\alpha^2}{xQ^4}[xy^2F_1(x,Q^2)+(1-y)F_2(x,Q^2)+(y-\frac{y^2}{2}xF_3(x,Q^2))], \tag{1.25}$$

where $F_1(x,Q^2)$, $F_2(x,Q^2)$ and $F_3(x,Q^2)$ are structure functions which depend on the momentum distribution of the objects within the proton. A formal derivation of Equation (1.25) can be found in [6]. The third structure function $F_3(x,Q^2)$ represents the parity violating $Z^0$ exchange and is needed for complete description of DIS. Since $Z^0$ contribution is negligible for $Q^2 < 5000\,\mathrm{GeV}^2$ (see Section 1.1) two structure functions are sufficient. Considering the relation $2xF_1 = F_2/(1+R)$ the differential cross section is written as

$$\frac{d^2\sigma}{dxdQ^2} = \frac{4\pi\alpha^2}{xQ^4}[2(1-y)+\frac{y^2}{1+R}]F_2(x,Q^2) \tag{1.26}$$

In order to measure separately $F_2(x,Q^2)$ and $R(x,Q^2)$ it is possible to exploit the different $y$ dependence of their contributions to the cross section to determine the differential cross section at more than one centre of mass energy (at fixed $x$ and $Q^2$; $s$ and therefore $y$ are changed).

It is convenient to introduce so called longitudinal structure function $F_L$ defined as $F_L = 2xF_1 - F_2$ and consequently $R = F_L/(F_2 - F_L)$. In this case the differential cross section is given as follows

$$\frac{d^2\sigma}{dxdQ^2} = \frac{2\pi\alpha^2}{xQ^4}Y_+(F_2 - \frac{y^2}{Y_+}F_L) \qquad Y_+ = 2(1-y)+y^2 \tag{1.27}$$

The DIS experiments at SLAC during the late 1960s [1] observed that structure function $F_2$ showed dependence on $Q^2$ at fixed values of $x$. This behaviour is known as *scaling violations*. In a sufficient approximation $F_2$ is for low $Q^2$ taken to be scale independent. This approach was the basis for the Quark Parton Model (QPM). In the QPM, the proton is considered to be composed of free, point-like fermions, namely quarks, the momentum distributions of which are described by density functions $f_i(x)$. The normalisation of the density functions is given by the momentum sum rule:

$$\sum_i \int_0^1 x f_i(x) dx = 1 \tag{1.28}$$

which sums over all types of quarks, $i$, in the proton. The scattering takes place from point-like objects in the proton, and therefore the parton density functions should depend only on the variable $x$. A relationship between parton density functions and the structure functions can be deduced:

$$F_1 = \frac{1}{2}\sum_i e_i^2 f_i(x) \tag{1.29}$$

$$F_2 = x\sum_i e_i^2 f_i(x) \tag{1.30}$$

where $e_i$ denotes the charge of the $i$-th species of parton. From above equations one can derive the relationship between the structure functions

$$F_2 = 2xF_1 \tag{1.31}$$

which implies $R = 0$ ($F_L = 0$).

## 1.5 $F_2$ Extraction Method

The structure function $F_2$ is defined with respect to the double differential Born cross section (see Eq. (1.26)). The Born cross section is a lowest order in $\alpha_s$ approximation described by the single photon exchange. However, the measured cross section covers contributions to all orders in $\alpha_s$ and therefore the Born cross section is not directly measured. The large corrections originate from bremsstrahlung processes of a real photon from the incident electron. The relation between the measured cross section and $F_2$ can be written as

$$\frac{d^2\sigma}{dxdQ^2} = \kappa(R)\cdot F_2(x,Q^2)\cdot(1+\delta_{RC}(x,Q^2)), \tag{1.32}$$

where $\delta_{RC}$ denotes radiative corrections and $\kappa(R)$ the kinematic factor

$$\kappa(R) = \frac{2\pi\alpha^2}{Q^4 x}\left(2(1-y)+\frac{y^2}{1+R}\right). \tag{1.33}$$

The kinematic factor depends on $R$ and consequently on the longitudinal structure function $F_L$ ($R = F_L/(F_2 - F_L)$, see Section 1.4). At low $y < 0.1$ the influence of $F_L$ is negligible, at medium $y \approx 0.3$ the $F_L$ contribution is comparable to systematic errors of the measurement and at high $y > 0.6$ it is of the order of the $F_2$. In the intermediate $y$ range a standard approach is to assume $F_L$ to be given by a model.

The double differential cross section is calculated mostly in bins of $x$ and $Q^2$, conveniently denoted as $\square_{x,Q^2}$. Then the uncorrected bin integrated cross section is given as follows

$$\sigma^{uncorr.}_{\square_{x,Q^2}} = \int_{\square_{x,Q^2}} \frac{d^2\sigma(x,Q^2)}{dxdQ^2}dxdQ^2 = \frac{N}{\mathcal{L}}, \tag{1.34}$$

where $N$ and $\mathcal{L}$ denote the number of events reconstructed in the bin and the integrated luminosity respectively. The Born cross section is extracted by using a number of corrections, which are included in the following formula

$$\frac{d^2\sigma}{dxdQ^2} = \frac{N_{data} - N_{\gamma p} - N_{pb}}{\mathcal{L}} \frac{1}{A \cdot \epsilon} \frac{1}{1 + \delta_{RC}} \cdot B, \tag{1.35}$$

where

$N_{data}$ Total number of selected events per bin.

$N_{\gamma p}$ Total number of $\gamma p$ background events estimated from the Monte Carlo simulation.

$N_{pb}$ Total number of background events originating from the pilot bunches.[3]

$\mathcal{L}$ Total luminosity corrected for the satellite bunch contribution.

$A$ Monte Carlo calculated detector acceptance. It is defined as the ratio of the number of reconstructed events to the number of generated events in a given bin.

$\epsilon$ Efficiency corrections not included in the Monte Carlo simulation.

$\delta_{RC}$ Already mentioned radiative corrections estimated by simulation.

$B$ The bin center and size correction. The bin size correction transforms the integrated cross section into a bin averaged differential cross section. The bin center correction is needed since the cross section varies inside a given bin. Both corrections are included in the following relation $B = \frac{d^2\sigma}{dxdQ^2} / \sigma^{Born}_{\square_{x,Q^2}}$.

With an assumption that the Monte Carlo simulations of the detector are correct and completely include the radiative corrections, the measurement of $F_2$ in a given bin can be compactly summarised in the following relation

$$F_2(x,Q^2) - YF_L^{MC}(x,Q^2) =$$
$$\frac{N_{data} - N_{\gamma p} - N_{pb}}{N_{MC}} \frac{\mathcal{L}_{MC}}{\mathcal{L}_{data}} \frac{1}{\epsilon} \cdot (F_2^{MC}(x,Q^2) - YF_L^{MC}(x,Q^2)) \tag{1.36}$$

where $(x,Q^2)$ is corresponding to the center of a given bin. $N_{MC}$ is the number of DIS events in the Monte Carlo simulation with the integrated luminosity $\mathcal{L}_{MC}$. Quantity $Y$ is defined as $Y = y^2/Y_+$. The kinematic factors (see. Eq. (1.27)) are canceled. Note that the bin corrections enter the formula in the relation between $F_2^{MC}$ and the expected number of events in a given bin $N_{MC}$.

[3] In the following analysis will not be considered due to an error in DST1 data where the variable distinguishing a type of event was not set correctly.

| Parametrisation of $F_2(x, Q^2)$ (H1, 1993 data) | | | |
|---|---|---|---|
| $F_2 = [a \cdot x^b + c \cdot x^d \cdot (1 + e \cdot \sqrt{x}) \cdot (\ln Q^2 + f \cdot \ln^2 Q^2)] \cdot (1 - x)^g$ | | | |
| $a = 3.07$ | $b = 0.75$ | $c = 0.14$ | $d = -0.19$ |
| $e = -2.93$ | $f = -0.05$ | $g = 3.65$ | |
| Validity: $10^{-4} < x < 1 \ \wedge \ Q^2 < x \cdot 10^5\,\mathrm{GeV}^2 \ \wedge \ 4 < Q^2 < 2000\,\mathrm{GeV}^2$ | | | |

Table 1.1: The $F_2$ structure function parametrisation [7].

It should be emphasized that the correct Monte Carlo simulation is necessary for application of the method above. If the prediction of the model gives a too different results from the measurement obtained from the formula (1.36) an iteration is needed. In this case the QCD fit on the data $F_2$ is performed and accordingly the Monte Carlo events are reweighted. Then the extraction method is used again.

## 1.6 Calibration Influence on $F_2$ measurement

The accuracy of kinematic variables reconstruction is highly dependent on the quality of subdetectors calibration. It turns out that the backward calorimeter Spacal (see Sections 3,4.1) is in the first version of 1997 data undercalibrated by about 2 %.

It could be useful to study shift in $F_2$ measurement as an effect of an error in the determination of scattered electron energy. In presented analysis the bins will be treated as points (infinitely small size). The quantity of interest is the following one

$$\frac{F_2(x_m, Q^2_m)}{F_2^m(x_m, Q^2_m)} = \frac{F_2(x_m, Q^2_m)}{F_2(x, Q^2)} \cdot \frac{F_2(x, Q^2)}{F_2^m(x_m, Q^2_m)}, \tag{1.37}$$

where index $m$ refers to a measured values and quantities without index are taken to be correct. This ratio can be interpreted as a correction factor correcting the $F_2^m$ in a given $(x_m, Q^2_m)$ by multiplication only. Both terms on the right side are calculable. In a good approximation the structure function $F_L$ is for low $x$ negligible. A parametrisation of $F_2$ (see Table 1.1 for details) could be employed to derive the first fraction on the right side, i.e. the ratio of the $F_2$ value in the measured $(x_m, Q^2_m)$ and the 'real' $(x, Q^2)$ coordinates which are related via relations

$$x_m = x \cdot (k \cdot y)/(1 - k \cdot (1 - y)) \qquad Q^2_m = Q^2 \cdot k, \tag{1.38}$$

where $k$ represents the shift of the energy calibration ($k = E_e^m/E_e$). The second term in Eq. (1.37) can be evaluated using the Eq. (1.27) and neglecting $F_L$ for low $x$

$$\frac{F_2(x,Q^2)}{F_2^m(x_m,Q_m^2)} = \frac{xQ^4}{x_mQ_m^4}\,\frac{Y_+^m}{Y_+}\cdot\mathcal{J}, \tag{1.39}$$

where $\mathcal{J}$ denotes the Jacobian of transformation $(x,Q^2)\rightarrow(x_m,Q_m^2)$.

The evaluation of Eq. (1.37) as a function of $Q^2$ is depicted in Figure 1.4 for three values of $x$. For higher values of $x$ and lower values of $Q^2$ the measurement of $F_2$ is more sensitive to shift in electron energy determination. Therefore the requirement of accurate calibration of the backward calorimeter is essential for the structure function measurement. The correct description demands inclusion of the longitudinal structure function and of the corrections for the finite size of bins.

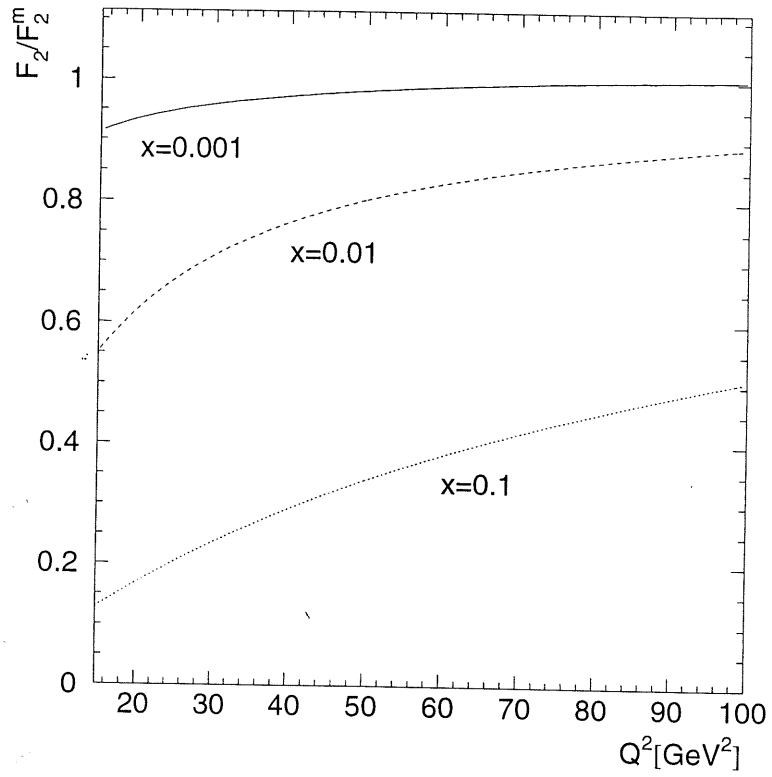


Figure 1.4: The $F_2$ measurement correction factor $(F_2(x_m,Q_m^2)/F_2^m(x_m,Q_m^2))$ caused by -2 % shift in the Spacal calibration.

## 1.7 Gluon Density Determination

In a convenient way the gluon density can be obtained by analysing the longitudinal structure function. In [8] a similar method is applied using the $Q^2$ derivative of $F_2$ to obtain the gluon density to a good accuracy. The main idea is that the scaling violation of $F_2$ for low $x$ arises from the gluon density alone and does not depend on the quark densities. At $x$ below $10^{-2}$ the quarks in Altarelli - Parisi equation can be neglected

$$\frac{dF_2}{d\log Q^2} \approx \frac{5\alpha_s}{9\pi}\int_0^{1-x} G\left(\frac{x}{1-z}\right)\cdot P_{qg}(z)\,dz, \tag{1.40}$$

where in the lowest order

$$P_{qg}(z) = (1-z)^2 + z^2. \tag{1.41}$$

When applying (1.40) there could be a problem with determination of the gluon distribution $G(x)$ ($= xg(x)$, $g$ is the gluon density) over the complete $x$-range. At low $x$ the problem can be avoided by calculating the integral in (1.40) approximately. The gluon distribution is expanded as following

$$G\left(\frac{x}{1-z}\right) \approx G(z=\tfrac{1}{2}) + (z-\tfrac{1}{2})\cdot G'(z=\tfrac{1}{2}) + (z-\tfrac{1}{2})^2\cdot\frac{G''(z=\frac{1}{2})}{2} \tag{1.42}$$

This expression is inserted in (1.40) and the upper integration limit is approximated to 1. The second term in (1.42) vanishes due to the symmetry of $P_{qg}(z)$ around $z = \frac{1}{2}$. The third term gives a small contribution compared to the first one and is neglected. After that one obtains

$$\frac{dF_2}{d\log Q^2}(x) \approx \frac{5\alpha_s}{9\pi} G(2x)\int_0^1 P_{qg}(z)\,dz. \tag{1.43}$$

Latter equation could be evaluated using the leading order for $P_{qg}(z)$

$$\frac{dF_2}{d\log Q^2}(x) \approx \frac{5\alpha_s}{9\pi}\,\frac{2}{3}\,G(2x). \tag{1.44}$$

Below $x = 10^{-3}$ the approximation is good to the level of 10 % [8] and is slightly dependent on the shape of the gluon distribution. This is caused by the fact that the expansion is less accurate at the endpoints of the integration. The effect of $\alpha_s^2$ corrections to $F_2$ on the $Q^2$ derivative of $F_2$ is not more than 5 % at $Q^2 \sim 10 - 50\,\mathrm{GeV}^2$ and $x \sim 10^{-4} - 10^{-3}$ as is noticed in [8]. Total accuracy of gluon density measurement amount to around 20 %, consisting of 5 % uncertainty in the measurement of the $Q^2$-dependence of $F_2$, 10 % for $\alpha_s$, 10 % for neglecting typical low-$x$ effects[4] and 10 % for described approximation.

[4]These effects are calculated beyond the DGLAP approximation, e.g. gluon recombination into quarks and relaxation of the strong ordering of the transverse momenta.

# Chapter 2

# The H1 Detector at HERA

## 2.1 The HERA Accelerator

HERA (Hadron Electron Ring Accelerator) is the first facility to provide colliding beams of electrons and protons. It is designed to accelerate 210 bunches of electrons (or positrons) and 210 bunches of protons to 30 GeV and 820 GeV respectively. Some of those e(p) pilot bunches which pass through the detectors without being collided against p(e) bunches are used for the background and timing studies. Bunches separated by 96 ns are accelerated in two independent storage rings housed in a tunnel of circumference 6.3 km. HERA provides a center of mass energy of 314 GeV (equivalent to a 50 TeV incident electron beam on a fixed target). This provides an extension of two orders of magnitude in the accessible kinematic range in $x$ and $Q^2$ compared to fixed target experiments. The electron and proton bunches are arranged to intersect at four interaction points, which house the H1 (North Hall), ZEUS (South Hall), HERMES (East Hall) and HERA-B (West Hall) experiments. A schematic layout of the HERA facilities at DESY is shown in Figure 2.1.

The positrons from a 500 MeV linear accelerator are injected into a storage ring where they are accumulated and then injected into DESY II synchrotron which increases their energy up to 7 GeV. In the next step they are transferred into the PETRA ring where the energy is raised up to 14 GeV after accumulating up to 70 bunches. Bunches are then injected into HERA accelerator. This was repeated until HERA has been filled with up to 210 bunches of positrons.

A whole new chain of preaccelerators has been built in order to inject protons into HERA. A linear accelerator delivers a 50 MeV negatively charged hydrogen ion beam which is stripped upon entering into the DESY III synchrotron. Inside DESY III the protons are captured into 11 radio frequency buckets with the final bunch spacing and the final total number of particles per bunch, unless losses happen during transfers and ramping. The protons are then accelerated up to 7.5 GeV and transferred to PETRA, which can accumulate up to 70 bunches and

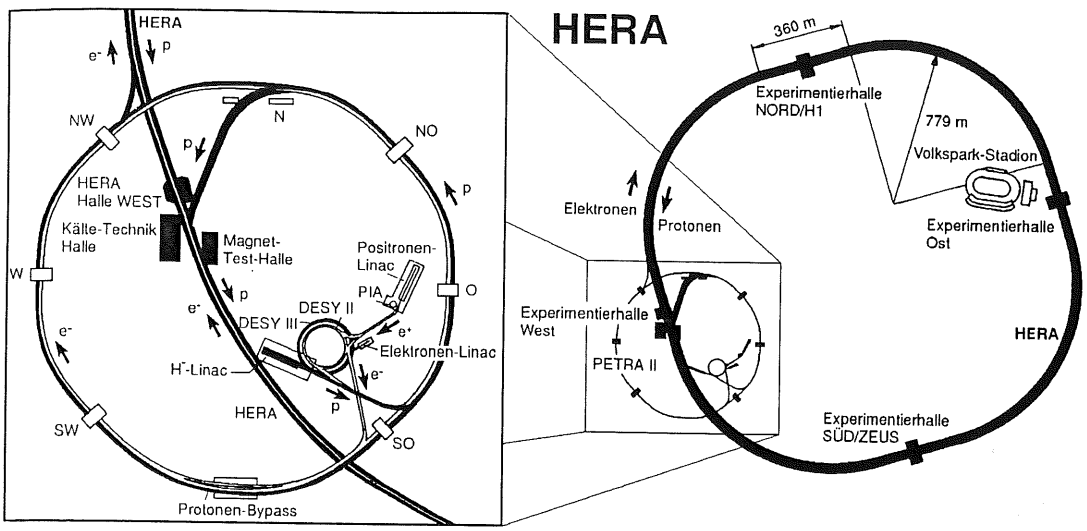


Figure 2.1: The HERA accelerator at DESY and injection system

accelerate them up to 40 GeV. Finally they are transferred into the HERA proton ring.

## 2.2 The H1 Detector

The H1 detector [9] is designed to study many aspects of $ep$ scattering. In order to exploit fully the physics potential of HERA, the detector has to fulfill a number of major roles, which are:

- **Electron detection:** identification and energy measurement of scattered electrons is crucial for the study of NC DIS events, particularly in the backward (electron) direction, where the final state electrons at moderate $Q^2$ are detected.

- **Hadron detection:** calorimetry with fine granularity and good resolution is needed in order to characterize the hadronic final states in many processes.

- **Charged particle tracking:** charged particle momentum measurement and identification is required for the investigation of many processes at HERA. This is provided by tracking detectors covering a large solid angle. A magnetic field curves the tracks and allows the momentum to be determined, while energy loss measurements enable particle identification.

- **Muon identification:** heavy flavour, rare Standard Model and exotic physics processes are detected through the production of muons in the final state.

- **Luminosity measurement:** accurate determination of the luminosity delivered to the experiment is vital for calculation of cross sections.

- **Triggering and readout:** the high bunch crossing rate at HERA and the very high backgrounds from beam-gas and beam-wall interactions means that the detector must be able to identify physics processes from the background, digitize and read out a large number of detector channels ($> 250000$) while minimising dead time. A fast, pipelined, multi-level trigger system, in combination with high-speed digitization and readout, is therefore employed.

The H1 detector is cylindrically symmetric around the beam axis. The event topology requires an asymmetric detector design along the beam axis. It is caused by large imbalance in the energy of the two colliding beams, which boosts the center of mass system along the proton flight direction. Therefore high particle densities and high energies are expected in this direction. The coordinate system of H1 is right handed and defined with the z axis parallel to the proton direction, the y axis vertical and the x axis mutually perpendicular to the others. The origin is defined as the nominal interaction point. The part of the detector situated on the positive side of z axis (relatively to the interaction region) is referred to as the "forward" direction. The negative side, corresponding to the outgoing electron direction, is referred to as the "backward direction".

Figure 2.2 gives an overview of the H1 detector. Starting the description from the interaction point, silicon trackers surround the beam pipe [1] in central and backward region (not shown). The central [2] and forward [3] trackers enclose the central silicon tracker and the beam pipe in the forward region. The Liquid Argon (LAr) electromagnetic [4] and hadronic [5] calorimeters mounted in Liquid Argon cryostat, surrounds the central trackers. The Spacal electromagnetic and hadronic calorimeters [12] are situated in the backward region. A superconducting coil [6] of radius 3m is placed outside the LAr calorimeter and provides an uniform magnetic field of 1.2T. This field is compensated by another superconducting coil [7] in order not to influence the HERA accelerator. The large iron return yoke [10] return the magnetic flux and completes the magnetic circuit of the solenoid. It also serves as a tail catcher to detect hadronic showers not contained by the LAr calorimeter. The muon chambers [9] are used for muon identification. Measurement of muon tracks in the forward region is provided by toroid [11] equipped with drift chambers. The plug calorimeter [13] surrounds the beam pipe in the forward region. The whole detector is shielded by the concrete shielding in order to minimize radiation in the experimental hall. The electron

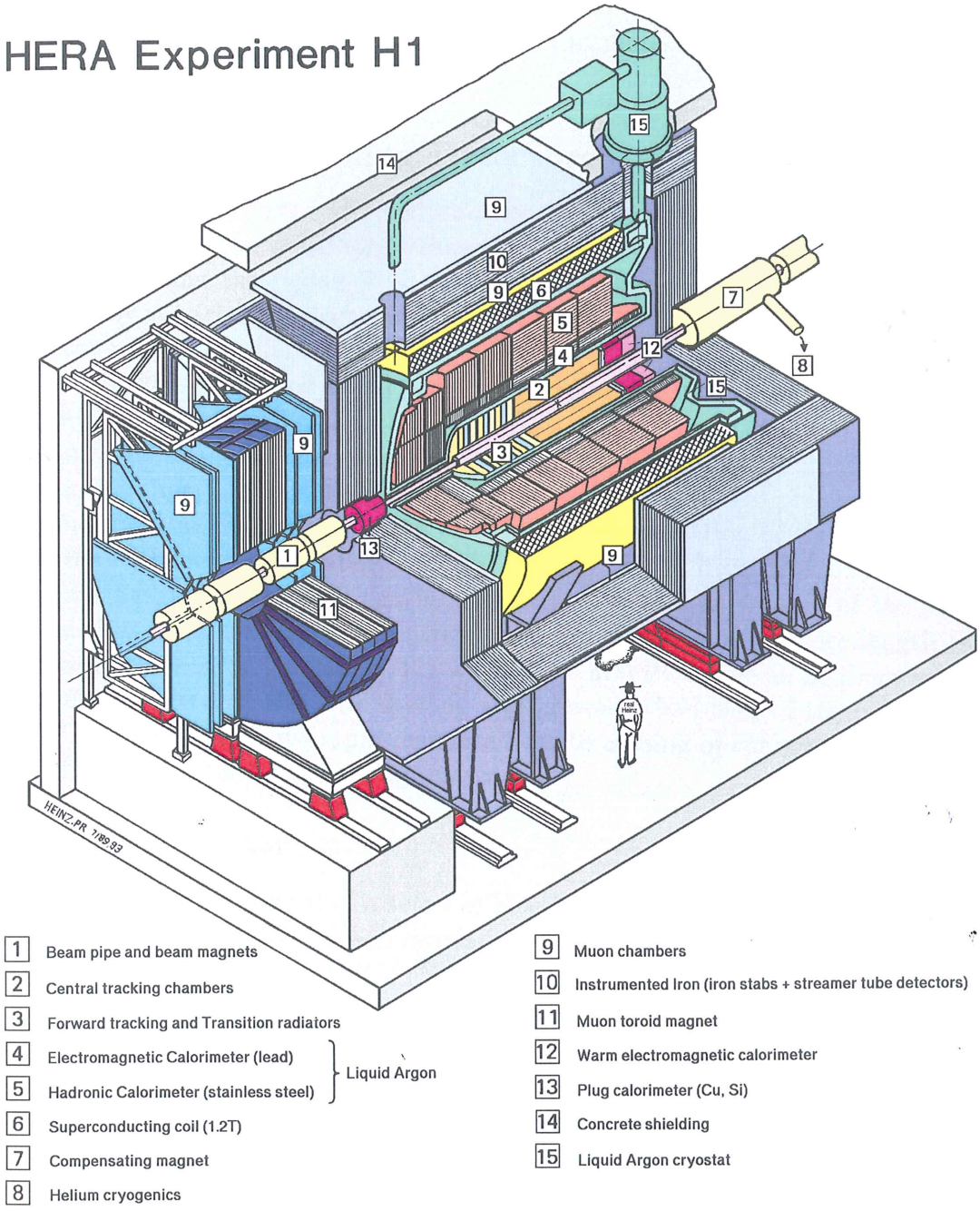


Figure 2.2: The H1 detector

tagger at position $z = -33\,\mathrm{m}$ upstream the interaction point (in HERA tunnel) detects electrons with a very small scattering angle. In conjunction with the photon detector at $z = -102.9\,\mathrm{m}$ it monitors the luminosity by the bremsstrahlung process $ep \to ep\gamma$. This reaction has a well known cross section.

The above components will be described in more detail in the following sections.

### 2.2.1 The H1 Tracking Detectors

The H1 tracking system is divided into two main components; the central tracker (CTD), covering the polar angle range $15° < \theta < 165°$, and the forward tracker (FTD), covering the region $7° < \theta < 25°$. In addition, the backward region is covered by a backward drift chamber (BDC) in front of the Spacal calorimeter and covers the angular range $151° < \theta < 177.5°$. The central and backward silicon trackers (CST and BST) provide precision measurement of tracks close to the interaction point.

Both the central and forward trackers consist of drift and multi-wire proportional chambers (MWPC). The drift chambers are used for precise trajectory measurement of charged particles; enabling a determination of the particle momentum. Hits can be located within $\sim 150\,\mu\mathrm{m}$ in the drift direction. The coordinate parallel to the wire can be determined by charge division of the pulses recorded at each end of the wire, to a precision of $\sim 1\%$ of the wire length (i.e. $\sim 2\,\mathrm{cm}$ in the case of 2 m long CTD wire). The MWPCs have an intrinsic spatial resolution limited by the wire spacing and is worse than that of the drift chambers. However, they have rapid response time to passing of charged particles and therefore are useful for triggering purposes.

#### The Central Tracker

The central tracker consist of a series of interleaved drift chambers and MWPCs. Reconstruction of trajectories in central region is based mainly on two concentric drift chambers, CJC1 and CJC2 (Figure 2.3).

CJCs have drift cells defined by 2200 mm long wires strung parallel to the beam axis and inclined by about 30° with respect to the radial direction, so that the drift direction is approximately perpendicular to high momentum tracks. The chamber has an inner radius 200 mm, an outer radius 795 mm and length 2640 mm centered around the nominal interaction point. The inner chamber, CJC1, has 30 cells with 24 wires each, and the outer chamber, CJC2, has 60 cells with 32 wires each. A spatial resolution of $170\,\mu\mathrm{m}$ in the $r$-$\phi$ plane and 2.2 cm in $z$ has been measured which compares well with the design goals. The particle momentum is reconstructed from the curvature of the track caused by the magnetic field. Chambers allow the measurement of the particle momentum with precision $\sigma_p/p^2 < 0.01\,\mathrm{GeV}^{-1}$. Particle identification is assisted by measurement

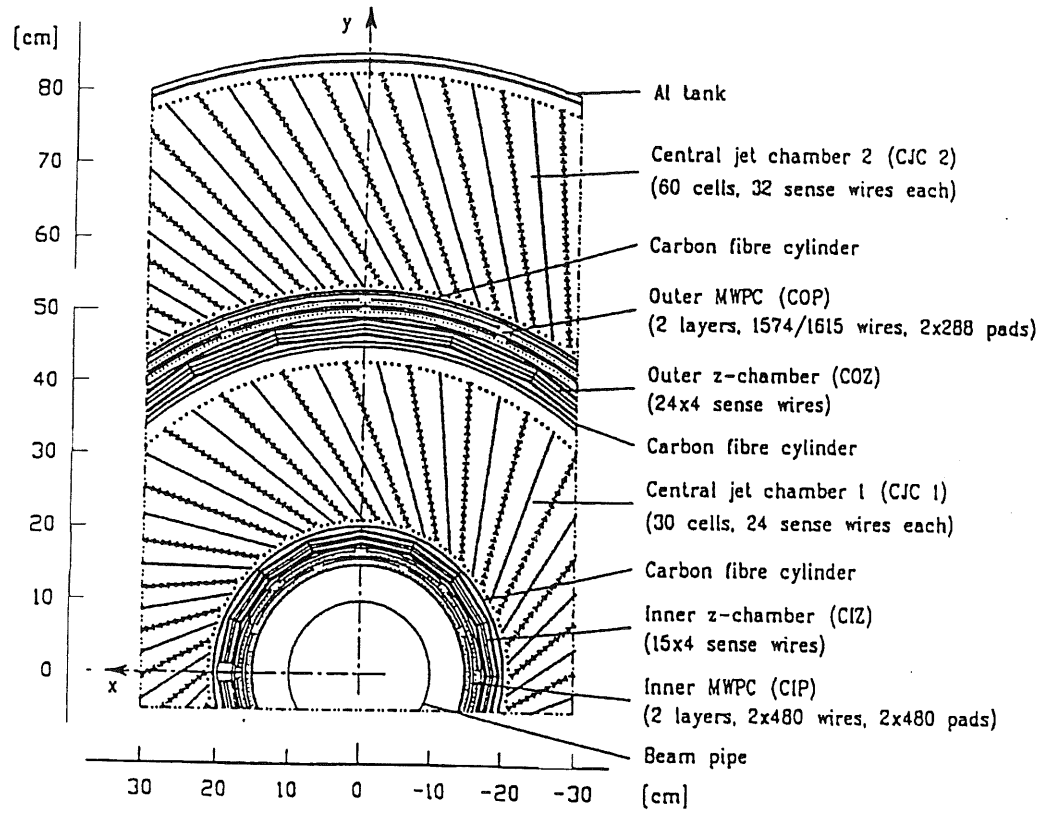


Figure 2.3: Radial view of the central tracker.

of the specific energy loss, $dE/dx$, along the track, with a typical resolution of 10%. The event interaction vertex determination relies essentially on CJC reconstructed tracks.

Two thin drift chambers with wires perpendicular to the beam axis enable a better measurement of the track position in the $z$-coordinate than is possible from charge division of the CJC signals. The inner $z$-chamber (CIZ) is located inside CJC1, and the outer chamber (COZ) lies between CJC1 and CJC2. They provide track elements with typically 300 $\mu$m resolution in $z$ and about 2% in $\phi$.

Linking these track elements to those obtained from the jet chambers gives the design resolution for the momentum of charged tracks $\sigma_p/p^2 \approx 3 \times 10^{-3}\,\mathrm{GeV}^{-1}$ and for the polar angle $\sigma(\theta) \approx 1\,\mathrm{mrad}$.

The MWPC chambers are also included in the central tracker. The inner multiwire proportional chamber (CIP) is closest to the interaction region and is composed of 60 sectors in $z$-direction and 8 sectors in $\phi$. The outer multiwire proportional chamber (COP) lies between COZ and CJC2. It is composed of 18 sectors in the $z$-direction and 16 sectors in $\phi$. The CIP and COP both consist of double cell layer, with wires parallel to the $z$-axis. The fast timing signals, with a time resolution better than the separation between two successive HERA bunch

crossings (75 ns for CIP and 60 ns for COP), are used to define vertex-pointing tracks for the purposes of triggering.

### The Forward Tracker

The Forward Tracking Detector (FTD) consists of three identical modules, known as supermodules, which contain planar drift chambers, MWPCs and a layer of transition radiator material and radial drift chambers.

Each planar module contains three planar wire drift chambers, rotated by 60° to each other in azimuth. These chambers consist of four wire planes in the $z$ direction with 32 wires per plane each. This design enables to provide a space point reconstruction in the $x-y$ plane with a spatial resolution of $\sigma_{xy} \simeq 160\,\mu$m.

The radial drift chambers consist of planes of sense wires strung out from the beam pipe, such that the maximum drift length for each wire increases with distance from the beam-axis. The radial chambers thus provides an accurate measurement of the azimuthal angle, together with a moderate measurement of the radial coordinate using charge division. The radial chambers are also used to detect the X-rays from the transition radiators. Each radial chamber has 48 cells in $\phi$ with 12 sense wires in $z$-direction.

The forward MWPCs are located between the radial and transition chambers in each supermodule, and consist of a double layer of wires strung along the vertical axis (i.e. the $y$-axis). The MWPCs in the first submodule are used in conjunction with the CIP and COP to provide a trigger on vertex position tracks. All three submodules are used to produce a trigger on tracks in the forward region.

### The Backward Drift Chamber

The Backward Drift Chamber (BDC) is mounted on the front surface of the Spacal calorimeter. It is designed to provide track segments for final state electrons entering the backward region and provide a better measurement of the electron angle than the Spacal calorimeter.

The BDC consists of four double layers of drift chambers in eight octants with sense wires strung in the radial direction. Each double layer is staggered in order to resolve the ambiguity of the track position in the drift coordinate. The layers are rotated by 11.5° with respect to one another in $\phi$ to enable construction of track segments from the intersection of hits in the layers. The BDC is designed to provide a space point resolution in the radial coordinate of $\sigma(r) = 0.4\,$mm and in the $\phi$ coordinate of $\sigma(r\phi) = 0.8\,$mm.

## 2.2.2 The H1 Calorimeters

The H1 tracking system is complemented by the H1 calorimeter system in order to measure the total energy of both charged and neutral particles produced in

the interaction. There are four detectors which provide energy measurement: the Liquid Argon, Spacal, tail catcher and plug calorimeters. The Spacal calorimeter is described in more detail in Chapter 3 and will not be mentioned here.

### The Liquid Argon Calorimeter

The Liquid Argon (LAr) Calorimeter provides the primary measurement of hadronic energy at H1. Above $Q^2 \simeq 100\text{GeV}^2$ the scattered electron in DIS is also detected in this calorimeter.

The LAr calorimeter covers the angular range of $4° < \theta < 154°$ and is mounted in a large argon cryostat. The calorimeter consists of an electromagnetic section with lead absorbers, corresponding to the depth of between 20 and 30 radiation lengths, and a hadronic section with steel absorbers. The total length of the LAr calorimeter is between 4.5 and 8 hadronic interaction lengths. The calorimeter is highly segmented in both sections, with a total of around 45000 cells. The orientation of the absorber plates is such that the angle of incidence of particles is always greater than 45°.

Test beam studies of LAr calorimeter modules have demonstrated energy resolutions of $\sigma(E)/E \simeq 0.12/\sqrt{E} \oplus 0.01$ with $E$ in GeV for electrons and $\sigma(E)/E \simeq 0.5/\sqrt{E} \oplus 0.02$ for charged particles. The very fine granularity of the LAr allows the longitudinal shower development to be used for efficient $e/\pi$ separation, with an observed contamination of less than $10^{-3}$. The overall electromagnetic energy scale is presently known to 3%, and the absolute scale of the hadronic energy measurement is known to 4%.

### The Tail Catcher

The tail catcher (TC) provides a coarse measurement of the energy of hadronic showers leaking out of the LAr detector. The TC is divided into central barrel and the forward and backward end-caps.

The energy resolution of the TC detector has been measured to be $\sigma(E)/E \simeq 100\%/\sqrt{E}$. The overall energy scale is known to 35%.

### The Plug Calorimeter

The plug calorimeter (PLUG) covers the extreme forward direction $0.6° < \theta < 3°$. Its primary task is to minimise the loss of transverse momentum due to hadrons emitted close to the beam pipe.

The design value of the energy resolution of PLUG is $150\%/\sqrt{E}$.

## 2.2.3 Muon Detection

Detection of muons is provided at H1 by two systems. The Central Muon System (CMD) consists of streamer tube chambers inside the instrumented iron return

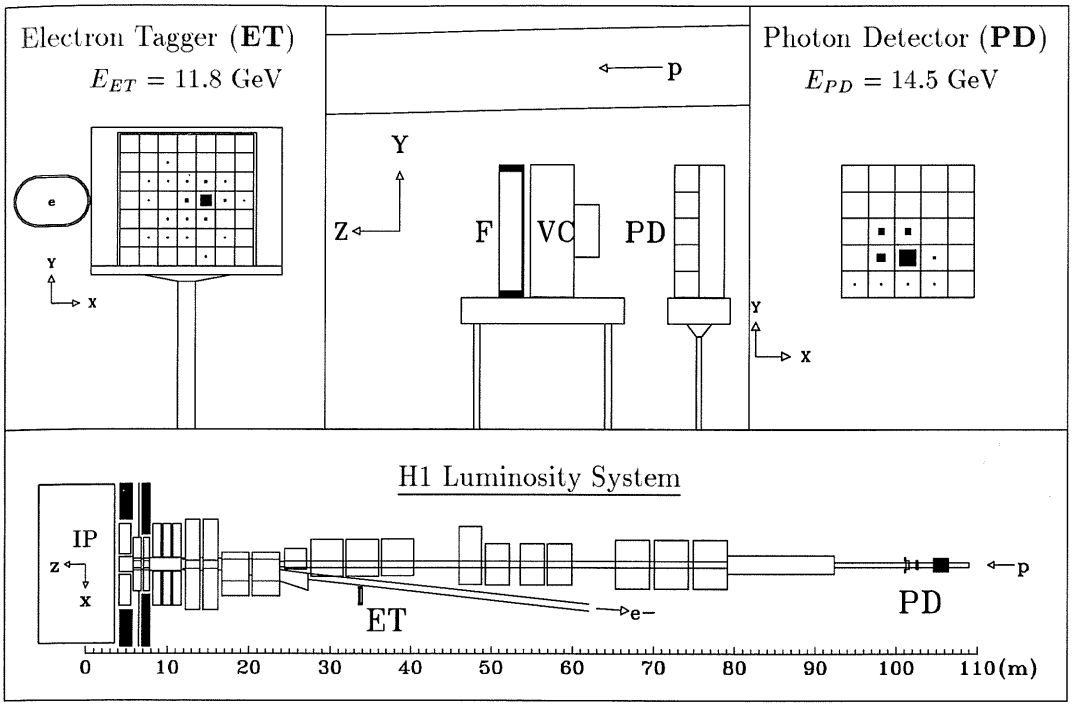


Figure 2.4: The H1 Luminosity System

yoke. The Forward Muon System (FMD) consists of four sets of drift chambers designed to measure the polar angle $\theta$, and two sets of drift chambers designed to measure the azimuthal angle $\phi$.

### 2.2.4 Luminosity Monitoring

A fast luminosity measurement is provided at the H1 detector by small angle electron and photon detectors in the electron direction, which are installed in the accelerator tunnel (see Figure 2.4). Furthermore this system detects and triggers on scattered electrons at very low $Q^2 (< 10^{-2}\,\mathrm{GeV}^2)$.

The luminosity measurement is enabled by the Bethe-Heitler radiative process $ep \to e\gamma p$. This process has a large, well known and exactly calculable cross-section, which allows to use this reaction to measure the luminosity. The sum of outgoing $e$ and $\gamma$ energies is constrained, in the limit $Q^2 of \to 0$, to the electron beam energy, i.e. $E_e = E_{e'} + E_\gamma$. The thresholds are applied at 5 GeV to both energies to remove noise and trigger threshold effects.

The electron and photon detectors are TIC1/TIBr crystal calorimeters, with a resolution of $\sigma(E)/E \simeq 10\%/\sqrt{E}$. The electron tagger (ET) is located at position $z = -33\,\mathrm{m}$ and the photon detector (PD) at $z = -102.9\,\mathrm{m}$. The electron detector detects electrons with an energy fraction between 0.2 and 0.8 with respect to the

beam energy and angles $(180° - \theta) \leq 5$mrad and is also used as a trigger for photoproduction interactions, in which case it is combined with a veto against there being a photon in the small angle photon detector. The ET consists of 49 crystal calorimeters read out by photomultipliers. The PD consists of 25 crystals of the same design as the ET. A lead filter (F), which protects the photon detector proper from the high synchrotron radiation flux, is mounted before the ET together with Cerenkov Veto Counter (VC) which rejects events with photons originating from interactions in the filter.

### 2.2.5 The Time-of-Flight Detectors

Fast scintillation detectors at H1 are needed in order to distinguish real *ep* interactions from proton induced background appearing upstream the detector. The particle produced from *ep* interaction will arrive at different time than particle produced from the background interactions relative to the nominal time of the bunch crossing. This is caused by different path lengths and different times of interactions. Background events produced near the nominal vertex cannot be distinguished from genuine *ep* interaction in this way, the scintillation counters, however, give a significant reduction of the background.

The Time-of-Flight (ToF) system consists of a number of components. Scintillators are mounted between the backward end-cap of the return yoke and the beam pipe (BToF), within the unused gaps of the PLUG absorber (PToF) and around the beam pipe in the region of the FMD (FToF). In addition, the inner and outer veto walls are situated backward of the return yoke at $z = -6.5$ m and $z = -8.1$ m respectively. These are known as the Veto Wall and detect particles (mostly muons) from the proton beam halo.

The Spacal calorimeter, which is close to the beampipe in the direction of the incoming protons, is also used for ToF purposes.

## 2.3 The Trigger System

Interactions at the H1 detector are dominated by background events rather than the physics events. In order to select interesting physics processes, the H1 detector is equipped with a trigger system. The philosophy of the trigger is to minimize the dead-time of experiment, which is the time following a trigger in which the signals from subsystems are being read and therefore the subsystems are insensitive to new events. For the background rate of 10 kHz, the H1 trigger is able to reduce the event rate to $\approx 50$ Hz with a dead time of about 10%. For detailed information of events rates see Table 2.1.

Background events that have to be considered include

- interactions between beam electrons or protons with the residual gas in the beampipe;

| | |
|---|---|
| beam gas interactions | 50 kHz |
| cosmic $\mu$ in barrel | 700 Hz |
| tagged $\gamma p$ | 25 Hz |
| $e\bar{e}$ total | 15 Hz |
| DIS low $Q^2$ | 2.2 Hz |
| DIS high $Q^2$ ($e$ in LAr) | 1.4 $\text{min}^{-1}$ |
| Charged current DIS $p_T > 25$ GeV | 30 $\text{h}^{-1}$ |
| W production | 0.5 $\text{d}^{-1}$ |

Table 2.1: The event rates at design luminosity $\mathcal{L} = 1.5 \times 10^{31} cm^2 s^{-1}$ [9].

| | |
|---|---|
| width of proton bunch | 1.4 ns |
| distance to next satellite bunch | 5 ns |
| flight time to backward ToF | 6 ns |
| flight time to barrel muon system | 20 ns |
| **bunch crossing interval** | **96 ns** |
| longest drift time in CJC | 1 $\mu$s |
| integration time of LAr preamplifier | 1.5 $\mu$s |
| delay of first level trigger | 2.5 $\mu$s |
| front end readout time | $\sim 1$ $\mu$s |

Table 2.2: Time scales at HERA and H1 [9].

- interactions between off momentum beam particles and the wall of the vacuum chamber;
- synchrotron radiation;
- cosmic rays.

The HERA bunch crossing interval of 96ns is short when compared with the response times of many subdetectors. For example in the drift chambers the maximum drift time is of the order of 1 $\mu$s (for detailed information see Table 2.2). Consequently the readout is *pipelined* in synchronisation with the HERA clock (HCKL). For at least 24 bunch crossings the information is being stored whilst an initial trigger decision (L1) is determined. The L1 trigger thus turns out to be deadtime free.

The H1 trigger is of a multilevel design. Each successive level processes more precise data and takes longer time to make a better trigger decision of keeping events. The trigger information is centrally controlled by the Central Trigger Logic (CTL) which makes a global decision based on combination of all subsystem trigger information.

**Level 1** The trigger level 1 consists of nine different trigger systems, each based on the information given by a subdetector. The outputs of these systems

are called *trigger elements*, i.e. {yes/no} decision encoded in bits. The types of information from which trigger elements are created include:

- **Calorimeter energy:** signals in LAr and Spacal are summed in *towers* and compared to thresholds in order to find jet and electron candidates.
- **Z-vertex:** information from central tracker MWPCs is used to determine the position of interaction vertex.
- **Time-of-flight:** the ToF systems described in Section 2.2.5 are used to generate triggers for in-time events or veto for background events.
- **Muon tracks:** the central muons system generates triggers for muons in iron return yoke. The forward muon system information is processed by a sophisticated trigger system which extracts a $t_0$ and pointing track candidates from the drift chamber signals.

Trigger elements are then used in CTL and combined to so called *subtriggers*. Up to 128 subtriggers can be defined in order to select interesting physics events (physics triggers), to monitor detector efficiency (monitor triggers) or to select cosmic ray events for calibration purposes (cosmic triggers). The rate of each subtrigger is computed separately and can be prescaled if needed. The final level decision of L1 is given by the logical OR of all subtriggers and is distributed to the front end electronics of all subsystems to stop the pipeline.

**Level 2** The L2 trigger provides a complex decision based on more detailed informations. The systems are based on topological array [10] and more sophisticated neural technology [11], both of which are suited to make decisions based on correlations in multi-dimensional space.

Decision of the trigger level 2, which is ready after a period of typically 20 $\mu$s, defines whether a fast rejection will be applied or whether the event is to be treated further.

**Level 3** This level was proposed as further intermediate trigger step to suppress event rate but has not yet been put into operation.

**Level 4** The level 4, which is integrated in the central data acquisition system, is based on a farm of approximately 30 fast RISC processor boards. Each processor reconstructs a complete event to which it applies a series of selection criteria depending on subtriggers that passed the event. For example one of the most important rejection algorithms relies on the event $(x, y, z)$ vertex constraint. Events which pass the L4 are written to a tape at a typical rate of 10 Hz. The average size of one event is 130 kB. L4 also creates separate streams of events for the purposes of monitoring and calibration of some

subdetectors. A small fraction of events rejected by L4 are brought off and written to tape to enable monitoring of the effects of the L4 decisions.

The full event reconstruction is processed by dedicated workstations within typically a day of data taking. The events are also classified into different physics classes dependent on physics area of interest. This can be considered as the fifth level (L5) of the H1 trigger system. The full events are written to Production Output Tapes (POT) and stored.

# Chapter 3

# The Spacal Calorimeter

Since 1994/95 winter shutdown the Spacal[1] Calorimeter replaces the Backward Electro-Magnetic Calorimeter (BEMC) in the backward region of the H1 detector. This section describes the Spacal calorimeter design and gives a brief description of the Spacal calibration methods and Spacal IET trigger. For the detailed description of Spacal see [12, 13].

Figure 3.1 shows the position of the Spacal in the backward region of the H1 detector. The front face $z$-position is -150 cm. The Spacal has a diameter of 160 cm (see Figure 3.2) and consists of an electromagnetic (EM) and hadronic (HAD) section with an active depth of 25 cm each.

The required features of the new calorimeter are as follows:

- **Extension of kinematic range at low $x$ and $Q^2$:** this is enabled by the extension of the angular range for the electron detection up to $\theta \leq 177.8°$ with respect to the nominal interaction point, which corresponds to the range of $Q^2 \geq 0.85\,\mathrm{GeV}^2$.

- **High resolution in $\theta_e$ and $E_e$:** this allows to resolve exclusive processes (e.g. the measurement of decay products of light mesons such as $\pi^0 \to \gamma\gamma$ as well as the measurement of QED final state radiation.

- **Reliable electron identification:** the probability of misidentification of a pion as an electron is less than $10^{-2}$. This is useful to reduce photoproduction background which is several orders of magnitude larger than DIS.

- **Good coverage and containment for hadronic energy flow:** the measurement of hadronic energies in the backward region of the H1 detector is improved with respect to the previous one.

[1] 'Spacal' comes from Spaghetti Calorimeter

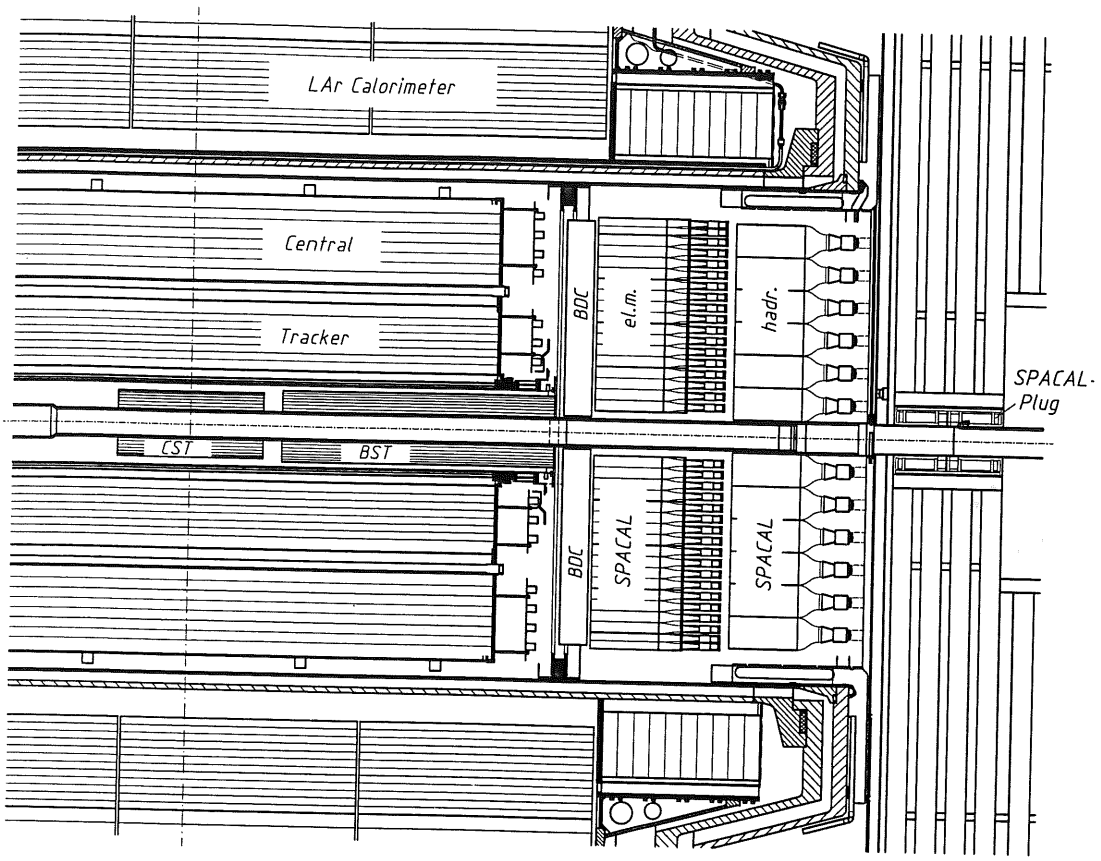


Figure 3.1: The position of Spacal calorimeter in H1 detector.

- **Good time resolution and fast signal response:** a resolution better than 1 ns allows the construction of Time-of-Flight based inclusive electron trigger (IET) which provides the means to efficiently reduce the proton beam related background. This capability is needed at the first trigger level.

- **Low trigger thresholds:** the use of photomultiplier tubes (PMT) and an electronic chain with an extremely low noise at a level of 3 MeV allows very low trigger thresholds and a reliable reconstruction of very small energy deposits. The Spacal is therefore sensitive to minimally ionisating particles.

- **The Spacal has a very good homogeneity:** the special lead-fiber detector design provides a compact active volume of this calorimeter.

## 3.1 Spacal Design

The arrangement of H1 subdetectors determined the technical parameters of the Spacal Calorimeter. The depth is limited by the distance between the end of the

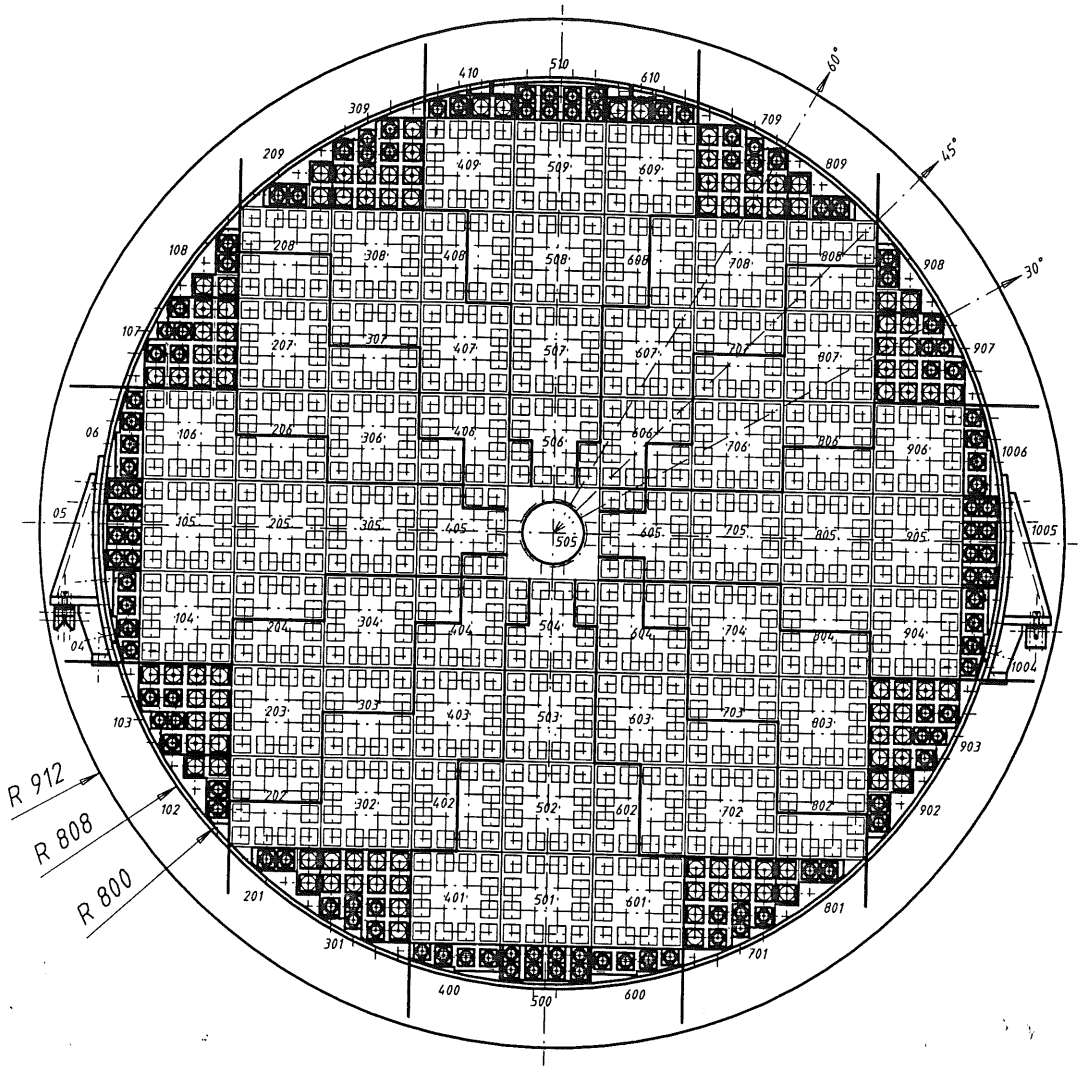


Figure 3.2: The XY view of Electromagnetic Spacal Calorimeter.

central tracker and the return yoke and the maximum weight of Spacal depends on the inner rails of the cryostat which can support 8 tones of mass in the backward region [13]. Technical parameters of EM and HAD sections are summarized in Table 3.1. The acceptance of the HAD section is increased to 178.7° by a backward plug section (BPLUG)[2] which is mounted on the return yoke.

The electromagnetic section of Spacal consists of 1192 cells with an active volume $40.5 \times 40.5 \times 250\,\mathrm{mm}^3$ each. A front view of Spacal electromagnetic section is shown in Figure 3.2. The cells consist of lead sheets with grooves into which scintillating fibers are laid. Incident particles shower in the lead and the products of the shower cause the fiber to scintillate. The light is then collected at

[2]The BPLUG was installed during the 1995/96 winter shutdown.

| | Electromagnetic | Hadronic |
|---|---|---|
| Fiber Diameter | 0.5 mm | 1.0 mm |
| Fiber Type | Bicron BCF-12 | Bicron BCF-12 |
| Pb/Fiber Ratio | 2.3:1 | 3.4:1 |
| Pb-Fiber Density | 7.3 g/cm$^3$ | 7.7 g/cm$^3$ |
| PMT Type | Hamamatsu R5505 | R2490-06 |
| Cell Size | 40.5 × 40.5 mm$^2$ | 120 × 120 mm$^2$ |
| Number of Cells | 1192 | 136 |
| Angular Coverage | $\leq 177.5°$ | $\leq 178°$ |
| Active Length | 25 cm | 20 cm |
| Radiation Length | 0.91 cm | 0.85 cm |
| Interaction Length | 25 cm | 20 cm |
| Molière Radius | 2.55 cm | 2.45 cm |

Table 3.1: Technical parameters of the Spacal Calorimeter.

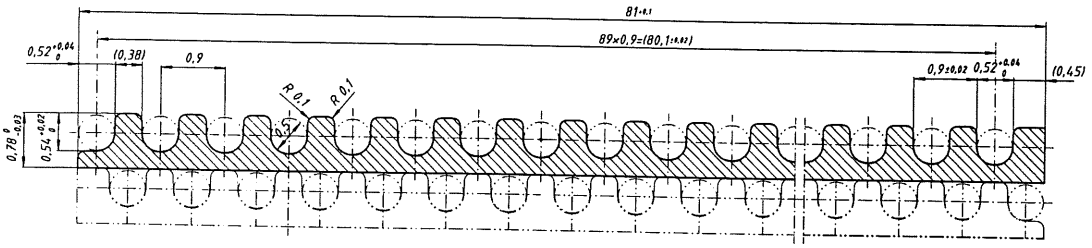


Figure 3.3: The profile of lead sheets (Electromagnetic Spacal).

the one end of the fibers and measured by a photomultiplier (PMT). The profile of lead sheet is shown in Figure 3.3. The lead/fiber ratio is 2.27:1. 2-cell-unit (see Figure 3.4) consists of 52 stacked lead plates with 4680 fibers each. Eight of these pairs are held together to form a supermodule.

The HAD section consists of 136 cells of 120 × 120 × 250 mm$^3$ providing an equivalent of one nuclear interaction length. The fibers are of the same type as in the EM section but have a larger diameter of 1.0 mm. The construction of HAD section is similar but the cells are assembled individually.

The BPLUG consists of 12 cells of trapezoidal cross-section which are arranged in a ring surrounding the beam pipe and four veto layers of 8 mm width. At the inner radius of 5.7 cm a tantalum frame shields against synchrotron radiation from the beam. The veto layers are used to measure potential energy leakage into the beam pipe.

The PMTs have to operate in the 1.2 T magnetic fields. Chosen PMTs (Hamamatsu meshdynode type) provides a typical gain of $10^4$, a factor of 100 smaller than in case of no field [14]. Each supermodule is furnished with a high-voltage (HV) distribution module which provides a high-voltage for PMTs. A calibra-

tion module (CAM) is attached to the rear of each supermodule. CAM contains control electronics and two pulses LEDs which feed light through fibers into light mixers and PMTs. Potential instabilities of light output of each LED are monitored by photodiodes. The LEDs are typically pulsed at a rate of 1 Hz, synchronised to empty HERA bunches. LED pulses are used to monitor the stability of the photomultiplier gains and therefore for the calibration of the calorimeter [15].

## 3.2 The Inclusive Electron Trigger

The Spacal trigger has to provide two functions; a trigger for events containing electron candidates and a veto of events originating from beam-induced background. The system consists of the Inclusive Electron Trigger (IET) for the EM section, plus AToF veto and ToF/AToF total energies ($E_{tot}$) for both EM and HAD. In this subsection the description of the IET will be presented.

The IET trigger [16] of the Electromagnetic Spacal is segmented in 320 arrays of $4 \times 4$ neighbouring cells (IET-windows). The input to these arrays are the $2 \times 2$ ToF-gated (in-time) analog sums which are combined again to give a summation of energy deposited in the IET-window. The IET-windows are overlapping in both directions (they are 'sliding'). This technique guarantees that there is no loss of events arising from electrons with an impact point close to the edge of the IET-window. Three different discrimination thresholds, IET$>0$, IET$>1$ and IET$>2$ are used for triggering purposes. These thresholds are adjustable in the range between $\sim 100$ MeV and $\sim 20$ GeV. If, inside an IET-window, a signal exceeds any discriminator threshold a logical bit (cluster bit) is set. The Spacal trigger logic combines the logical 'or' of all cluster bits, except the central region which is processed separately, for each of the three thresholds and the result is encoded in a 2 bit trigger element which is sent to the central H1 trigger controller. These trigger elements are then combined with those from other subdetectors into

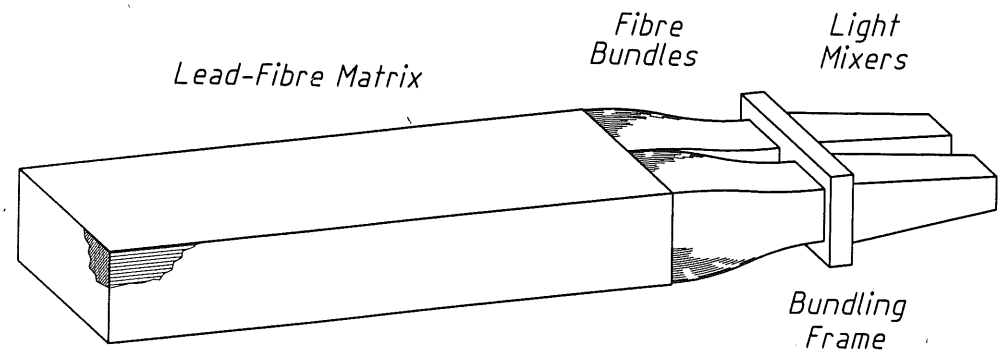


Figure 3.4: The module of Electromagnetic Spacal calorimeter.

the subtriggers at the L1 trigger level. The cluster bits are also available at the L2 trigger level.

## 3.3 Calibration of Spacal

The precise knowledge of the energy scale is required for the measurement of the scattered electron, which is, for low $Q^2$, detected in the Spacal calorimeter. The energy calibration of the Spacal consists of two groups of methods. Namely the relative comparison of the response of the calorimeter cells and an estimation of the absolute energy scale. The relative calibration is needed in order to obtain homogeneous response of the calorimeter and an optimum energy resolution. An example of relative calibration method is the *cosmic muons method* [17]. The absolute calibration is essential for the correct reconstruction of the event kinematics. The established methods are as follows: *kinematic peak method, double angle method* and *monochromatic peak method* [18]. In this section the kinematic peak absolute calibration method [18, 19] is introduced.

### 3.3.1 The Kinematic Peak

At low and moderate $Q^2(\leq 100\,\mathrm{GeV}^2)$ at HERA the energy distribution of scattered electrons has a characteristic shape with a prominent peak which is commonly called *kinematic peak*. In Figure 3.5 a typical energy distribution generated by a Monte Carlo simulation of $ep$ DIS is shown. The mean energy for events with energy between 23 - 30 GeV is 26.48 GeV for the generator level and 26.26 GeV for the reconstruction level. The difference between the histogram shapes and between the mean energies is due to the detector acceptance, i.e. energy loss in dead material.

The shape of the kinematic peak originates mainly from kinematic effects. The minor component comes from calorimeter properties and from distribution of partons in the proton. The kinematic peak is caused by (quasi-) elastic electron-quark scattering. The latter process delivers electrons with beam momentum for small (in laboratory frame) scattering angles, but its cross section is strongly damped by the elastic formfactor for increasing scattering angles, equivalent to increasing $Q^2$. The sub - process of electron - quark scattering, however, leads to scattered electrons carrying the beam momentum even for large $Q^2$.

The shape of the energy spectrum can be understood by investigation of the cross section dependence on inelasticity $y$:

$$\frac{\mathrm{d}^2\sigma}{\mathrm{d}Q^2\mathrm{d}y} = \frac{2\pi\alpha^2}{Q^4 y}\left(2(1-y)+\frac{y^2}{1+R}\right)F_2(x,Q^2). \qquad (3.1)$$

The structure function $F_2(x,Q^2)$ is relatively flat in the whole accessible region. Therefore at sufficiently small values of $y$ the cross section rises propor-

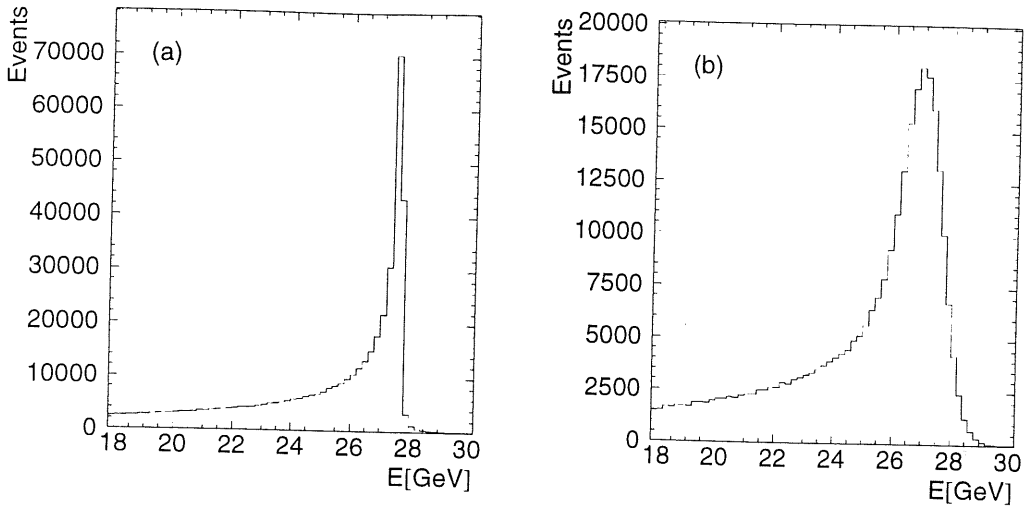


Figure 3.5: The kinematic peak in the distribution of energy of the scattered $e$ in Monte Carlo simulation on generator level (a) and on reconstruction level (b).

tionally to $1/y$. This dependence translates into the energy behaviour via the relation

$$\frac{1}{y} = \frac{E_e}{E_e - E'_e \sin^2(\frac{\theta}{2})}. \tag{3.2}$$

The above equations show that the cross section becomes large in the region of $E_e \approx E'_e \sin^2(\frac{\theta}{2})$. Taking into account the transformation $(y, Q^2) \rightarrow (E, \theta)$ the kinematic peak appears more pronounced towards smaller $Q^2$.

### 3.3.2 The Calibration Algorithm

The energy calibration using the kinematic peak is based on comparisons between Monte Carlo simulations and data. Monte Carlo simulations are used to calculate the exact position and shape of the peak. In the next step correction factors are applied to the data such that the measured position of the kinematic peak matches with the simulated position. Several iterations are needed in order to obtain good agreement. Procedure described below is established for the routine calibration of Spacal data during the data taking where L4 tapes for calibration purposes are used [20].

The basic steps of the calibration are as follows:

1. Events are selected by using basic spatial and energy cuts. A cluster with the highest energy is taken to be electron cluster. More precise cuts are impossible because the L4 tapes contain informations from Spacal only. In addition, cuts on the electron candidate energy ($23 < E_{cl} < 30\,\mathrm{GeV}$) and on the cluster radius ($R_{cl} < 3.2\,\mathrm{cm}$) are applied.

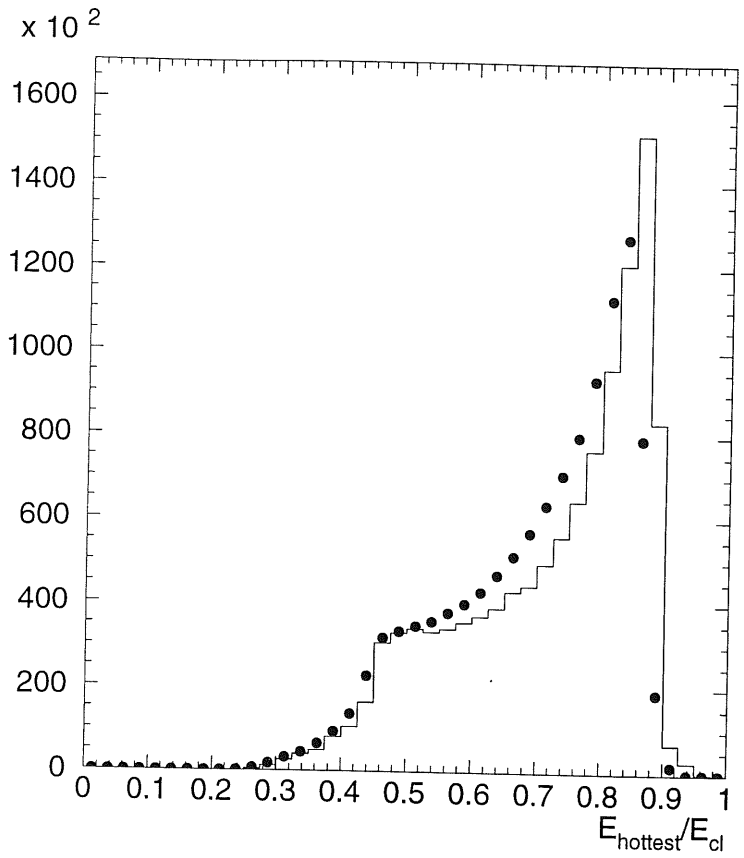


Figure 3.6: The ratio of the energy of the hottest cell in the cluster over the cluster energy for data (dots) and Monte Carlo (solid line).

2. Energy of cluster $E_{cl}$ is assigned to the hottest cell of this cluster when condition $E_{\text{hottest}} > 0.6 \times E_{cl}$ is satisfied (see Figure 3.6 for distribution of ratio $E_{\text{hottest}}/E_{cl}$), otherwise the event is rejected.

3. The distribution of energy of accepted electron clusters in each cell (corresponding to the hottest cell in a given cluster) separately is built.

4. The correction factor for a given cell $i$ is defined as

$$c_i = \frac{\langle E_{cl,i}^{MC} \rangle}{\langle E_{cl,i}^{data} \rangle} \tag{3.3}$$

where $\langle E_{cl,i}^{data} \rangle$ and $\langle E_{cl,i}^{MC} \rangle$, are the mean values of energy in energy distributions for cell $i$ for measured events and Monte Carlo events respectively. In good approximation one mean value of energy $\langle E_{cl}^{MC} \rangle$ can be used for all Spacal cells instead for each cell separately (see Figure 3.11 and the text below).

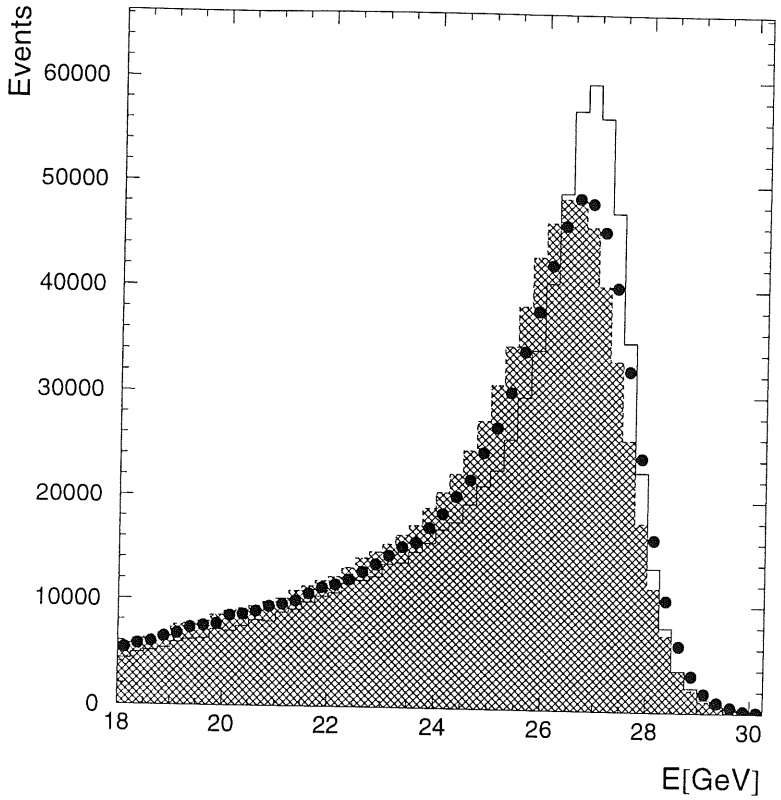


Figure 3.7: Energy distributions for Monte Carlo (solid line), data without the recalibration (hatched) and data recalibrated with the *'kinematic peak'* calibration method (dots). Histograms are normalized to the number of events with energy between 23 - 30 GeV. L4 tapes for the calibration purposes were used.

There are two basic ideas for this algorithm:

- An electromagnetic shower is completely contained in a region of calorimeter covered by only few cells.
- The shape and position of the kinematic peak are well known by simulation and they are in good approximation independent of the structure function.

### 3.3.3 Calibration Results

The following results were obtained by using software prepared by the Spacal group [21].

Background in the selected interval around the beam energy (i.e. 23 - 30 GeV) originates mainly from proton-gas and proton-pipe wall interactions. It is suppressed by the demand that the cluster radius must be less than 3.2 cm and the

time of flight measured by the Spacal TDC system with respect to the bunch crossing time has to be between 10 ns and 20 ns. Figure 3.7 shows the energy distributions for data before and after the recalibration and for to the Monte Carlo simulation. The mean energy for events with the energy between 23 - 30 GeV is 25.9 GeV before the recalibration and 26.1 GeV after the recalibration, which corresponds well to the Monte Carlo events which yield 26.17 GeV. Data presented in this section were taken from the run interval 197600-199049 from special L4 tapes.[3]

The event rates in each cell separately are plotted in Figure 3.8. The asymmetry around the center of the detector is caused by a Spacal special trigger reducing *hot spots* which seem to originate from the synchrotron radiation. Hot spots are not included in the Monte Carlo (see Figure 3.9).

In Figure 3.10 examples of behaviour of some selected cells are displayed. The cell No. 100 has a very abnormal energy distribution and *calibration stability*[4]. The cell No. 36 is the typical example of a cell with a good response but a bad stability. The instability of the response causes that the kinematic peak becomes wider. The cell No. 20 exhibits a typical behaviour of a good cell.

The stability of the Spacal calibration in different radii intervals is illustrated in Figure 3.11. The mean values of energy slightly fall towards large radii, but the decrease is less than 0.4 % and could be neglected.

Figure 3.12 shows behaviour of some cells in the central part of the Spacal. Cell 46 (ID 15046) shows an example of a time instability of high voltage on photomultiplier where the change of the high voltage causes a 'double peak' effect. Cells 13, 14, 15 (ID 15013, 15014, 15015) and some neighbouring cells are affected by the synchrotron radiation (hotspots). Cell 25 is an example of a good cell behaviour.

The kinematic peak method gives the uncertainties of the absolute energy scale about $1-2\,\%$. Better precision is achievable by using the fact that the event kinematic can be determined by the measurement of both the hadronic final state and the scattered electron. This fact can be exploited for independent calibration checks, e.g. double angle method, where the electron energy is calculated from electron and hadron final state angles.

[3] Selected runs were analyzed during my presence in DESY, Hamburg.

[4] Calibration stability denotes the mean value of energy $\langle E_{cl}^{data} \rangle$ for a given cell (set of cells) as a function of the consecutive event number (run-number, time, ...).

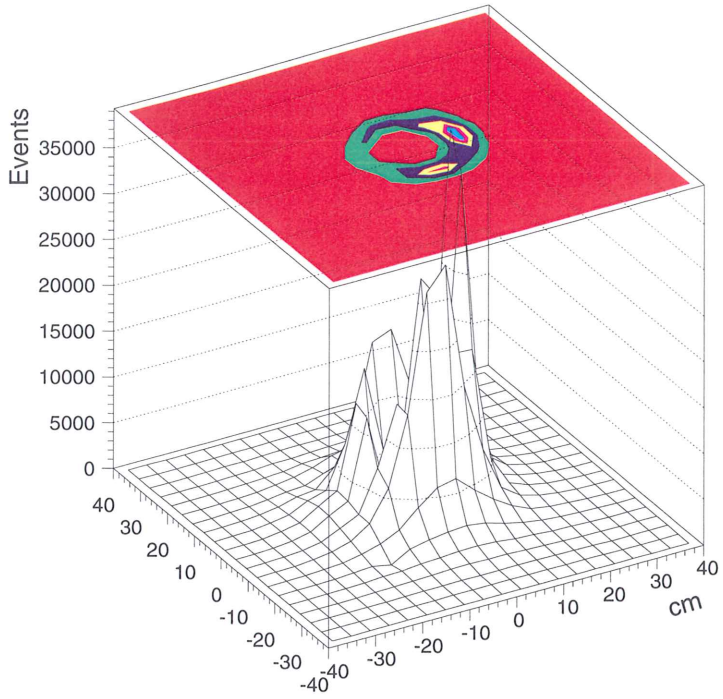


Figure 3.8: The XY-plane spatial distribution of scattered $e$ in the Spacal calorimeter from L4 data tapes.

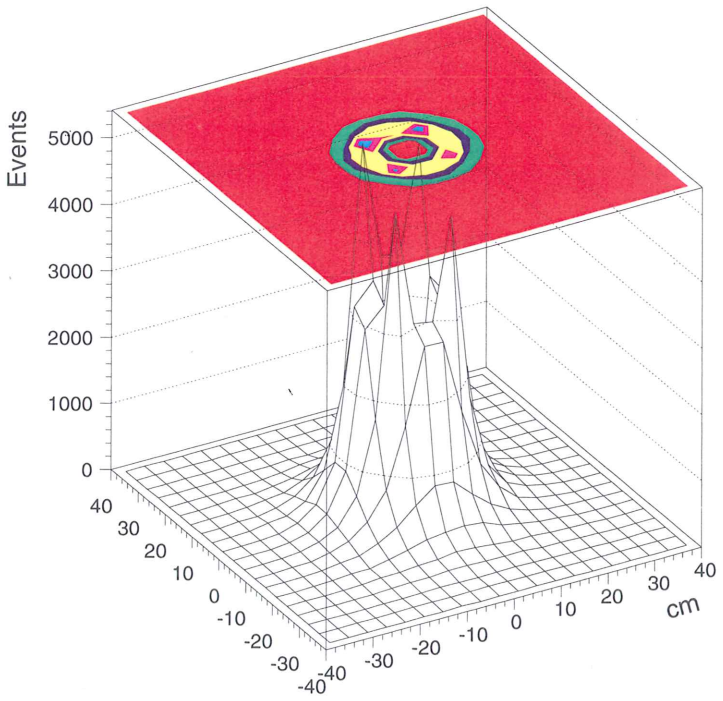


Figure 3.9: The XY-plane spatial distribution of the simulated scattered $e$ in the Spacal calorimeter.

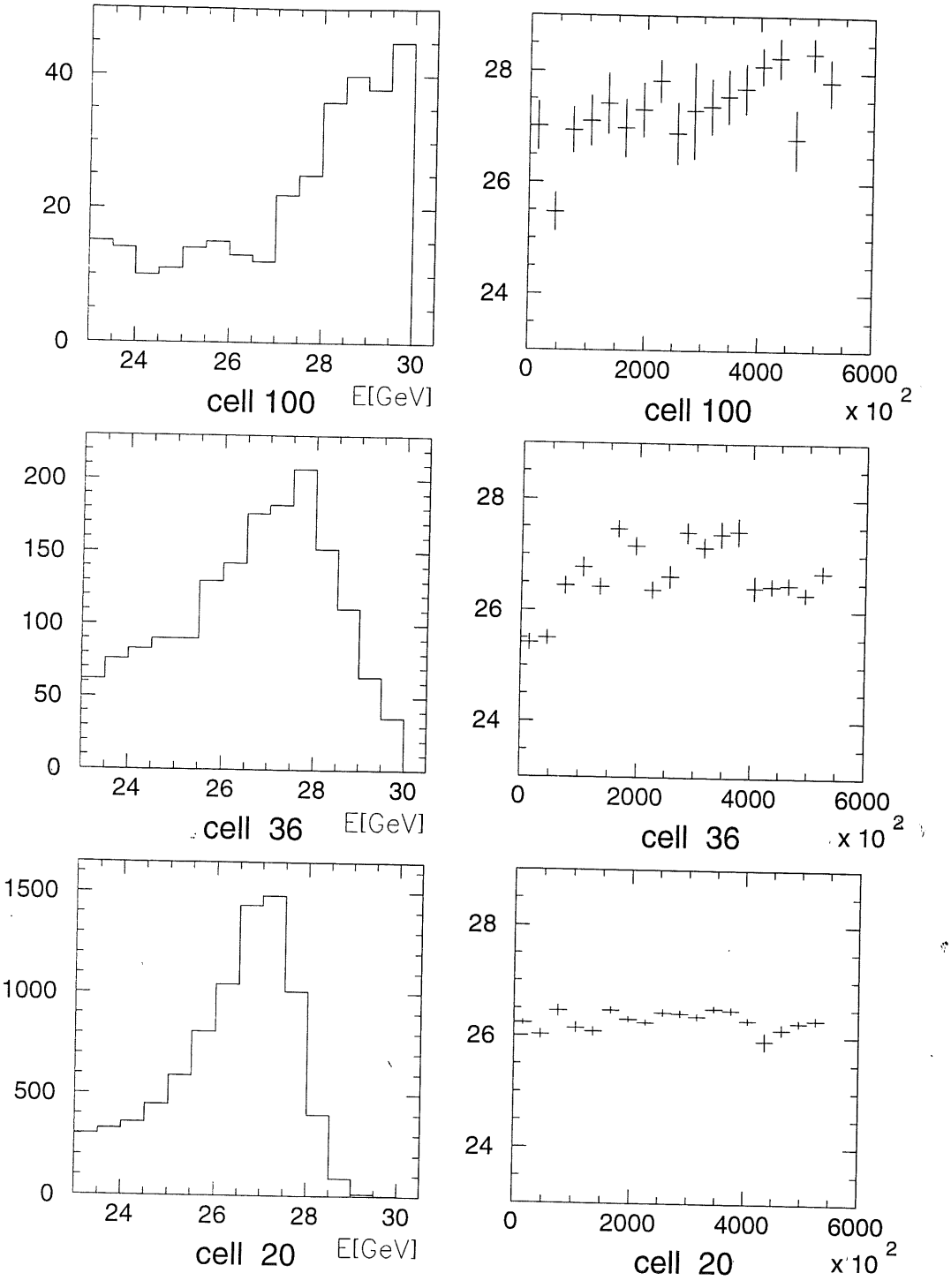


Figure 3.10: The energy distributions (left column) and the energy stability as a function of the consecutive event number (right column) for selected cells of Spacal. Each dot in stability graphs represents a mean energy of 3000 consecutive events selected with the requirement: $23 < E_{cl} < 30\,\mathrm{GeV}$. Cell 100 has a bad response and cell 36 a bad stability. Cell 20 is an example of a good cell. Data corresponds to the run-interval 197600-199049 and they are presented without recalibration.

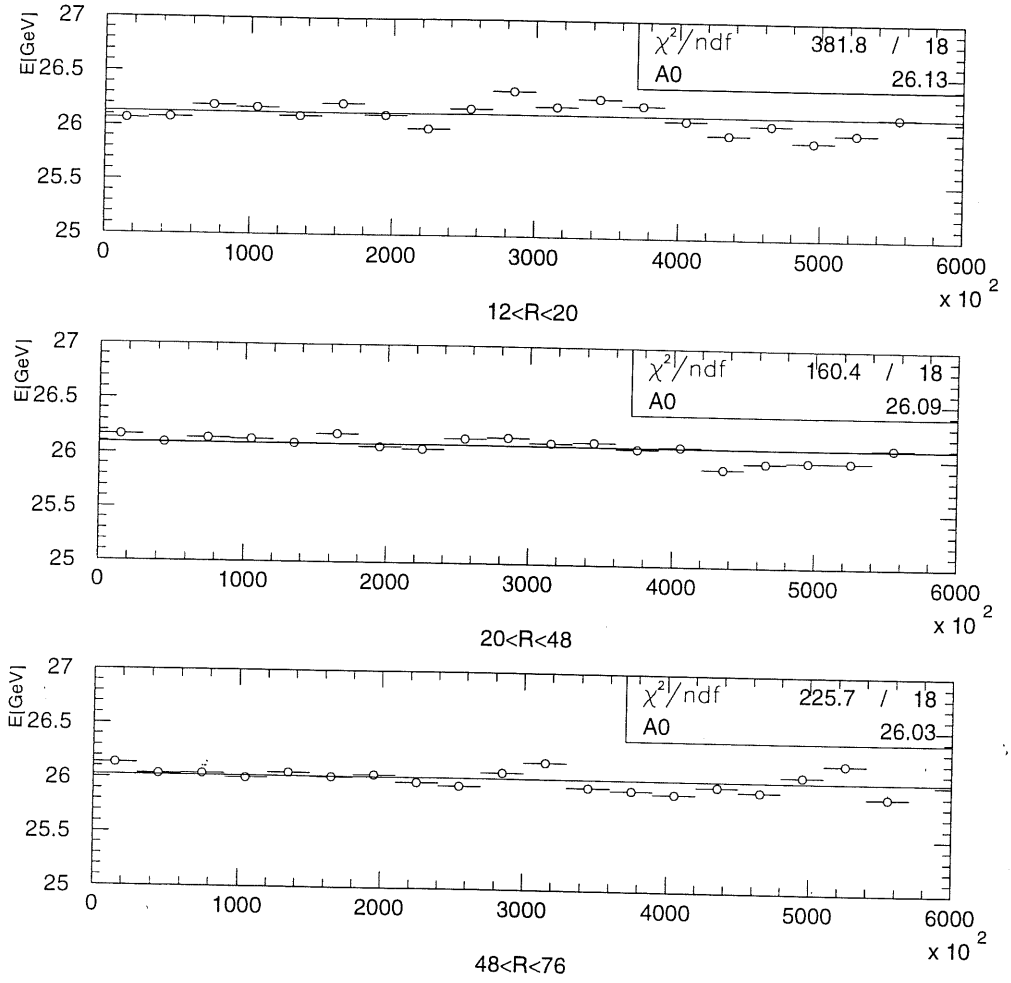


Figure 3.11: Spacal calibration stability for selected radii intervals (cm) in Spacal as a function of the consecutive event number. Each dot represents the mean energy of 30000 consecutive events. Horizontal line in each histogram represents the fit by a constant (its value is denoted A0).

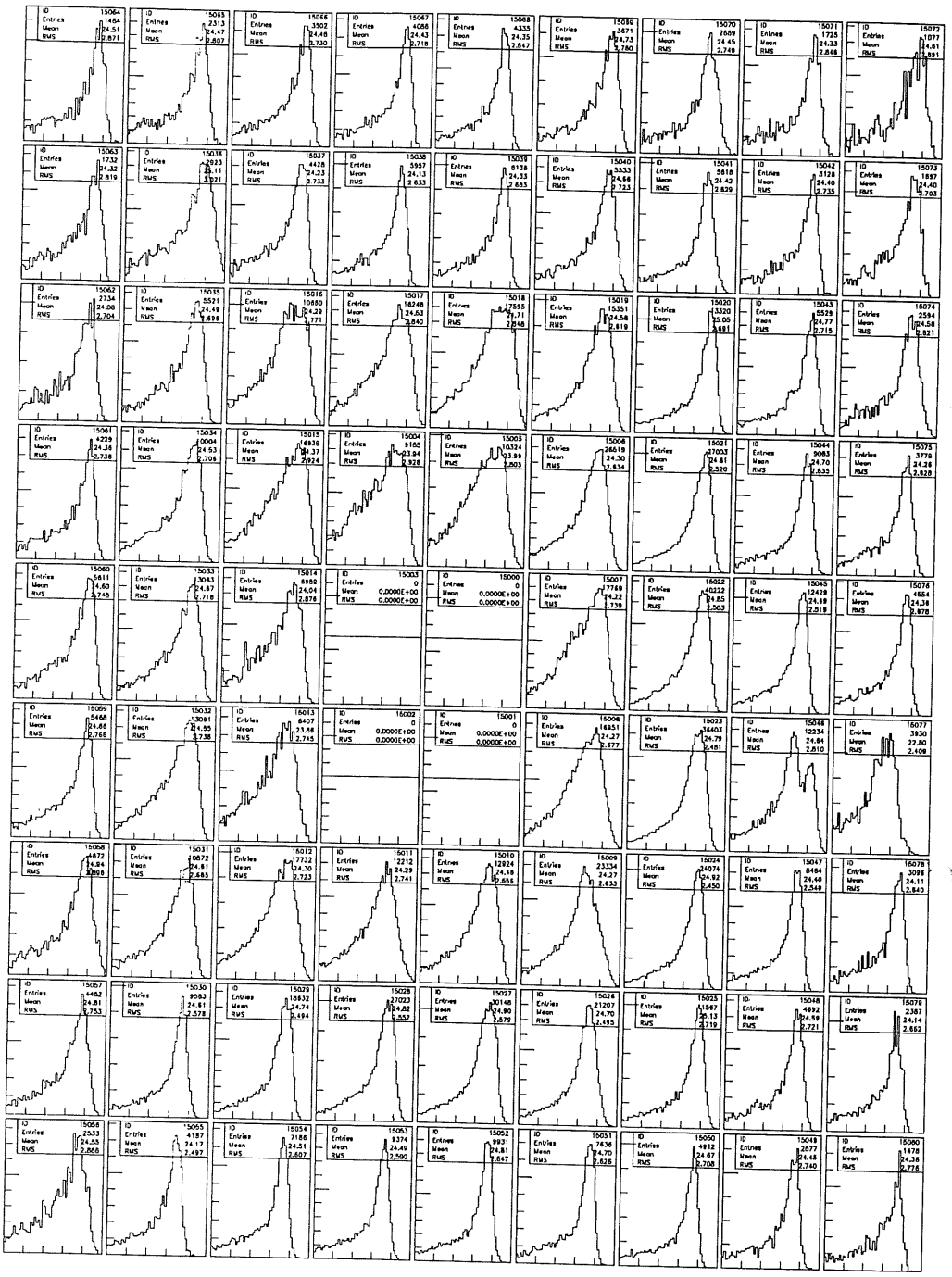

Figure 3.12: The cell energy distributions in the central part of Spacal. The scale on x-axis is 17 - 30 GeV. The cells are arranged in the same way as in the real detector.

# Chapter 4

# Data Treatment

In this chapter an analysis of DST1 data accumulated by H1 in 1997 is presented. We selected runs[1] taken in June and July with the run numbers between 190125 - 197000. Corresponding interval of luminosity fills is 1380 - 1550.

During the preparation of this thesis only the DST1 tapes which contain events reconstructed in parallel with the data taking were available. The data volume was reduced by creating n-tuples [21, 25] stored on the disks of the H1 Zeuthen group and which served as an input data for the analysis in the framework of the graphical package PAW. When the running period had finished in October 1997, the new set of parameters was introduced into the database and the reconstruction program was tuned for the 1997 data. The data reprocessing started in November and took several months. N-tuples from this more precise data have not yet been available.

In the following analysis the software package and share libraries developed by the Zeuthen group were used together with my own programs.

The chapter is organized as follows: In Section 4.1 a simple method to recalibrate Spacal is described and a more precise method is mentioned. The $\pi^0$ Spacal calibration cross check is presented in Section 4.2. In Section 4.3 an outline of deep inelastic event selection is given. The run selection criteria are listed in Section 4.4. Analysis of $z$-vertex[2] distributions of simulated events and data is described in Section 4.5. In Section 4.6 the logic of relevant subtriggers is explained along with the event-weight calculation. Finally, the efficiency of subtriggers is studied in Section 4.7.

## 4.1 Recalibration of Spacal

In order to make some preliminary analysis it is useful to improve Spacal calibration. It can be done in a simple way as a global recalibration of all Spacal cells by

[1] It does not correspond to data used in the previous chapter for Spacal calibration.
[2] The term $z$-vertex is further used for the $z$-coordinate of the interaction vertex.

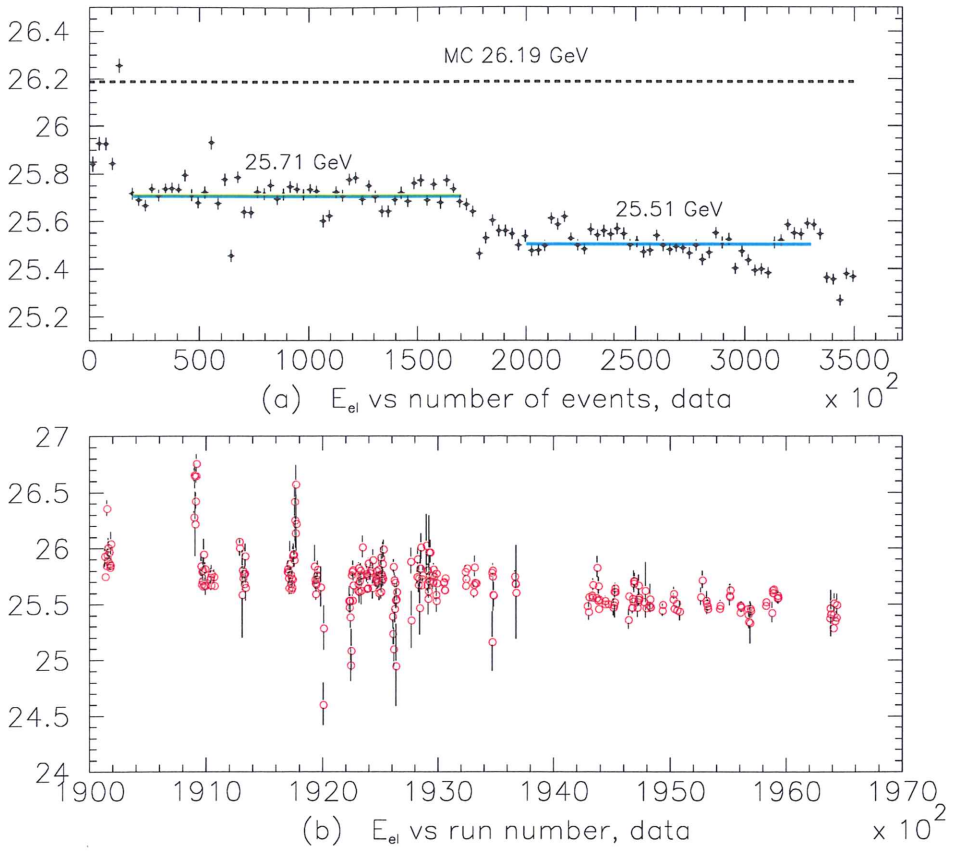


Figure 4.1: The calibration stability for DST data as a function of the consecutive event number (a) and run number (b). Dashed line in (a) represents the mean value of $E_{el}$ for Monte Carlo, other two lines correspond to fit to a constant for two data intervals. Numbers are the y-coordinates of horizontal lines.

one calibration constant obtained by comparison with Monte Carlo. It is based on the *kinematic peak* method mentioned in Section 3.3.2. The mean energy is calculated for each run or for a number of consecutive events and its dependence on the run number or the consecutive event number is plotted in Figure 4.1. A drop of the mean energy is seen around the run No. 194000. Therefore the total event sample was divided into two parts which were fitted to a constant. The results of these fits were compared with the mean energy of simulated events. The recalibration of measured energies in Spacal means the multiplication of an energy by the ratio of simulated and measured mean energies. The energy of events of the runs taken before the run 194000 should be recalibrated by a factor about 1.02. For runs after the run 194000 this factor is approximately 1.027.

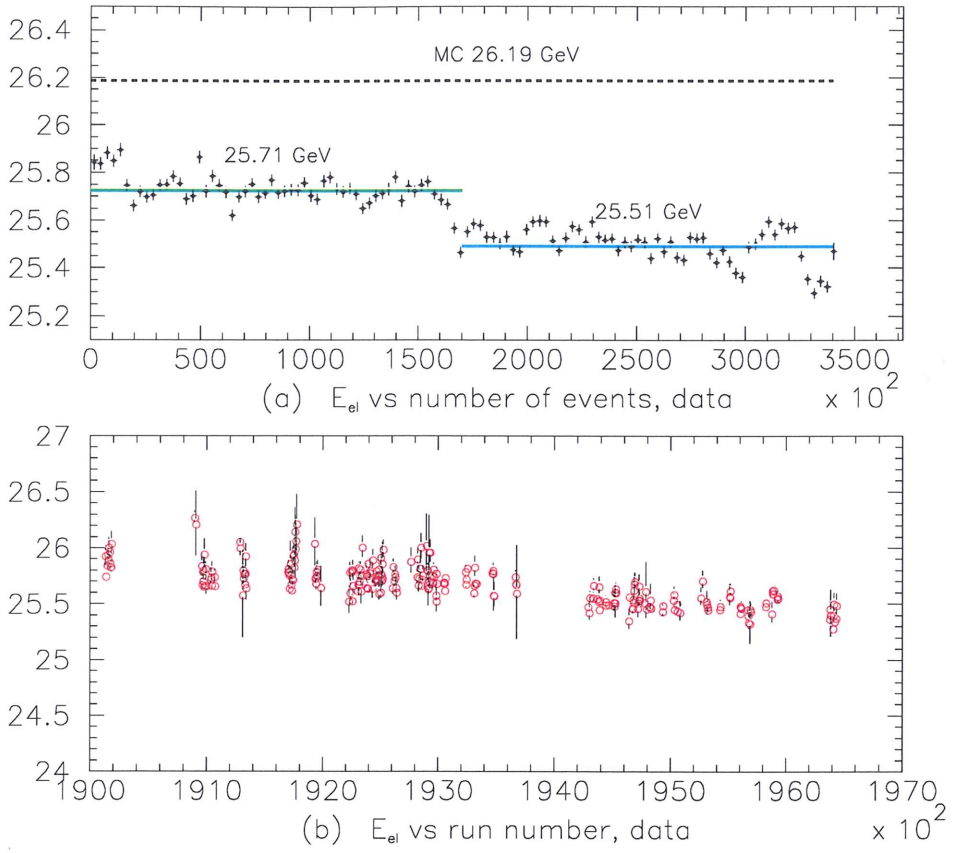


Figure 4.2: The same plots as in Figure 4.1 but after cut on runs with highly deviated mean electron energy $\langle E_{el}^{run} \rangle$.

Although this method is less accurate it is useful for the first analyzes of data and for the rejection of the runs with the bad electron mean energy (Section 4.4). In the following analysis the runs with mean electron energy $\langle E_{el}^{run} \rangle$ within approximately $2\sigma$ around the overall mean energy $\langle E_{el} \rangle$ for a given interval of run were accepted.

Another possibility is to recalibrate Spacal cell by cell. The calibration constants could be obtained from DST1 data tapes by a combination of methods described in Section 3.3. It is more complicated but more precise and it can be improved by a number of additional corrections [22] applied to both the data and Monte Carlo, i.e.

- **Inside cell calibration:** Correction to a center of cluster position inside the hottest cell. The difference of the energy response in the center and at the corners was found to be less than 1 %.

- **Circular correction:** The dead material in front of the Spacal causes a one percent change of the measured energy at the Spacal radius of 25 cm. This correction was not applied to the Monte Carlo.

- **Supermodules crack correction:** The cracks between the supermodules contribute up to 2 % variations of energy scale and they are not correctly described by the Monte Carlo simulations. The correction was done as a function of $R_{box} = \max(|X_{Sp}|, |Y_{Sp}|)$.

This method was developed by A. Glazov [22] and it will be used only for comparison with the rough recalibration method.

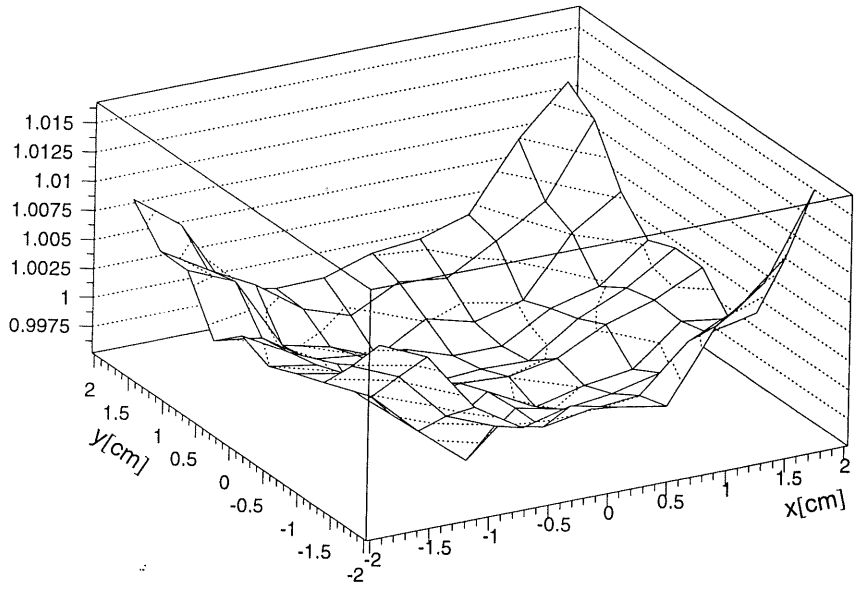


Figure 4.3: Dependence of calibration constants on the position of a cluster inside the hottest cell.

## 4.2 $\pi^0$ Spacal Calibration Cross-Check

The $\pi^0$ calibration is an additional calibration method which can be used to validate the procedures mentioned in Section 3.3. This method is useful because the $\pi^0$ is produced in abundance in photoproduction, has a well determined mass, and provides a low-energy cross check of the calibration determined with the kinematic peak method. At the same time, it is less useful for providing a calibration suitable for applications to high energy electrons.

The main idea is to find a $\gamma\gamma$-pair which originates from $\pi^0$ decay. The invariant mass of this pair has to be equal to the invariant mass of $\pi^0$ ($M_{\pi^0}$).

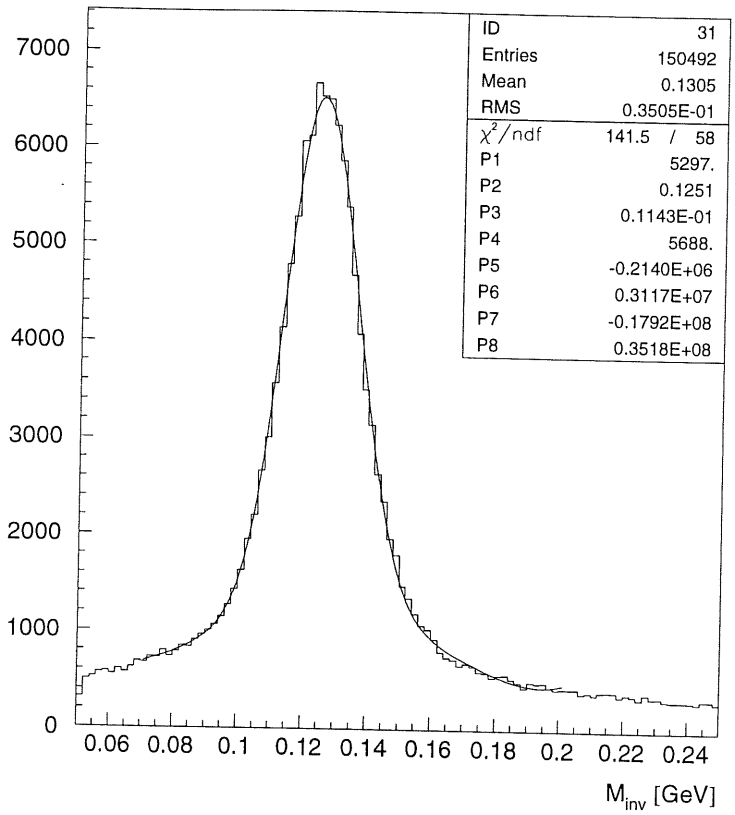


Figure 4.4: Distribution of invariant mass $M_{inv}$ of selected $\gamma\gamma$-pairs.

Unfortunately there is no hint how to separate two $\pi^0$ photons from photons which were found in an event, therefore the $\gamma\gamma$-pair with invariant mass $M_{inv}$ closest to that of the $\pi^0$ is chosen. The distribution of $M_{inv}$ (Figure 4.4) is fitted to the gaussian function added to an polynomial. The parameter which represents the maximum of the gaussian should be equal to $M_{\pi^0}$. Possible difference indicates inaccuracy in global Spacal calibration i.e. nonlinearity of calibration down to low energies.

Distribution of $M_{inv}$ in Figure 4.4 corresponds to the events from run-range 190130-196435 with energy recalibration mentioned in Section 4.1. The value of gaussian maximum (parameter P2, let's denote it as effective mass $M_{eff}$) is about 0.125 GeV and is about 7.3 % below $\pi^0$ mass (0.135 GeV).

Furthermore we can classify $\gamma\gamma$-pairs according to the energy of the most energetical photon $E_{max}$. Distributions of $M_{inv}$ for different intervals of $E_{max}$ up to 8 GeV are shown in Figure 4.5. For $E_{max} >$ 8GeV the opening angle of the photons is too small to give two separate clusters in Spacal. The value of $M_{eff}$ is increasing with $E_{max}$. This could be an effect of miss-calibration of individual cells or of the cluster reconstruction in the Spacal. Monte Carlo simulations were

used to correct for the acceptance of $M_{inv}$. Dependence of effective mass $M_{eff}$ on $E_{max}$ is displayed in Figure 4.6(a). The graph (b) shows the same dependence for Monte Carlo. Similar shapes of both graphs indicate that the main source of Spacal undercalibration is the acceptance of $M_{inv}$ which is included in both data and Monte Carlo. Detector acceptance is eliminated in a ratio of both graphs (Figure 4.6(c)) which is not equal to one. This is an effect of miss-calibration of cells for data. They are undercalibrated for low energies.

Moreover the influence of acceptance can be studied. Since $\pi^0$ are produced within jets, the $\pi^0$ cluster could be affected by other hadrons. Therefore a special Monte Carlo simulation was performed where only single $\pi^0$ in each event was generated from the vertex with the angles corresponding to the geometrical acceptance of Spacal. The results (Figure 4.7(a,b)) show a similar dependence as in the case of 'full' Monte Carlo simulations.

In addition another special Monte Carlo was produced where only one photon with known energy was generated in each event and shot into Spacal. Figure 4.7(c) shows the systematic difference between the generated and reconstructed energies. If we correct the cluster energies of gammas of $\pi^0$ decays by the dependence seen in Figure 4.7(c) we observe (see Figure 4.7(d)) an overall shift of the data points with respect to the Figure 4.7(b), but the shape remains the same. Therefore the drop of the effective mass at low $E_{max}$ can not be corrected by a simple recalibration. The reason of this decrease could be in the clustering algorithm and/or in the simulation of low energy showers.

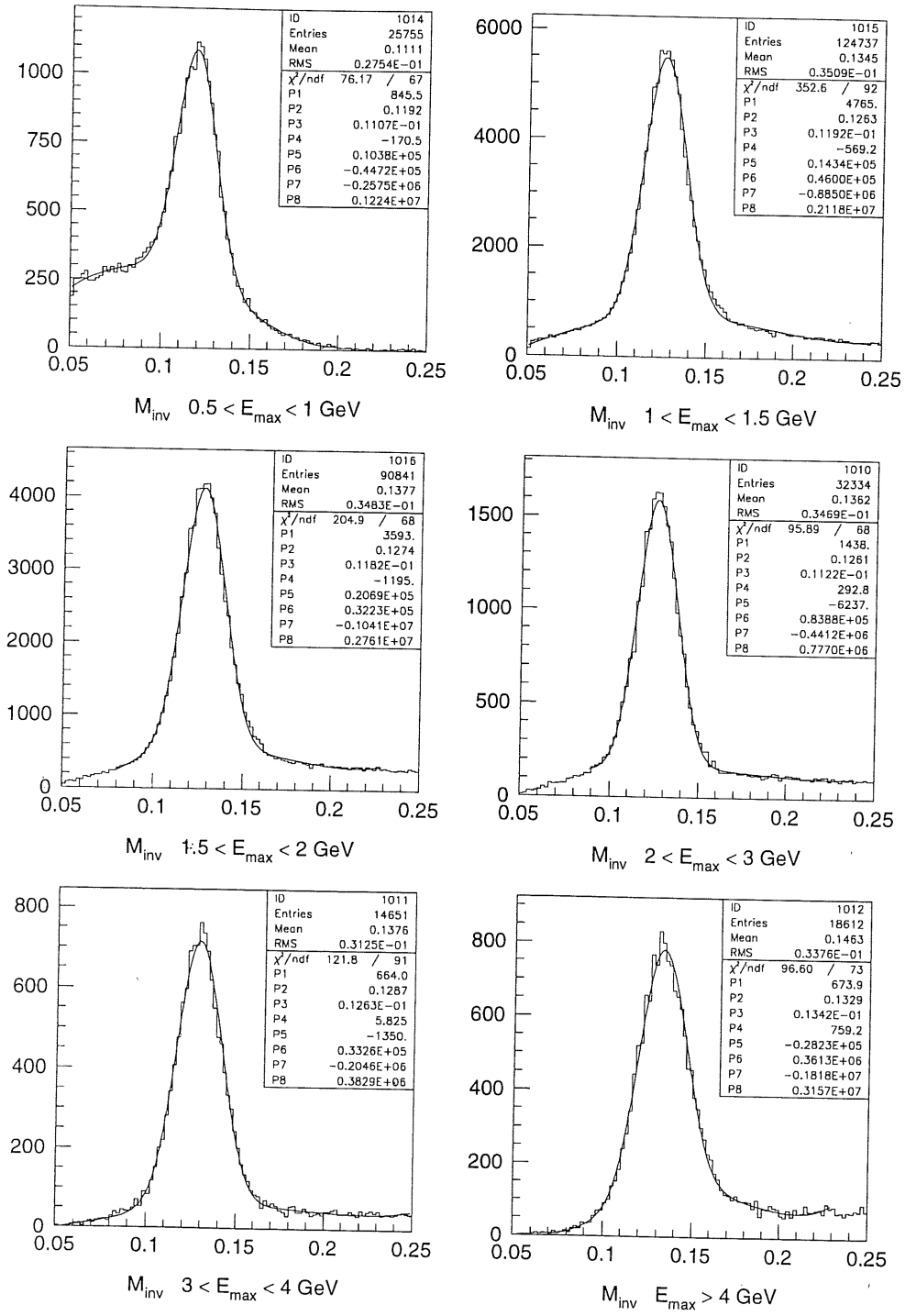


Figure 4.5: $M_{inv}$ for a given intervals in $E_{max}$ the higher of photons energies.

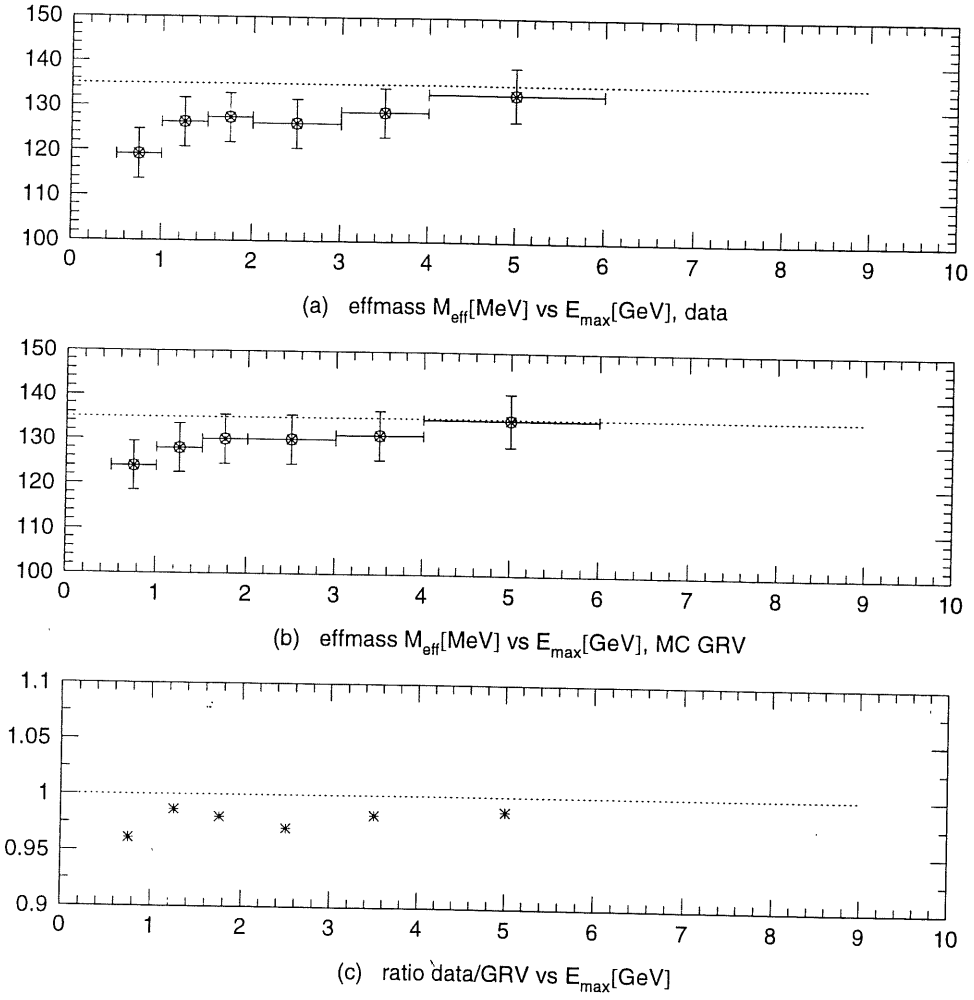


Figure 4.6: Comparison of data and Monte Carlo for $\pi^0$ calibration check.

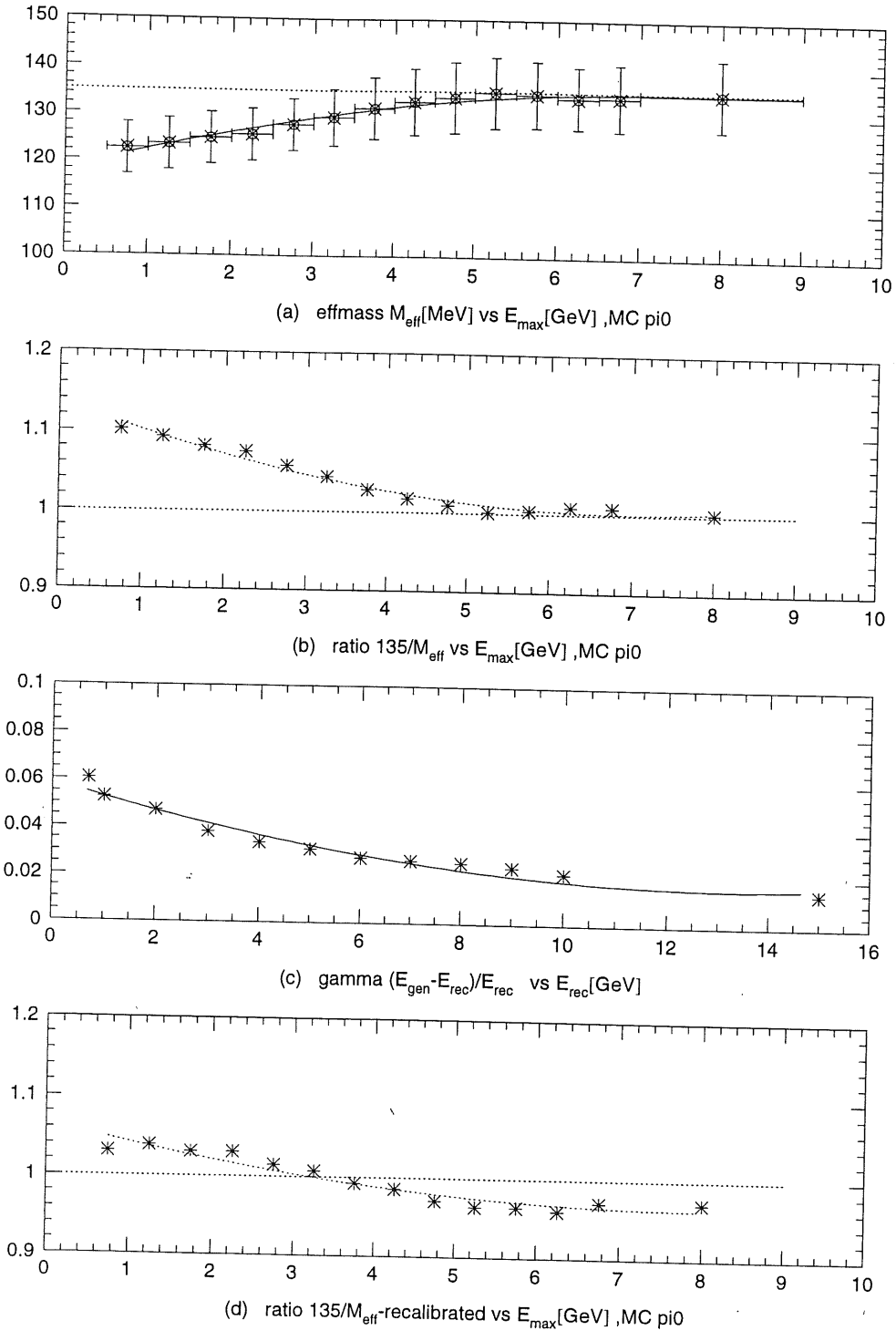


Figure 4.7: Plots of the effective mass $M_{eff}$ (a), the ratio of $135/M_{eff}$ (b,d) vs $E_{max}$ for single $\pi^0$ simulations. The energy resolution of gammas for the single gamma simulations (c).

| Cut | Required condition |
|---|---|
| $e$ energy cut | $E_e > 6.9\,\text{GeV}$ |
| $E - p_z$ cut | $E - p_z > 35\,\text{GeV}$ |
| Hadronic fraction | $< 15\,\%$ |
| Cluster radius | $R_{cl}^{log} < 4\,\text{cm}$ |
| BDC-Spacal link | $DCLBT < 3\,\text{cm}$ |
| $z$-vertex position | $\lvert z_v \rvert < 24\,\text{cm}$ |
| $z$-vertex error | $d_{zv} < 8\,\text{cm}$ |
| vertex type | $\exists$ reconstructed |
| CIP validation | for $E_e < 26\,\text{GeV}$ |
| Fiducial cut | ineff. areas cuts |

Table 4.1: The DIS selection cuts used in the analysis of DST1 1997 data.

## 4.3 Event Selection

In this section the event selection cuts used in the presented analysis are summarized. The list of used cuts is given in Table 4.1, namely

- The event must have a reconstructed vertex with the $z$-coordinate within $\pm 24\,\text{cm}$ around the nominal vertex position ($z = 0\,\text{cm}$).
- An electron candidate is identified as the highest energy deposit cluster in the Spacal. The minimum required energy is 6.9 GeV.
- The lateral size of this cluster (represented by parameter $R_{cl}^{log}$) has to be less than 4 cm. The *log* in superscript refers to logarithmical weighting calculation of the cluster radius. This cut is conveniently denoted as ECRA cut.
- The longitudinal size of the cluster is restricted by the cut on the energy in the hadronic Spacal which has to be less than 15 % of overall cluster energy.
- The selected Spacal cluster has to match a BDC track, i.e. the distance DCLBT between the extrapolated track (Spacal cluster-vertex) and a BDC track is less than 3 cm.
- A cut on $E - p_z$ enables reduction of $\gamma p$ background and radiative events.
- The CIP validation cut is the requirement of CIP pad signal triggered by the electron candidate. This cut enables for high $y$ analysis to reduce photon conversion background (e.g. from $\pi^0 \to \gamma\gamma$) .
- The *fiducial* cuts ensure excluding of inefficiency regions of the H1 detector.

The values presented in Table 4.1 are standard H1 limits which have been determined in the previous analyzes by the extensive study of data and various DIS and photoproduction simulations. The background suppression by the individual selection criteria is illustrated in Figure 4.8 where the cluster energy $E$ of electron candidates is plotted. The number of rejected events is increasing with the decrease of $E$ since the photoproduction background is raising at low $E$.

It is also useful to study the rejection efficiency for individual cuts, which is defined as

$$\epsilon^a = \frac{N^a}{N^a_{all}}, \tag{4.1}$$

where $N^a_{all}$ ($N^a$) defines a total number of events passing all selection criteria excluding (including) cut $a$.

In Figures 4.9 and 4.10 the efficiency $\epsilon^a$ of selected cuts is shown for data and DIS Monte Carlo respectively. The left column ($\epsilon$ dependence on $R_{BDC}$) should be similar for both data and simulation because for $E_e > 20\,\text{GeV}$ the contribution of $\gamma p$ background is negligible. The right column ($\epsilon$ dependence on $E_e$) demonstrates the influence of photoproduction background. The requirement $R > 25\,\text{cm}$ ensures an elimination of fiducial cuts effects[3] in the central part of the Spacal. For high energies the efficiencies are nearly equal to 1 except that of the VERTEX cut. The events with an electron candidate of high $E$ and low angle could not have reconstructed vertex and therefore are eliminated by the vertex cut. The decrease of efficiency for ECRA cut is an effect of wider $e$-shower for low energies of photoproduction events.

## 4.4 Run Selection

Full functionality of the H1 detector is needed in order to achieve the high precision of measurement. The quality of some runs is not sufficient and consequently they are rejected. The following run selection criteria were applied:

- **High voltage:** All relevant components of the detector must be operational. A run is rejected if at least one HV alarm bit is on for more than 5 % of the integrated luminosity recorded in this run. The luminosity is corrected accordingly.

- **Run luminosity:** The integrated luminosity within a run has to be larger than $0.2\,\text{nb}^{-1}$ in order to guarantee the statistical significance.

- **Energy response stability:** The energy of the electron candidates averaged over a run $\langle E_{el} \rangle$ must not deviate too much from the overall mean energy (see Section 4.1).

[3] In order to eliminate *hotspots* and trigger inefficiency regions a number of spatial cuts was applied around the beampipe.

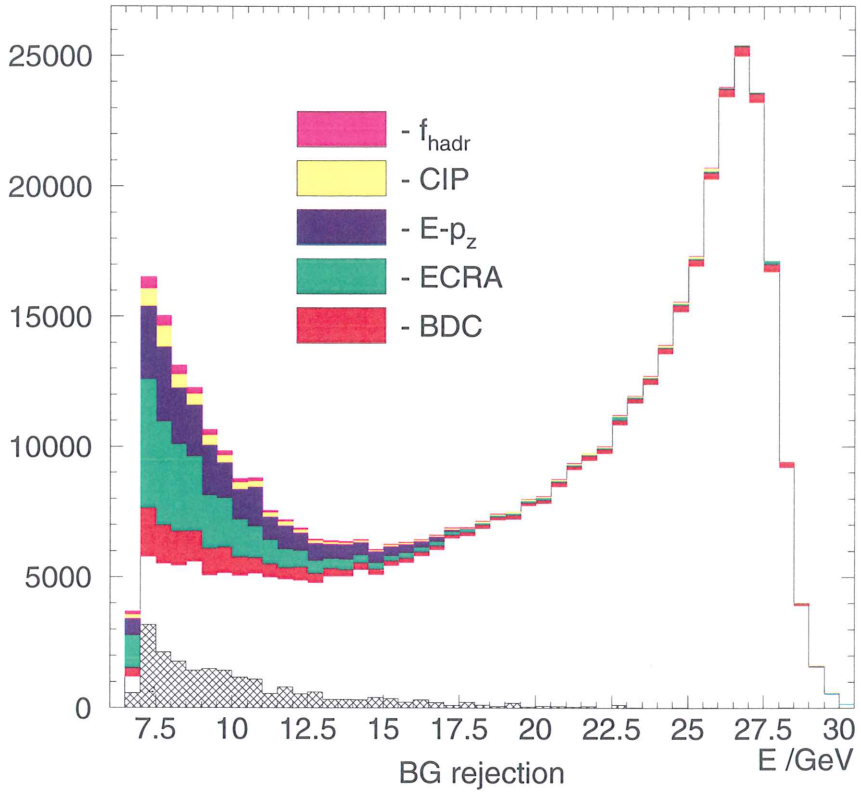


Figure 4.8: Effect of background rejection for individual cuts (data). The cut on $z$-vertex was already applied. The open histogram corresponds to events passed all cuts. The color bands represent events rejected by a particular cut with all other selection criteria applied. The hatched histogram shows an expected amount of remaining background simulated by the photoproduction Monte Carlo (PHOJET).

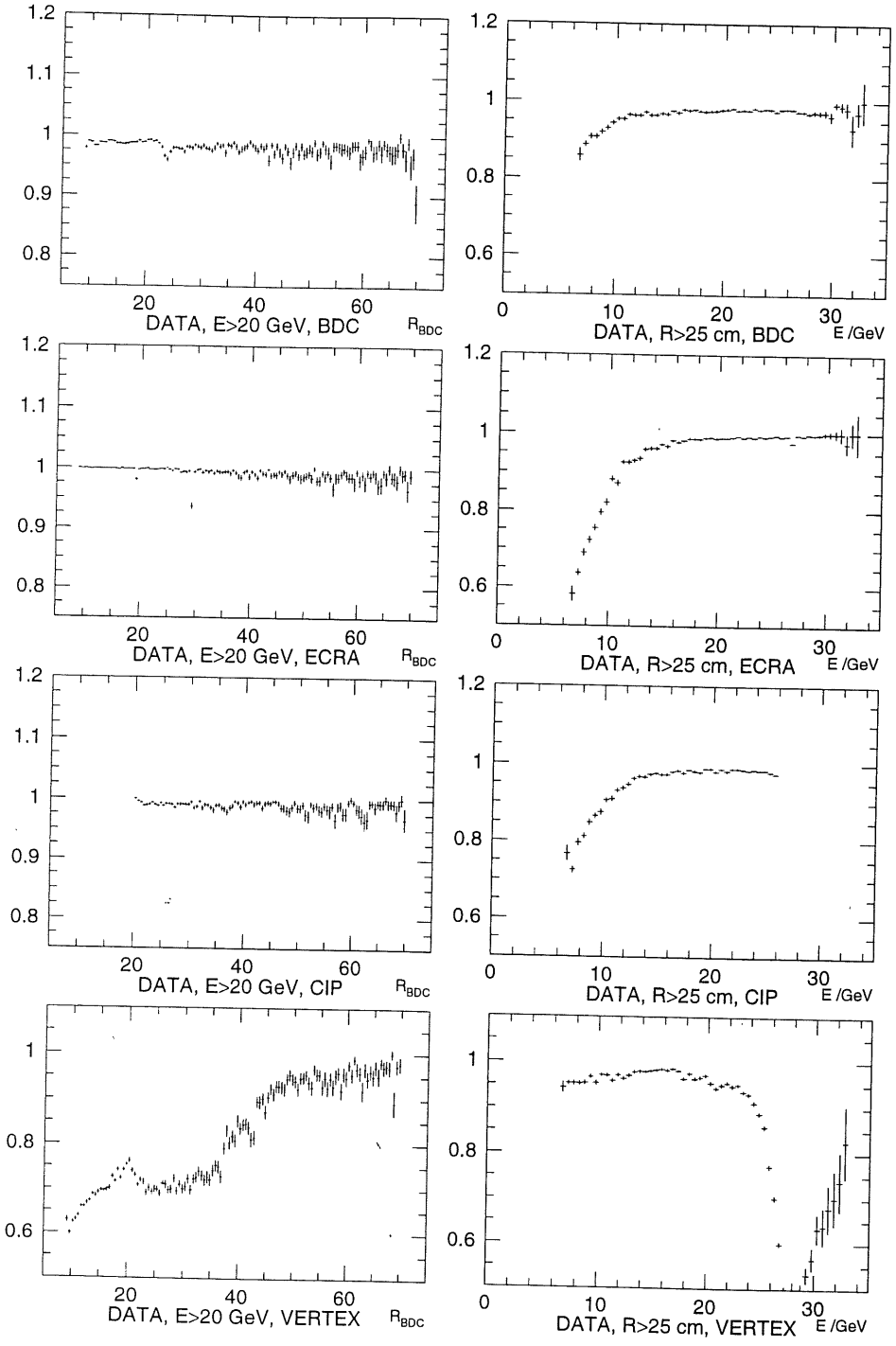


Figure 4.9: The efficiencies of selected cuts (DATA) vs the distance to the beam line ($R_{BDC}$) and vs electron candidate energy.

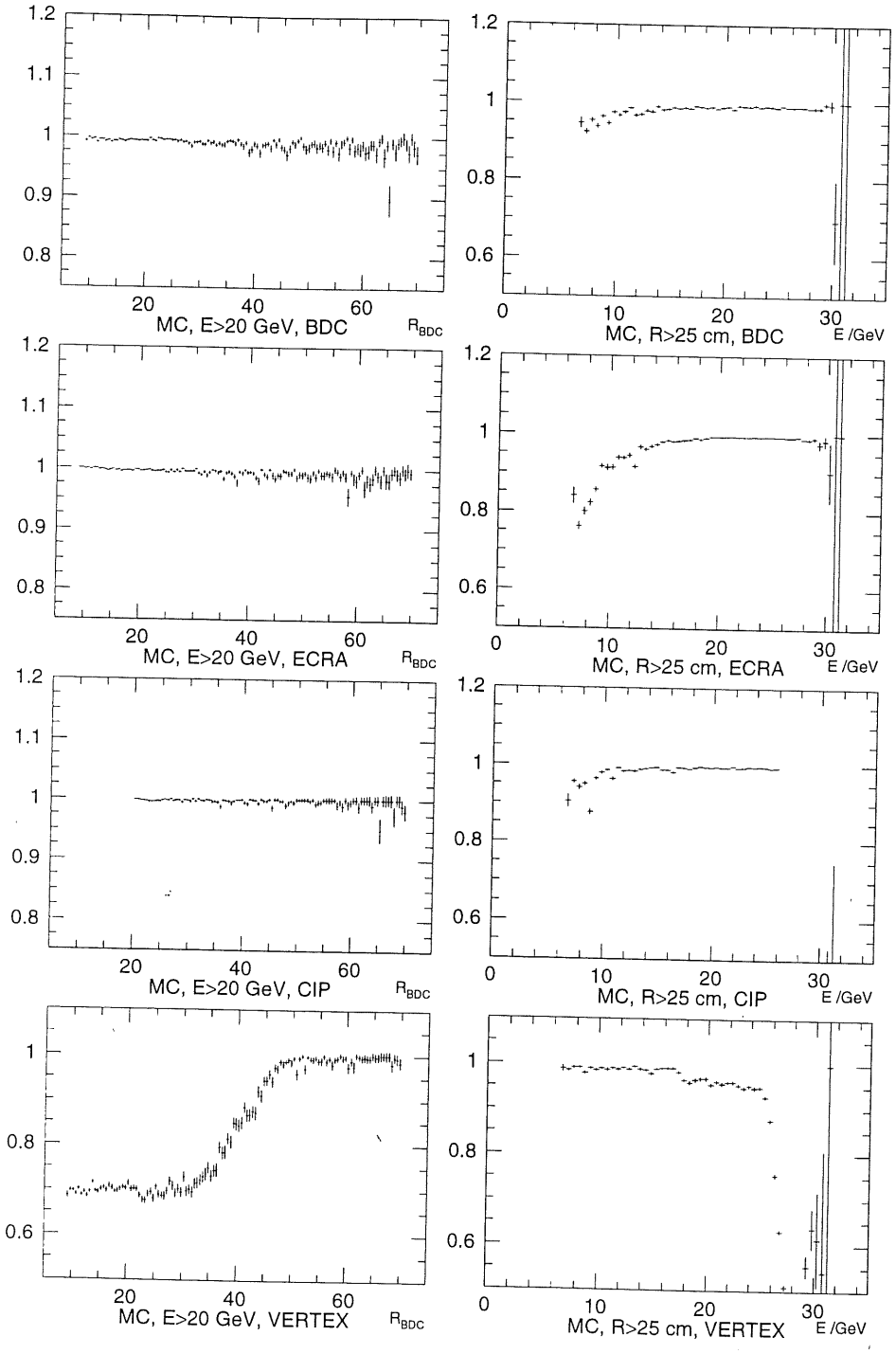


Figure 4.10: The efficiencies of selected cuts, Monte Carlo.

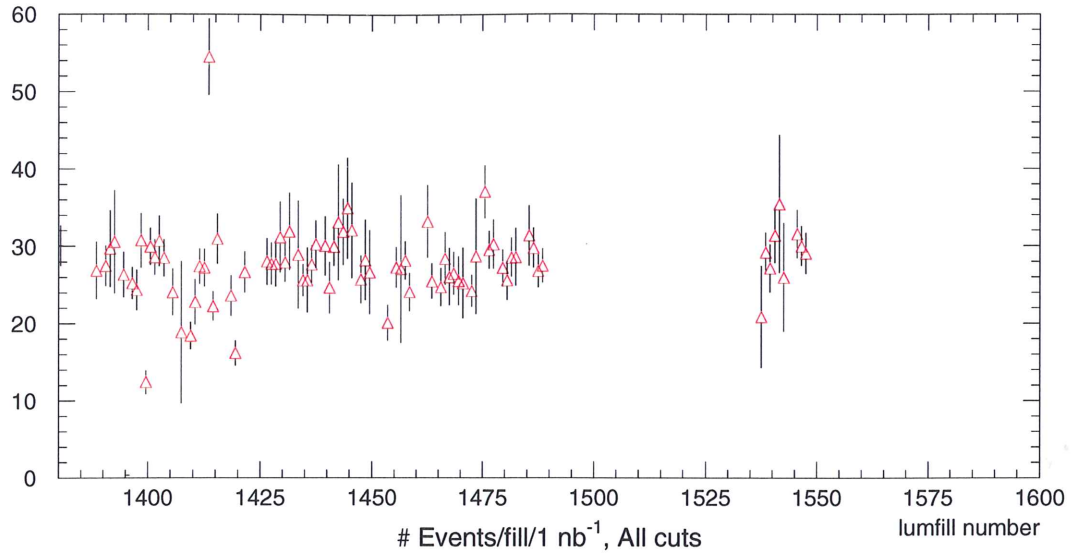


Figure 4.11: Number of events in a given lumfill divided by its accumulated luminosity. All selection criteria and cuts were applied.

- **Events per luminosity:** Number of selected events should be proportional to the luminosity. A luminosity fill (lumfill) is rejected if the number of selected events per luminosity strongly deviates from the overall mean value (see Figure 4.11).

- **$z$-vertex distribution:** A lumfill is accepted if the mean value or $\sigma$ of $z$-vertex distribution does not deviate significantly from mean value of all lumfills. This criterion provides a better comparability with the simulations and is necessary for the correct reconstruction of the event kinematics. For detailed description see Section 4.5.

## 4.5 Analysis of $z$-vertex

The mean position $\langle z_{vtx} \rangle$ and the spread $\sigma_{vtx}$ of the $z$-vertex directly affect the reconstruction of event kinematics. They are luminosity fill dependent as it is demonstrated in Figure 4.12 where they are plotted versus lumfill number.

The HERA proton bunch has a complicated longitudinal structure, which means that except the main bunches neighbouring *satellite* bunches can occur. Their signature is the presence of additional peak in $z$-vertex distribution (see Figure 4.13). The H1 luminosity system can not distinguish the luminosity of main bunches from that of the satellites and measures both together. An off-line correction of the luminosity is therefore needed. In the analyzed interval of the lumfills a contribution of the satellite bunches to the luminosity is very

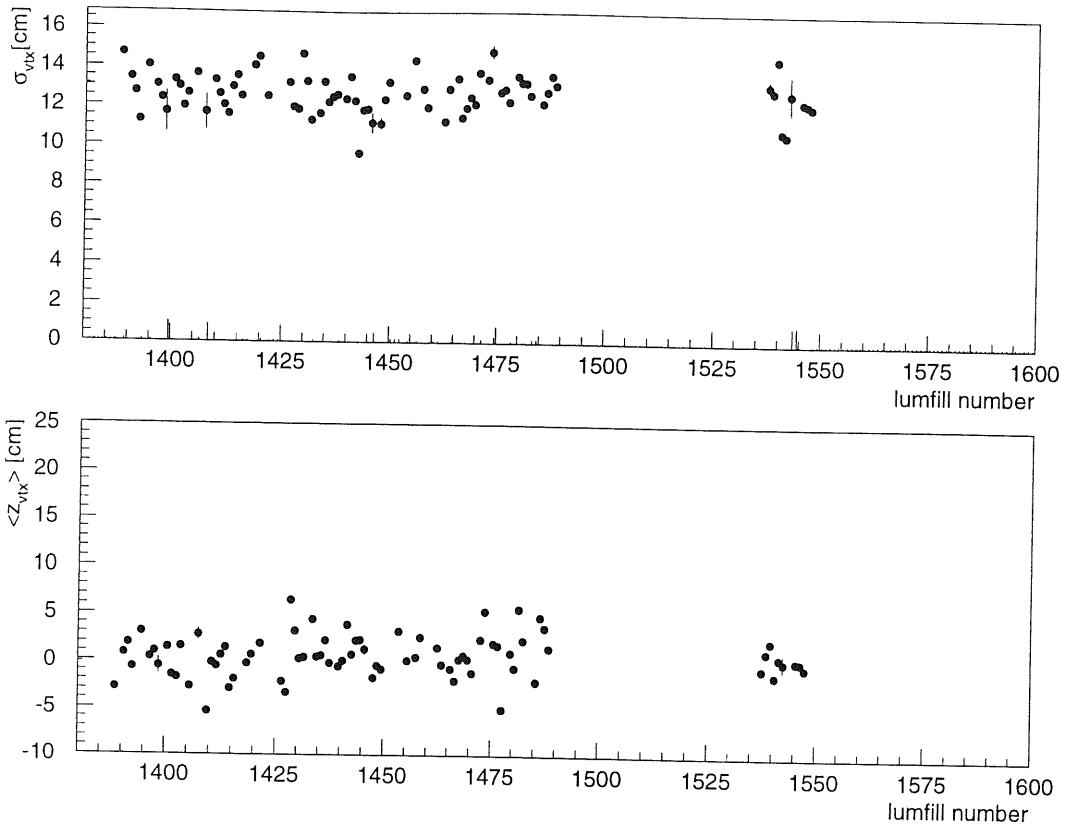


Figure 4.12: Sigmas (top) and mean values (bottom) of the gaussian fits to the distribution of the $z$-vertex coordinate for each lumfill.

low. Only three lumfills with a satellite signature were found and are displayed in Figure 4.13 together with three normal lumfills.

Since the Monte Carlo is generated with a fixed z-vertex distribution of events, which is not in general compatible with the measured one, there is a necessity to reweight Monte Carlo events according to the measurement. It can be easily done by the following method:

1. The z-vertex distributions for both simulations and data are normalised to each other.

2. Distributions are fitted to a gaussian formula ($g_{data}(z)$ for data and $g_{mc}(z)$ for simulation).

3. The simulated events are multiplied by a reweighting function $f(z) = g_{data}(z)/g_{mc}(z)$, which is displayed in Figure 4.14.

The normalisation in step 1. should ensure that the luminosity of Monte Carlo after reweighting is equal to that before. Figure 4.15 illustrates the z-vertex

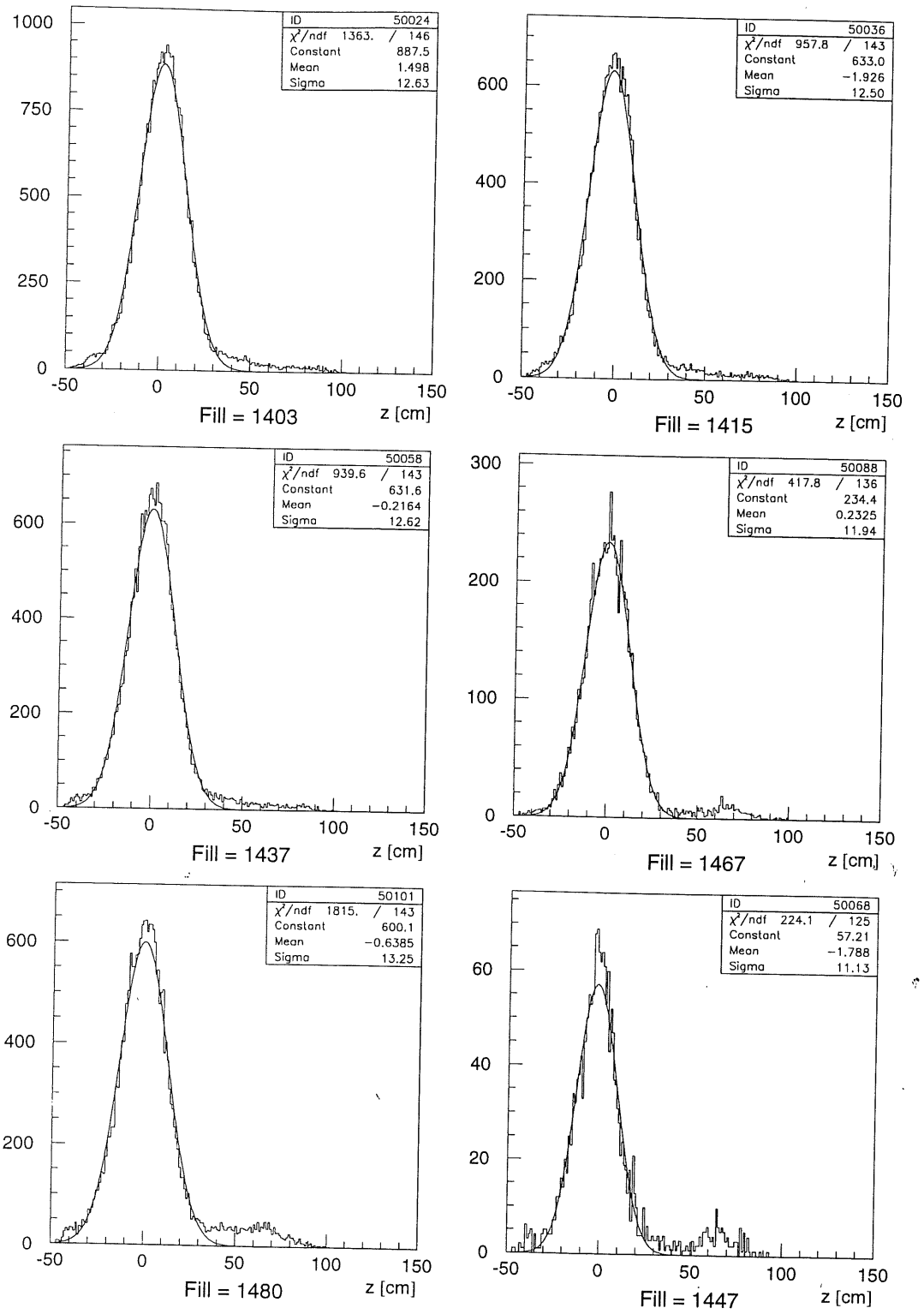


Figure 4.13: Distributions of $z$-vertex for some lumfills. Lumfills No. 1467, 1480 and 1447 contains a peak signature of satellite bunches at the higher values of the $z$-coordinate. The lines represent a gaussian fits.

distribution for Monte Carlo before (full line) and after (hatched) reweighting and for data (dots). The seeming disagreement between reweighted Monte Carlo and data is caused by the absence of photoproduction background simulations.[4]

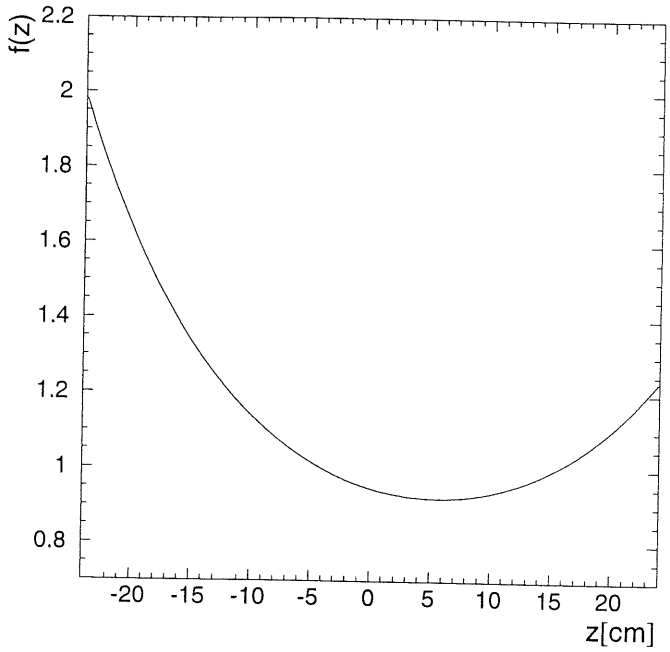


Figure 4.14: Z-vertex reweighting function.

## 4.6 Trigger Selection

The brief description of the H1 trigger system and the Spacal IET trigger was presented in Section 2.3 and 3.2. The definitions of subtriggers relevant for our analysis are listed in Table 4.2. Each subtrigger requires a minimum energy deposit in the Spacal calorimeter (IET[5]) and a combination of additional trigger elements (e.g. v:4, z:0, ...). The elements of type 'v' are related to the requirement on absence of VETO, BToF and Spacal ToF background signals. The elements 'f' demand a check of FToF and PToF signals. More important is the element z:0 for L1 vertex trigger [23], which is based on the fast histogramming of hits in the $z$-chambers CIZ and COZ (Section 2.2.1) and the search for the histogram maximum. Finally, t:0 refers to vertex trigger condition.

Due to the high background of proton-gas, proton-pipe wall and photoproduction interactions at low $Q^2$ DIS some subtriggers exhibit high rates. Therefore

[4]Graph corrected to the photoproduction background is shown in Figure 5.1.

[5]IET trigger covers all Spacal except the central part which is covered by special central IET trigger and will not be used in the following.

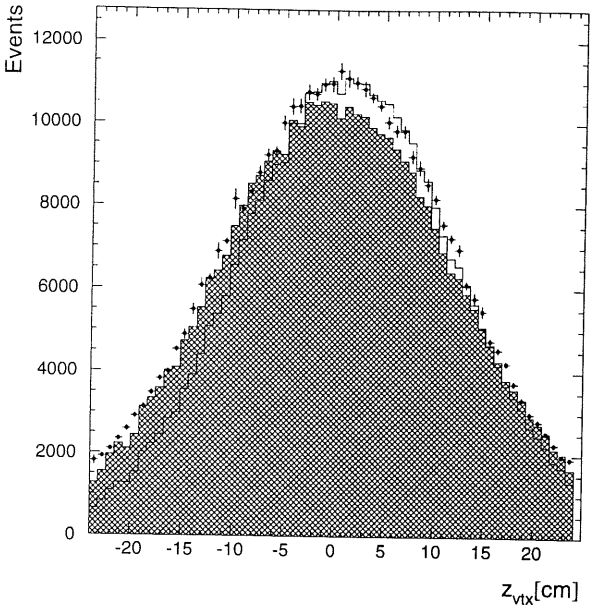


| | DATA |
|---|---|
| $z_{mean}$ | 0.272 cm |
| sigma | 12.03 cm |
| | MC non rew. |
| $z_{mean}$ | 1.355 cm |
| sigma | 10.74 cm |
| | MC reweighted |
| $z_{mean}$ | 0.306 cm |
| sigma | 12.03 cm |

Figure 4.15: The z-vertex distributions for Monte Carlo before (full line) and after (hatched) reweighting. Dots represent data. Parameters of the gaussian fits are listed in the table.

| Subtrigger | Definition | def. prescale min. | max. |
|---|---|---|---|
| s0 | IET > 2 v:4, f:1 | 1 | 5 |
| s1 | IET > 2 v:3, z:0, f:1, t:3 | 1 | 1 |
| s3 | IET > 2 Spacal-ToF, v:3, f:0 | 1 | 1 |
| s9 | IET > 1 v:8, f:1, t:3, z:0 | 1 | 3 |

Table 4.2: The definitions of used subtriggers, s0 is the minimum bias trigger. Trigger threshold for IET>1 (IET>2) was set to 2 GeV (6.5 GeV).

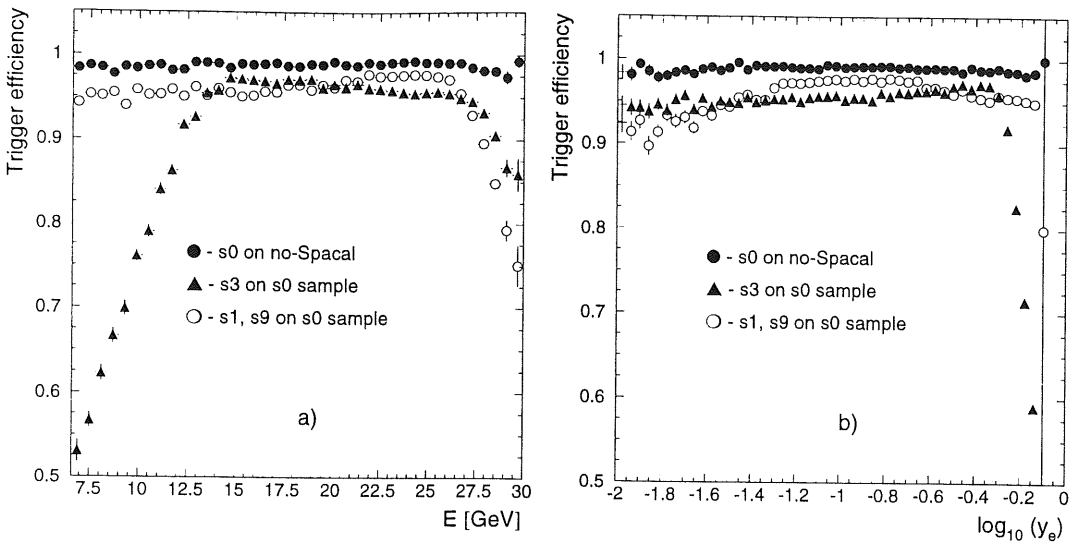


Figure 4.16: The efficiencies of subtriggers as a function of electron energy $E_e$ (a) and $\log_{10}(y)$ (b).

such subtriggers are *prescaled*, which means that event is triggered by a subtrigger only every e.g. fourth (for prescale factor 4) trigger signal of this subtrigger.

A signal from a subtrigger generates a *raw* trigger bit. If the prescale condition is passed an *actual* trigger bit is set.

Default prescale factors of used subtriggers are listed in Table 4.2. The subtrigger prescale factor depends on the *run phase* (1-4) which represents the functionality of H1 detector (run phase = 1 is low functionality). Higher trigger prescales corresponds to a lower run phase.

The selection of events is based on the following algorithm [22]. The term subtrigger now refers to one of the subtriggers used in the presented analysis (i.e. s0, s1,s3 or s9)

1. If an event is not triggered by any of the subtriggers (i.e. actual bits are not set) it is rejected.

2. The event weight is equal to the lowest prescale factor of actual subtriggers.

3. If there exists any raw subtrigger with prescale factor lower than the weight of the event, the weight of event is set to 0.

The mean idea of this algorithm is described in Appendix B in more details.

## 4.7 Trigger Efficiencies

The efficiency of a subtrigger is calculated as a fraction of events with raw bit set on in a sample triggered by an independent set of subtriggers or a more general

subtrigger.

The behaviour of subtrigger s0 is determined from the data using a sample of events triggered independently of the Spacal triggers. Events has to pass the DIS event selection criteria to be included in the sample. Figure 4.16 shows the trigger efficiency for the subtriggers s0, s1, s3 and s9 as a function of scattered electron energy $E_e$ (a) and the logarithm of the inelasticity $\log_{10}(y)$ (b). The efficiency of subtrigger s0 is above 97.5 % everywhere with the mean value of 99 %.

The efficiencies of the remaining subtriggers are calculated from a sample of events triggered by s0.

The fall of s3 efficiency towards lower $E_e$ (high $y$) is caused by the trigger element Spacal ToF which has the energy threshold of $\approx 15\,\mathrm{GeV}$.

The vertex requirement of subtriggers s1 and s9 causes a decrease of their efficiency for lower $y$. i.e. for high $E_e$. Difference between these two subtriggers is in the lower IET and hadronic Spacal-ToF thresholds in s9 subtrigger. Moreover s9 requires a topological cut on the L2 trigger level. : $\mathrm{R} > 20\,\mathrm{cm} \wedge \mathrm{IET} > 1$. The event selection cut on the scattered electron energy is higher than both thresholds and the fiducial cuts exclude the inner part of the Spacal anyway. These facts causes an identity of the selection ability of both subtriggers in the sample of selected events. The s9 subtrigger due to its higher prescale factor rarely triggers an event.

# Chapter 5

# Results

The results presented below are preliminary since they were obtained by analysing DST1 tapes only and using Monte Carlo simulations for the 1996 running conditions. During the preparation of this thesis the n-tuples from the new simulations of 1997 running conditions have not yet been available.

In Section 5.1 the comparison of basic distributions for data and Monte Carlo is presented. The results concerning the proton structure function are shown in Section 5.2 for both Spacal recalibration methods. The estimation of the gluon density by the Prytz method is given in Section 5.3.

## 5.1 Control Plots

After the run selection mentioned in the previous chapter the total integrated luminosity of data reached $2360\,\mathrm{nb}^{-1}$. The corresponding Monte Carlo luminosities are $2107\,\mathrm{nb}^{-1}$ and $105\,\mathrm{nb}^{-1}$ for DIS and photoproduction respectively. The simulation was performed by the Monte Carlo package DJANGO for DIS and PHOJET for the photoproduction background. A subsample of 400000 DIS MC events was simulated in the Prague computer centers on the SGI Power Challenge machines.

In Figure 5.1 the comparison of the basic distributions for the rough method recalibrated data (dots) and Monte Carlo (full line) is presented. Filled histograms correspond to $\gamma p$ background estimated by Monte Carlo.

The disagreement is seen in the distributions of the scattered electron energy (top-left). The corresponding distribution for the precise method (mentioned in Section 4.1) is plotted in Figure 5.2. It is apparent that the global energy recalibration of all Spacal by only one constant is not sufficient approach and the cell-by-cell method is needed.

Besides the electron energy, $\theta$ angle (top-right) was used to evaluate event kinematics. $\theta$ is determined using the cluster radius position $R_{bdc}$ (bottom-right) evaluated by BDC. The cluster radius position $R$ (bottom-left) evaluated by the

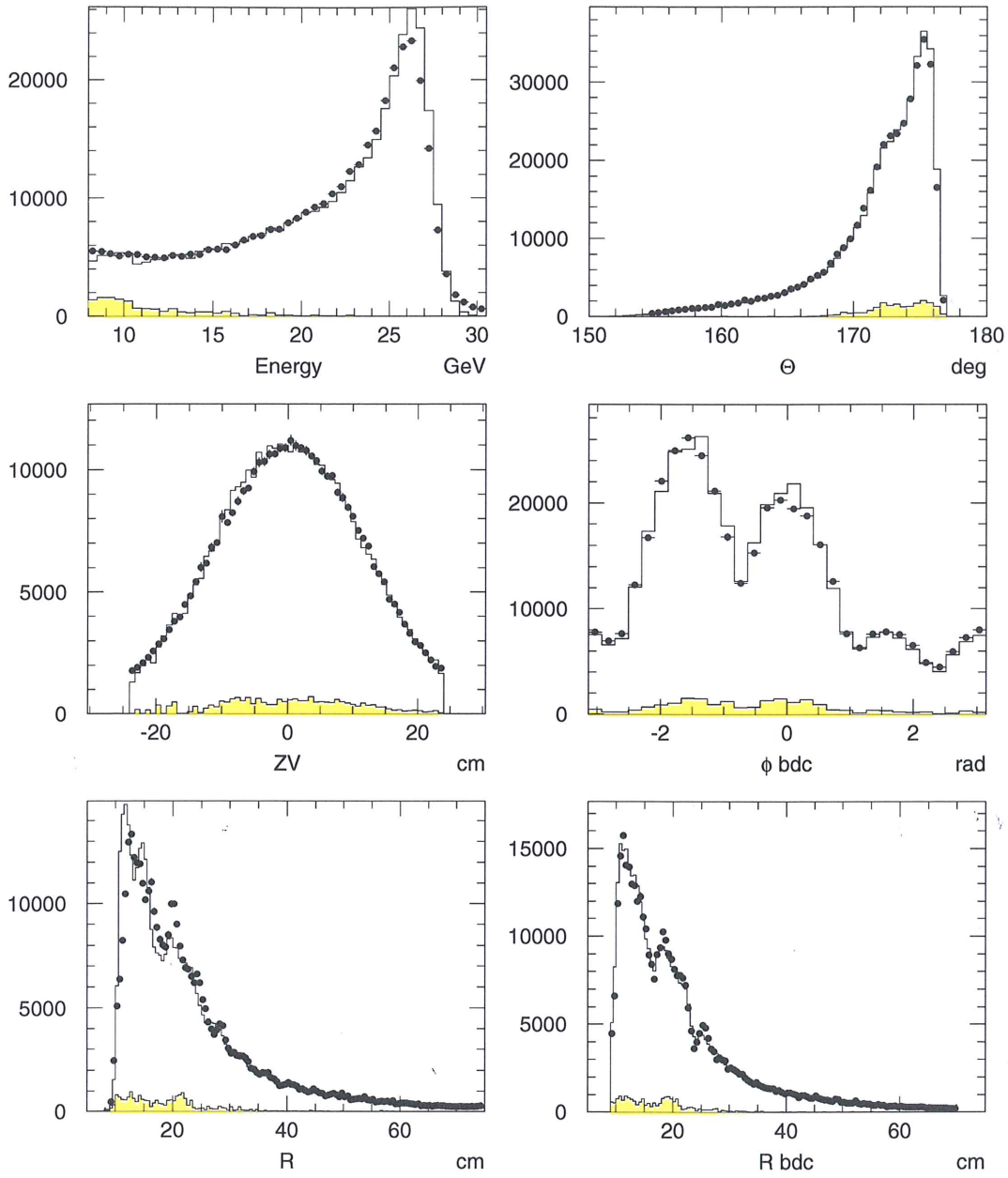


Figure 5.1: Control distributions for 1997 DST1 data (dots) and 1996 simulations (solid line). Filled histograms represent the $\gamma p$ background.

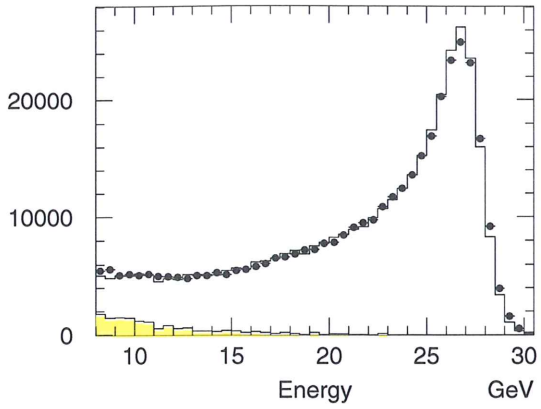


Figure 5.2: Energy distribution with a more precise calibration method used (Section 4.1).

Spacal itself is less accurate due to a non-precise determination of shower shapes.

Figure 5.3 shows the distributions of kinematic variables: Björken scaling variable $x$, square of transferred momentum $Q^2$ and inelasticity $y$. Left column corresponds to the rough recalibration method, right one to the precise method. The inelasticity $y$ variable is the most sensitive one to the measurement errors. For the rough recalibration the disagreement between data and MC is apparent whereas the more precise recalibration gives a perfect agreement with the simulations. This fact indicates the good quality of the precise cell-by-cell recalibration algorithm.

The distribution of electron energy in $Q^2$ bins for the precise recalibration method is plotted in Figures 5.4 and 5.5. It allows to estimate the lower values of $Q^2$ from which the extraction method of $F_2$ can be used. The agreement between data and Monte Carlo is good for higher values of $Q^2$, it is worse for the lower ones. A reasonable lower edge for this analysis is $Q^2 = 2.5\,\mathrm{GeV}^2$.

## 5.2 $F_2(x, Q^2)$ Results

The proton structure function $F_2(x, Q^2)$ is determined at the centre of $x$ and $Q^2$ bins using the equation (1.36). In Figure 5.6 the structure function in bins of $Q^2$ between $2.5\,\mathrm{GeV}^2$ and $60\,\mathrm{GeV}^2$ for the rough electron energy recalibration method is shown. The electron method for the reconstruction of the kinematics was used with the following cut on $y$

$$0.05 < y < 0.55. \tag{5.1}$$

The curves represent the H1 1994 $F_2$ fit which was used as an initial $F_2$ function for this analysis. The error bars correspond to the statistical and systematical errors added in quadrature. Because it is difficult to obtain correct systematical

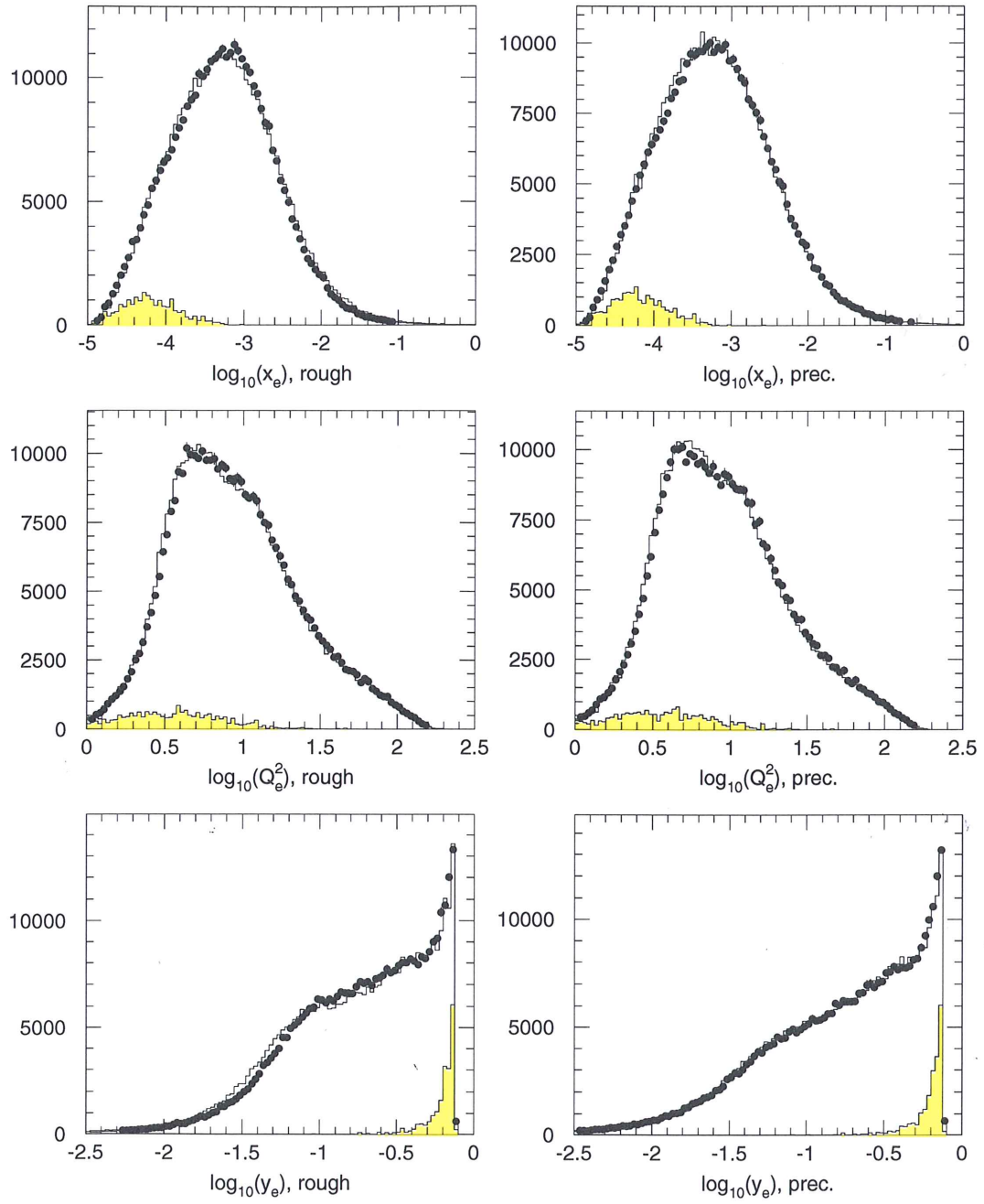


Figure 5.3: $Q^2$, $x$ and $y$ distributions data (dots) and simulations (continuous line) for electron method. Filled histograms represent the $\gamma p$ background.

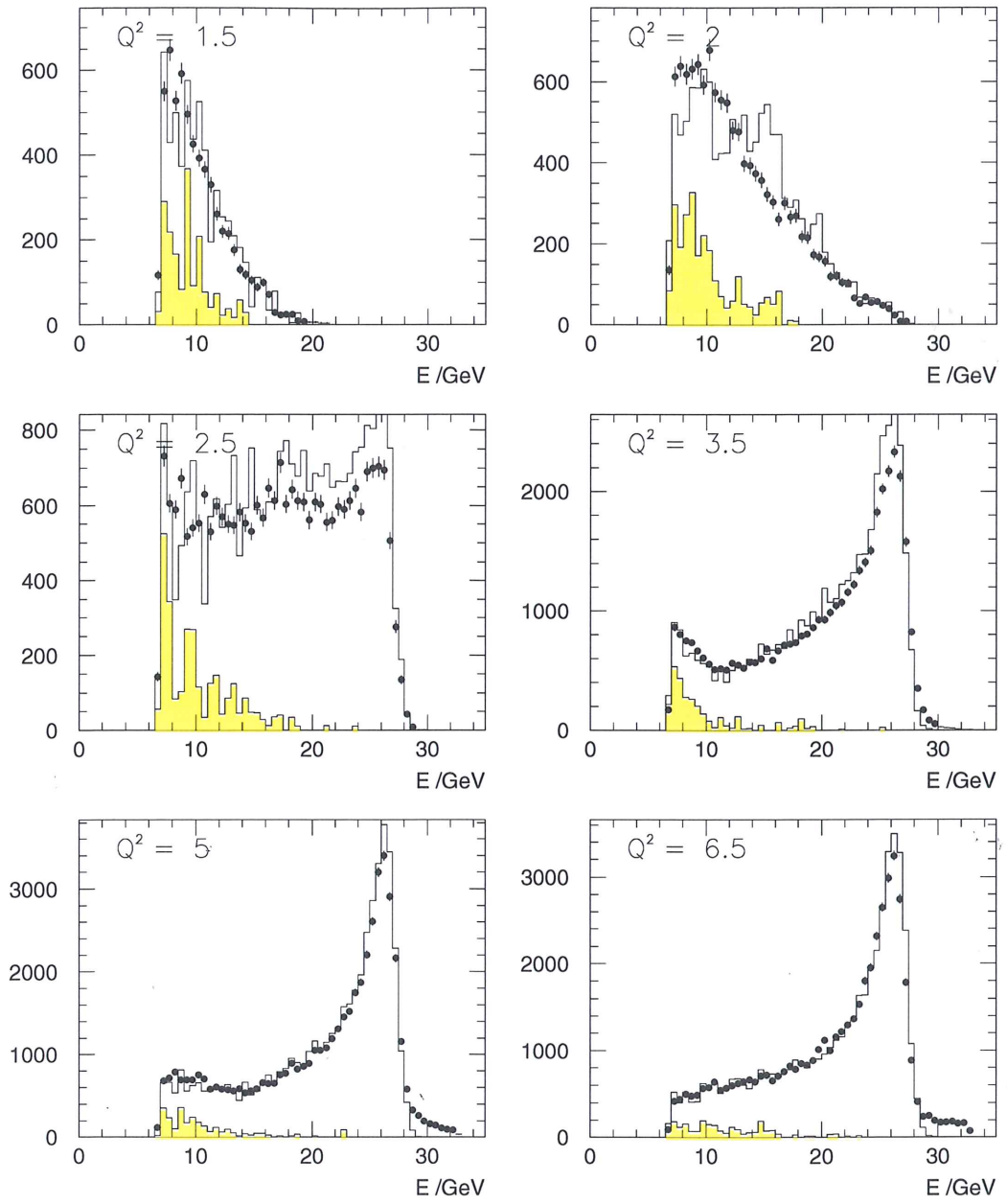


Figure 5.4: Distribution of energy in individual $Q^2$ bins for lower bins. Corresponding $Q^2$ [GeV$^2$] of the bin centers is in the top-left corner of each graph.

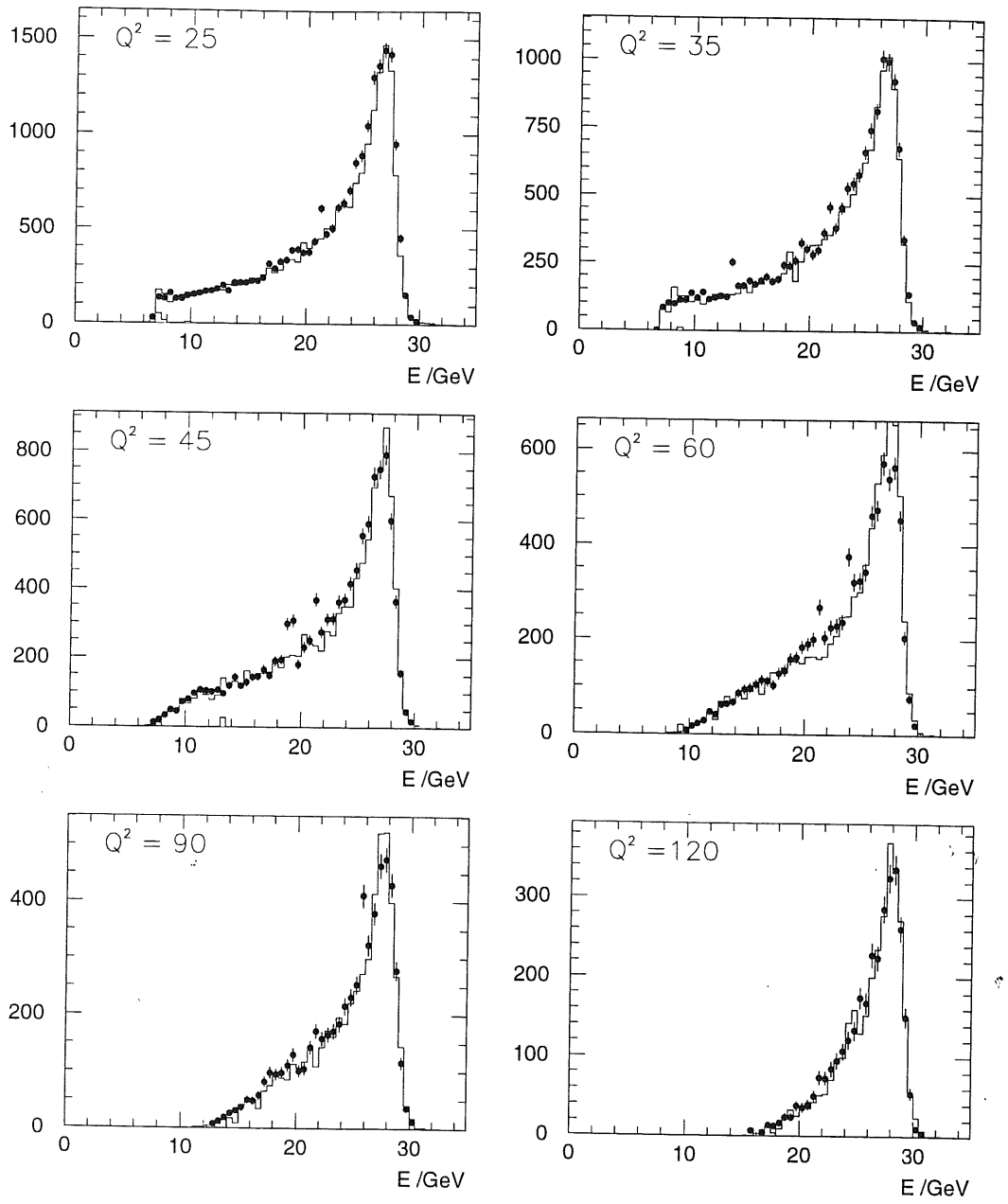


Figure 5.5: Distribution of energy in individual $Q^2$ bins for higher bins. Corresponding $Q^2$ [GeV$^2$] of the bin centers is in the top-left corner of each graph.

errors for DST1 rough data and non-actual Monte Carlo, they were taken from the analysis of 1994. Due to the high statistics, the statistical errors are negligible and only the systematical ones are relevant.

In Figure 5.7 the results of the $F_2(x, Q^2)$ structure function measurement for the precise recalibration and electron method are plotted. The full line represents the H1 1994 fit and the dashed line our fenomenological fit to the measured $F_2(x, Q^2)$ with the function

$$F_2(x, Q^2) = a \cdot x^{-b \cdot \left(\log\left(\frac{\log Q^2/d^2}{\log c/d^2}\right)/\log\frac{e}{x}\right)^f}, \tag{5.2}$$

where $a - f$ are parameters. This parametrization is well applicable for low $x$ kinematic region.

Although the precise method gives more accurate determination of the kinematic variables than the rough method, the extracted structure functions are very similar. In comparison with the H1 1994 fit both exhibits lower values for low bins of $Q^2$ and higher values for higher bins.

The measured $F_2$ structure function as a function of $Q^2$ is for the precise recalibration method plotted in Figure 5.8.

## 5.3 Gluon Density

The gluon density function $G(x) = xg(x)$ was estimated with the approximate Prytz's method described in Section 1.7 using the fit to the measured structure function which was mentioned above. The results are plotted in Figure 5.9 for two values of $Q^2$ (5 and 20 GeV$^2$). Hatched areas correspond to the 20 % error of the measurement (see Section 1.7). The H1 gluon density $G(x)$ published in 1995 [26] is shown in Figure 5.10 at $Q^2 = 20\,\mathrm{GeV}^2$. It was extracted with the NLO $\log(Q^2)$ DGLAP evolution equations, where starting from $Q_0^2 = 4\,\mathrm{GeV}^2$, the gluon density and the quark densities are evolved to higher $Q^2$ values.

Our estimate of the gluon density function quite agree with the H1 1995 gluon density. Both exhibits a strong rise towards low $x$.

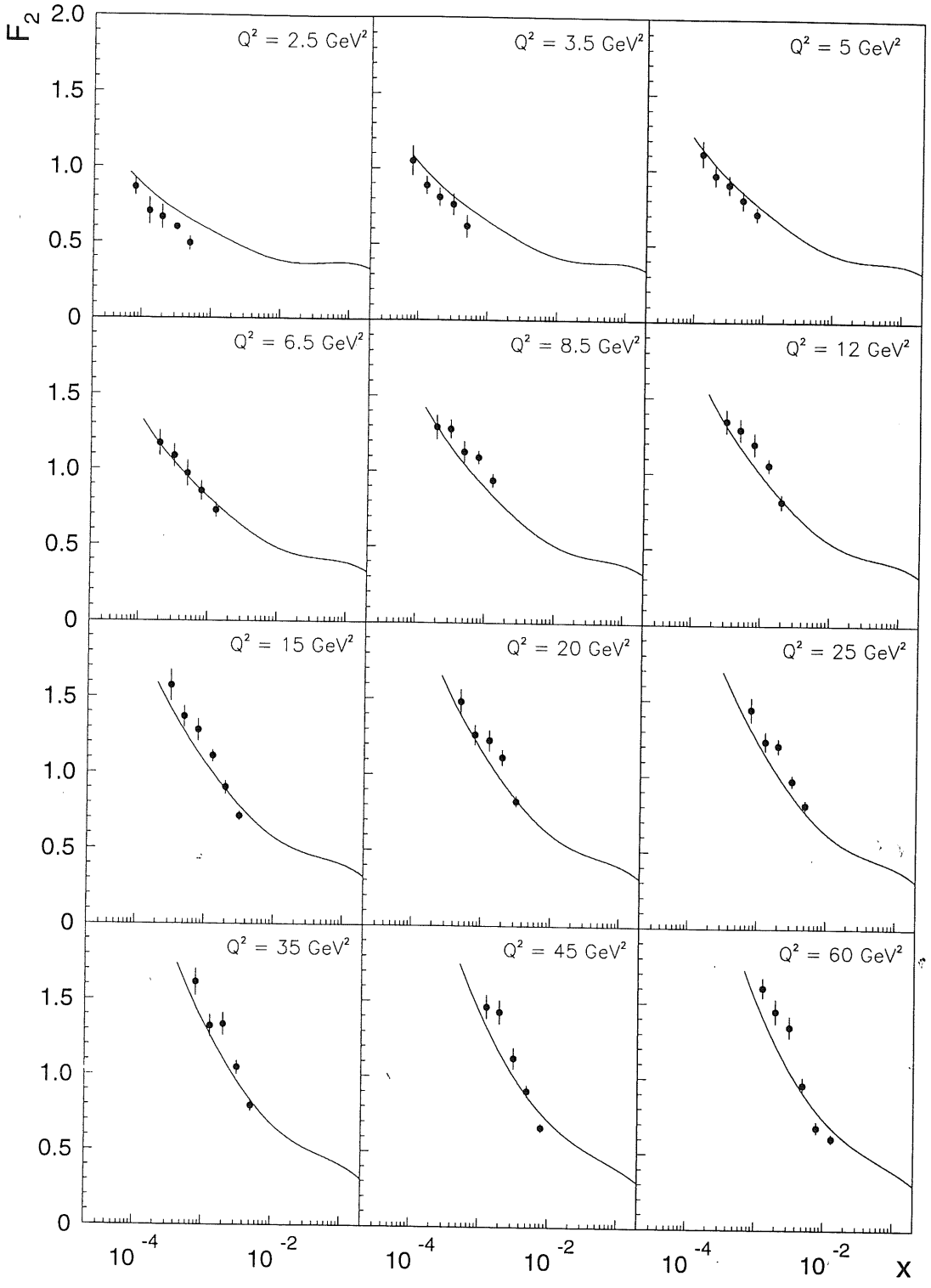


Figure 5.6: Measurement of the proton structure function $F_2(x, Q^2)$ as function of $x$ in different bins of $Q^2$, rough electron energy recalibration method. The errors represent the statistical and systematical errors. The electron method was used with the restriction $0.05 < y < 0.55$.

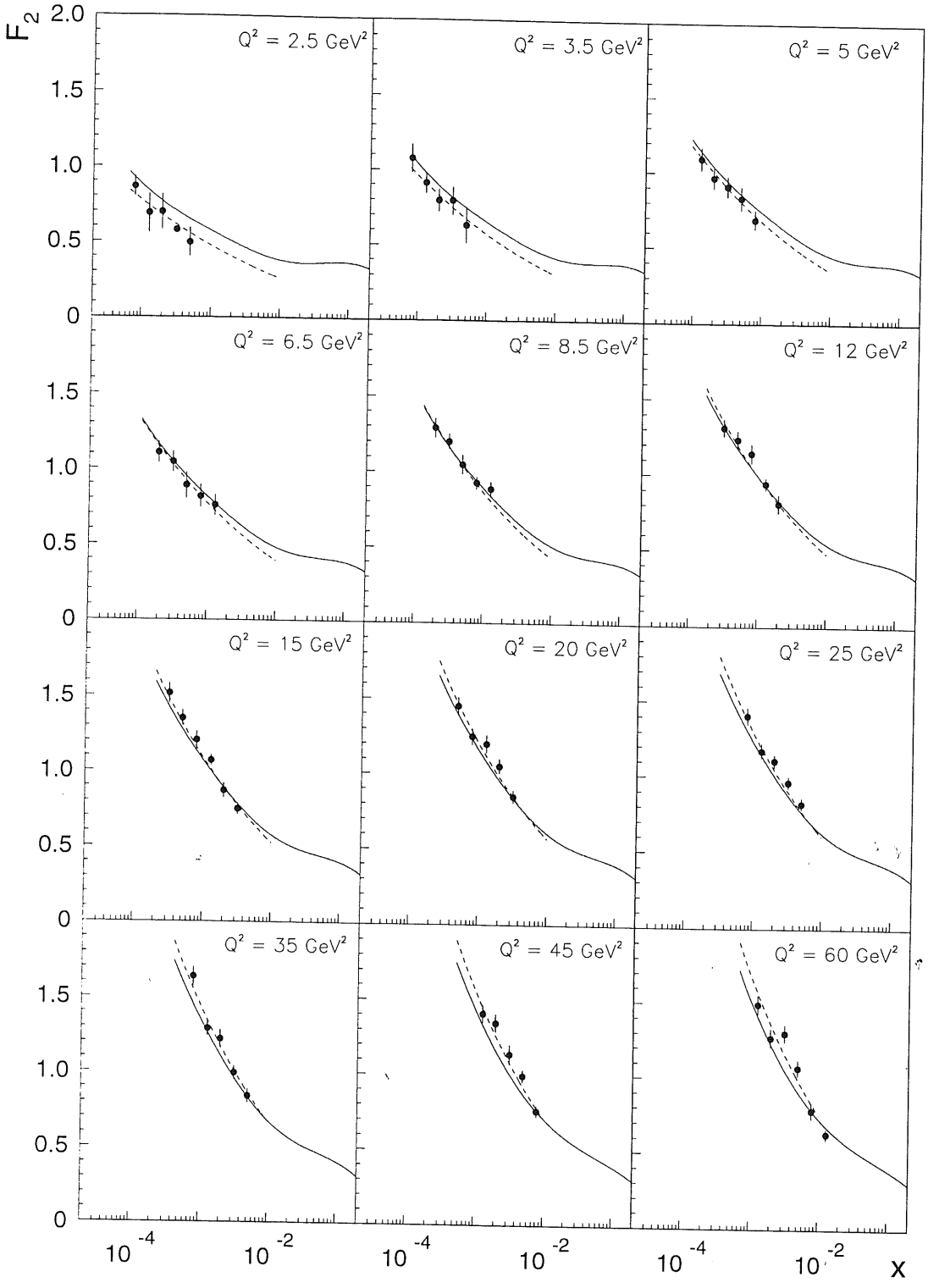


Figure 5.7: Measurement of the proton structure function $F_2(x, Q^2)$ as function of $x$ in different bins of $Q^2$, precise electron energy recalibration method. The errors represent the statistical and systematical errors. The electron method was used with the restriction $0.05 < y < 0.55$.

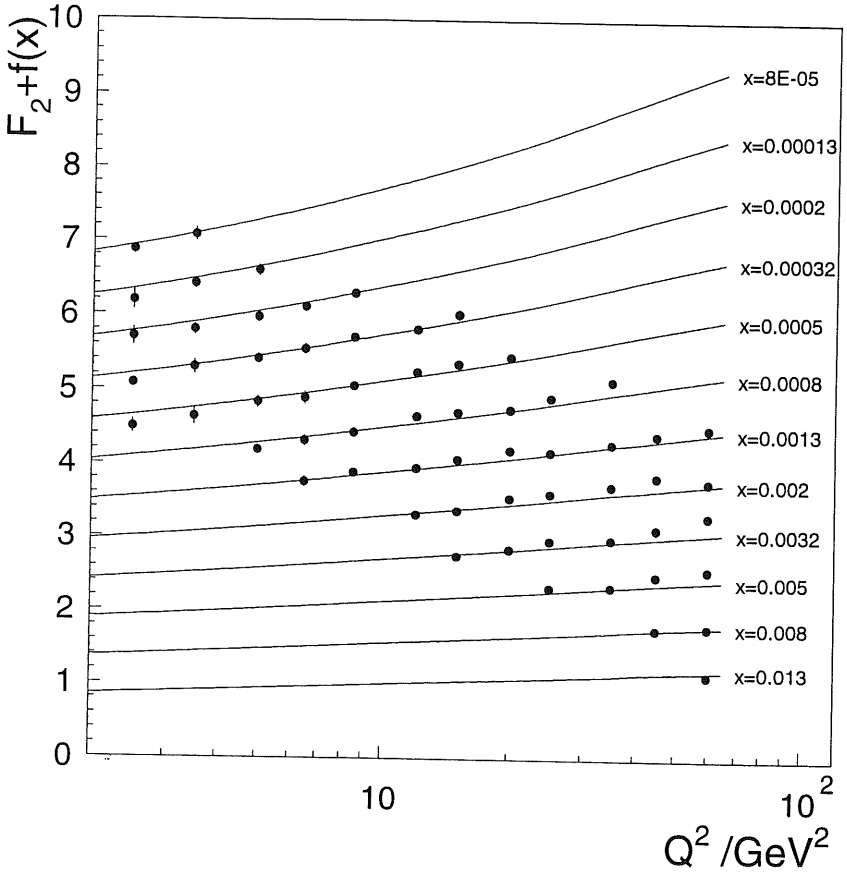


Figure 5.8: Measurement of the proton structure function $F_2(x, Q^2)$ as a function of $Q^2$ with the electron method and the restriction $0.05 < y < 0.55$. The precise electron energy recalibration method was used. A term $f(x) = i/2$ was added to $F_2$ where $i$ is the bin number starting at $i = 0$ for $x = 0.013$. Full line represents 1994 H1 fit.

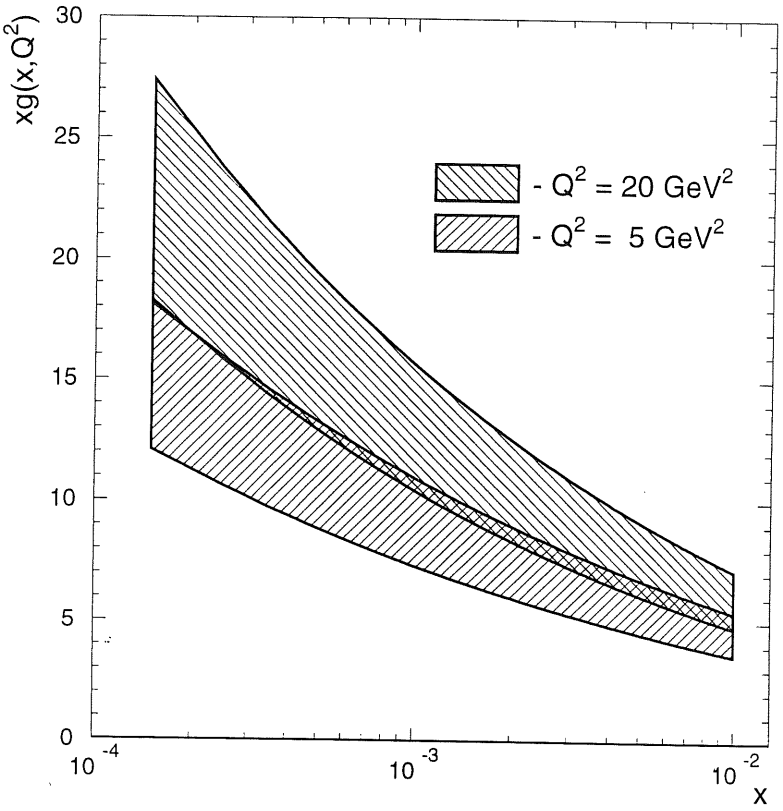


Figure 5.9: The estimate of the gluon density function at $Q^2 = 20\,\mathrm{GeV}^2$ from our fit to the measured proton structure function $F_2$.

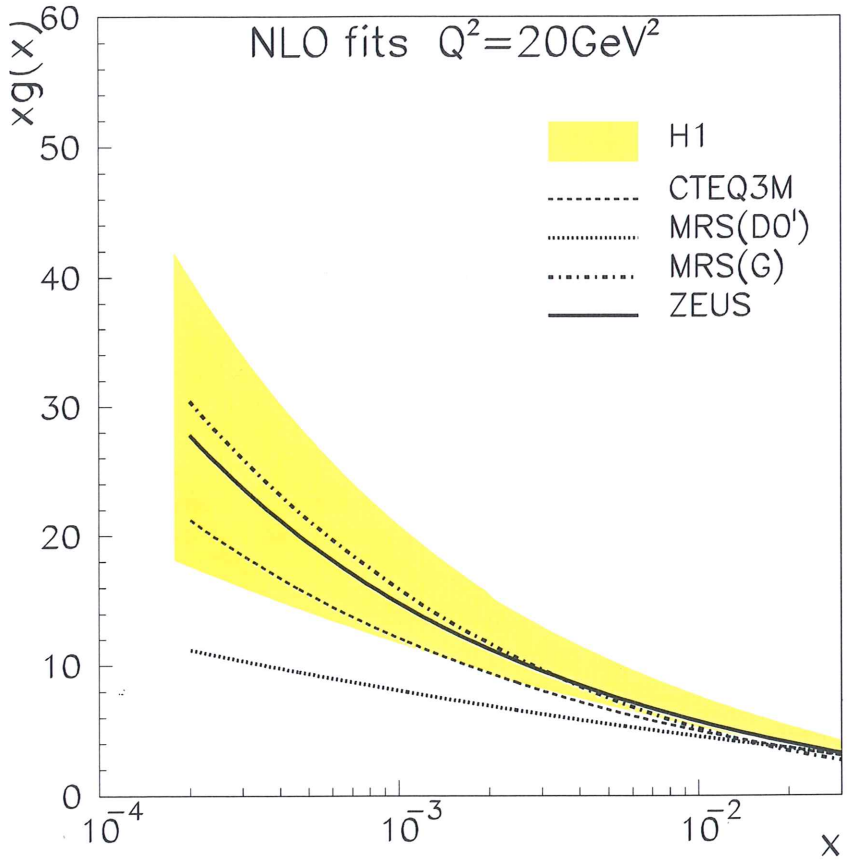


Figure 5.10: The gluon density at $Q^2 = 20\,\mathrm{GeV}^2$ extracted from a next-to-leading order QCD fit to the 1993 structure function data [26], together with the result from the ZEUS fit and the parametrisations CTEQ3M, MRSD0' and MRSG.

# Summary

A measurement of the proton structure function $F_2(x, Q^2)$ has been presented in the $Q^2$ region between 2.5 and 60 $\mathrm{GeV}^2$. The analysis used DST1 data recorded by the H1 detector in 1997 June/July and 1996 Monte Carlo simulations.

The calibration of the Spacal calorimeter by the kinematic peak method was described in detail and calibration results were presented.

The kinematic peak method was also used for the rough recalibration of DST1 data in the selected sample of events. The $\pi^0$ cross check of this calibration for low energies was performed. The more precise recalibration method was applied and results were compared with the rough one.

In order to extract the proton structure function $F_2(x, Q^2)$ we applied various cuts, with the goal to reduce photoproduction background and keep DIS events. The influence of each cut to various quantities was studied.

Monte Carlo events were reweighted in order to obtain a similar $z$-vertex distribution according to the measurement. Analysis of $z$-vertex distribution within a luminosity fill showed a very low contribution of the satellite bunches therefore their influence on the integrated luminosity was found to be negligible.

Each selected event was weighted by a weight including subtrigger prescale factors and the trigger efficiency was estimated.

The structure function $F_2(x, Q^2)$ was determined from the data with integrated luminosity 2360 $\mathrm{nb}^{-1}$ using the electron method to reconstruct the kinematic variables $x$, $Q^2$ and $y$. The results were compared with 1994 H1 measurement and showed a good agreement.

Finally, a fit to the measured structure function $F_2(x, Q^2)$ was performed in the range $10^{-4} < x < 10^{-2}$ approximately and a gluon distribution function was extracted with Prytz's approximation which is described in the thesis.

# Appendix A

# H1 performance

Since 1992, during the years of operation, HERA and consequently H1 experiment yearly increase their integrated luminosity. Summary for each year separately is shown in Figure A.1. In 1997 HERA achieved the highest increment of produced luminosity since 1992, the first year of physical running. The outline of H1 performance in 1997 is presented in Figure A.2 as a dependence of a number of quantities on luminosity fill (lumfill) number. From top: the luminosity delivered by HERA and accumulated by H1, the operational and overall efficiency, mean dead time for all runs and physics runs, number of runs per one luminosity fill and finally the average run time within a given lumfill.

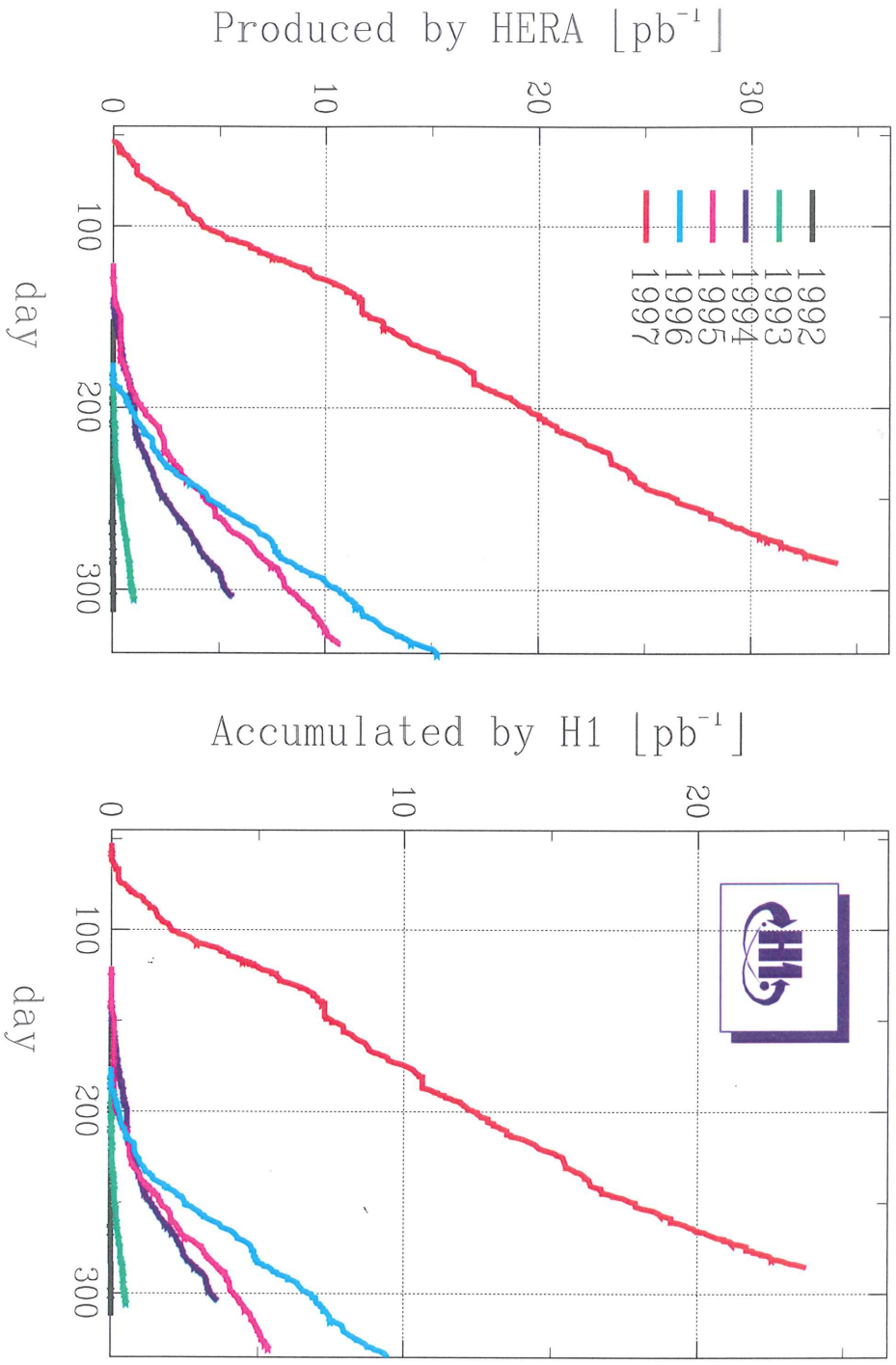


Figure A.1: Integrated luminosity produced by HERA and accumulated by H1 in 1992-1997.

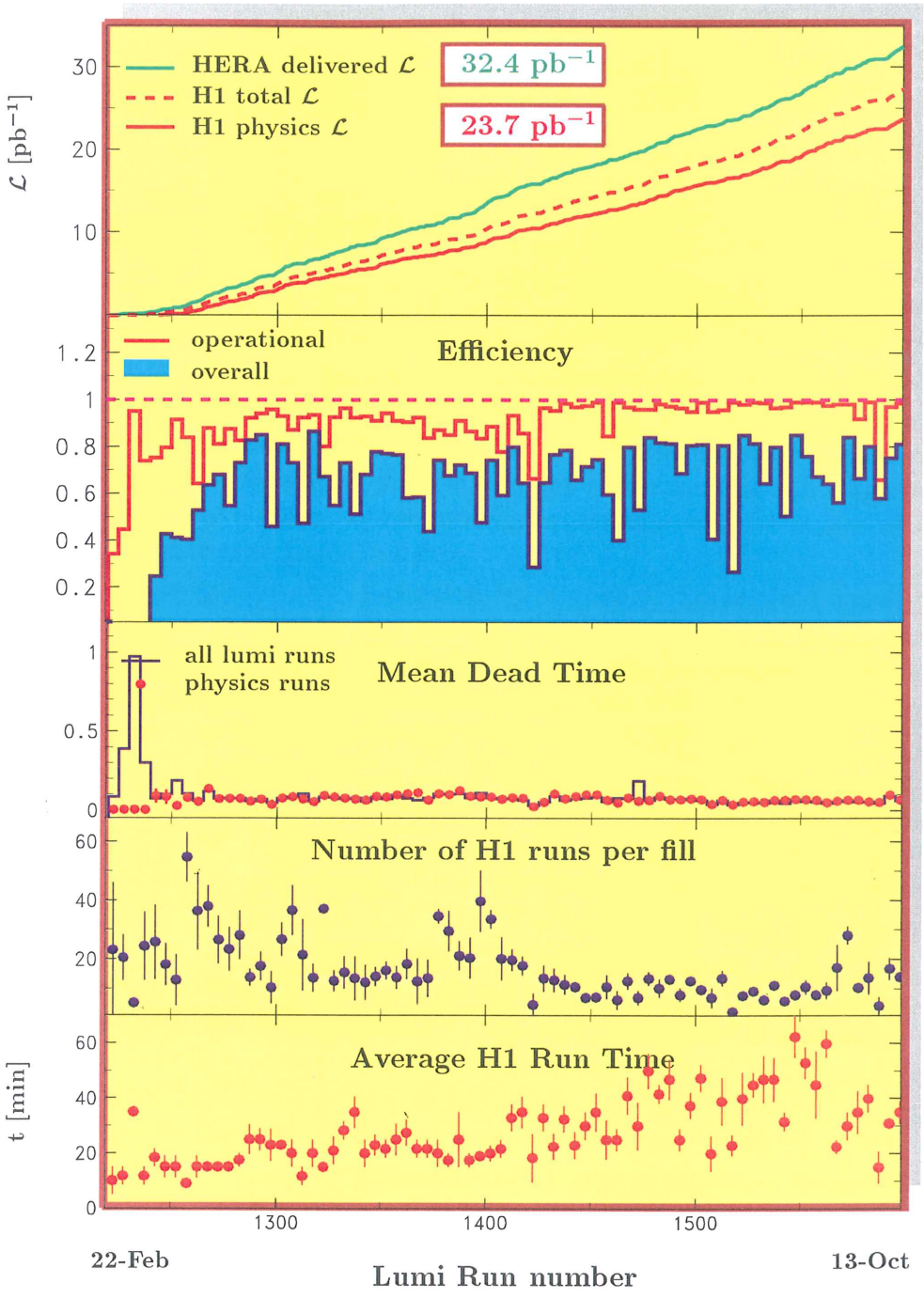


Figure A.2: H1 detector performance in 1997.

# Appendix B

# Trigger Weights

The purpose of the weighting algorithm introduced in Section 4.6 is to divide the total phase space of measured DIS interactions into non-overlapping regions with only one subtrigger assigned to each of them. Subtriggers with smaller prescale have a priority. In a weighting process only the corresponding subtrigger for each region is taken into account, other subtriggers are ignored, the weight of event is equal to the subtrigger prescale factor.

This idea is graphically illustrated by a general model in Figure B.1. A set of subtriggers (a) divides the overall phase space into a number of regions, which are covered in general by one, two or three subtriggers. The prescale factors $P()$ are ordered as follows: $P(T1) > P(T3) > P(T2)$. Application of the described selection algorithm brings division of phase space into three regions (Figure B.1 (b)) each covered by one subtrigger. Event weight is equal to the prescale factor of the subtrigger which covers corresponding region and actually triggered this event. Therefore no complicated weight calculation is needed.

The question of correctness of this method is important for regular event weight treatment. The regions of divided phase space, which correspond to a full phase space of a given subtrigger, are treated properly (e.g. trigger T2 in Figure B.1). Problems could be with subtriggers where only a fraction of its phase space coverage is employed for triggering of events. A simulation of two overlapping subtriggers was performed, results are depicted in Figure B.2. Subtrigger denoted by T1 has a prescale factor two and therefore it is prefered. The T2 subtrigger has a prescale factor three. Events were randomly generated in a phase space of both subtriggers. In a given region of overall phase space the number of reconstructed events is divided by the number of generated events and is plotted in Figure B.2 as a function of a total number of simulated events. The overall phase space of subtrigger T1 is expected to be described perfectly. A little bit worse is description of a total number of events (T1.or.T2). The worst ranges are T1.and.T2 and T2-(T1.and.T2), but their inaccuracies fall with increasing number of events.

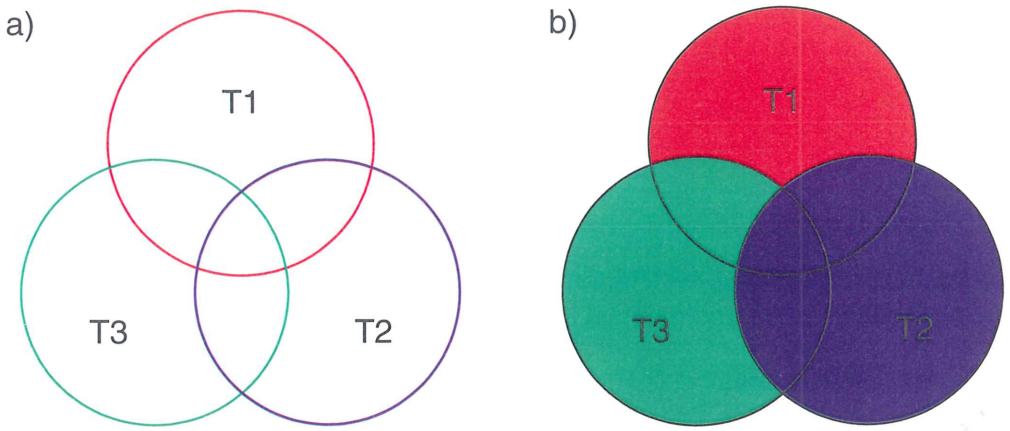


Figure B.1: The model of a set of subtriggers. The prescale factors $P()$ are ordered as follows: $P(T1) > P(T3) > P(T2)$.

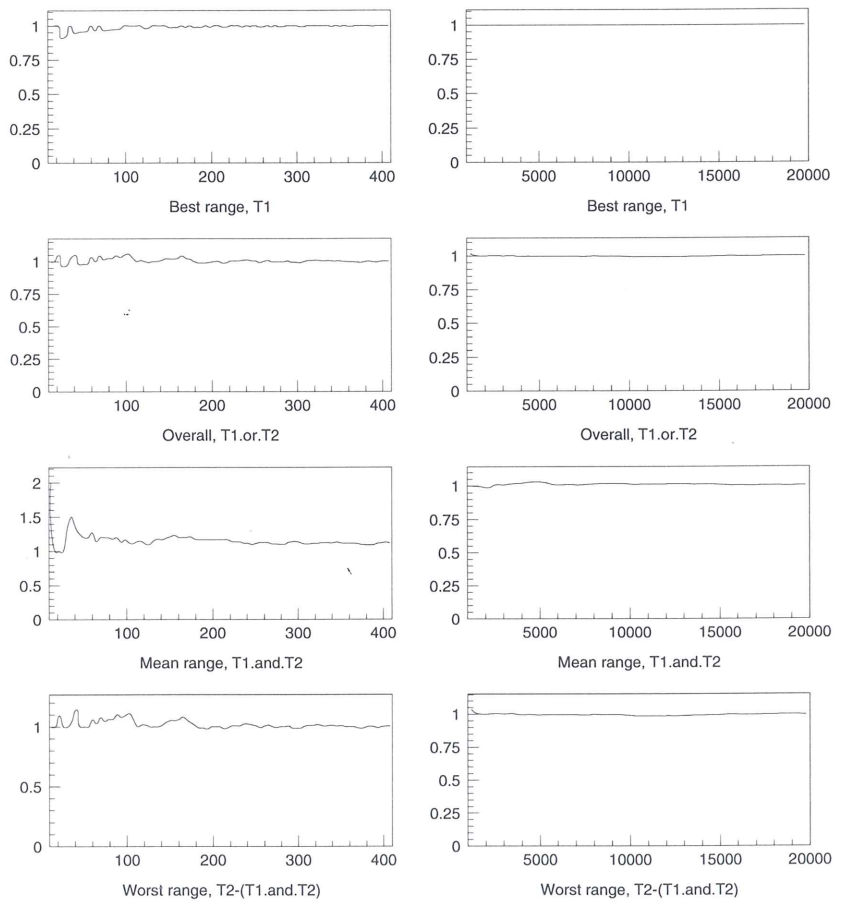


Figure B.2: Ratio between the reconstructed and the real number of events as a function of a total number of events in a simulation of weighting algorithm for two subtriggers. Rows correspond to a different areas of the phase space.

# Bibliography


[1] R.E.Taylor, Rev. Mod. Phys. **63** (1991) 573.
H.W.Kendall, Rev. Mod. Phys. **63** (1991) 597.
J.I.Friedman, Rev. Mod. Phys. **63** (1991) 615.

[2] The H1 Collaboration, *A measurement of the proton structure function $F_2(x, Q^2)$ at low $x$ and low $Q^2$ at HERA,* Nuclear Physics **B 497** (1997), 3-28.

[3] The H1 Collaboration, *A Measurement of the Inclusive Deep Inelastic ep Scattering Cross Section at Low $Q^2$ at HERA,* Submitted to the International Europhysics Conference on High Energy Physics, HEP97, Jerusalem, Israel, August 1997.

[4] S. Bentvelson, et al., *Reconstruction of $(x, Q^2)$ and extraction of structure function in neutral current scattering at HERA,* Physics at HERA.

[5] Ed. U. Amaldi, *Proc. of the study of an ep facility for Europe,* DESY 79/48 (1979), 391-394.

[6] J. Chýla, *Quarks, Partons and Quantum Chromodynamics,* Lecture notes available at *http://www-hep.fzu.cz/Theory/notes/p1997.html.*

[7] The H1 Collaboration, *A measurement of the proton structure function $F_2(x, Q^2)$,* Nuclear Physics **B 439** (1995), 471-502.

[8] K. Prytz, *Approximate determination of the gluon density at low-x from the $F_2$ scaling violations,* Physics Letters **B 311** (1993), 286-290.

[9] The H1 Collaboration, *The H1 Detector at HERA*, Nucl. Instrum. Meth. **A 386** (1997), 310-347.

[10] L. Goerlich, et al., *Strategy Studies for the H1 Topological L2 Trigger,* H1 Internal Note H1-09/97-508.

[11] A. Grueber, et al., *A Neural Network Architecture for the Second Level Trigger in H1 Experiment at HERA,* Proceedings of the IEEE Conference TAI94, New Orleans, 1994.

[12] The H1 Collaboration, *Technical Proposal to upgrade the Backward Scattering Region of the H1 Detector,* DESY PRC 93/02.

[13] H1 Spacal Group, *The H1 Lead/Scintillating Figer Calorimeter* Nucl. Instrum. Meth. **A 386** (1997), 397-408.

[14] H1 Spacal Group, *Series of Tests of Fine Mesh Photomultiplier Tubes in Magnetic Fields of up to 1.2 Tesla,* DESY-97-070 (1997).

[15] H1 Spacal Group, *The LED based Calibration System of the H1 Lead/Scintillating-Fiber Calorimeter,* to be submitted to Nucl. Instr. Meth.

[16] V. Boudry, et al., *The Inclusive Electron Trigger for the SPACAL: Design and CERN-test Results,* H1 Internal Note H1-03/95-430.

[17] M.Dirkmann, H1 Internal Note H1-05/96-477.

[18] A. Meyer, *Measurement of the Structure Function $F_2(x, Q^2)$ of the Proton at Low $Q^2$ with the H1 Detector at HERA Using the New Detector Components Spacal and BDC,* Dissertation, Hamburg, 1997.

[19] J. Janoth, et al., *An Algorithm to Calibrate the New H1 Backward Calorimeter "Spacal" using the Kinematic Peak,* H1 Internal Note H1-11/95-464.

[20] A. Meyer and J. Zálešák (Spacal group) private communication

[21] J. Zálešák, private communication

[22] A. A. Glazov, *Measurement of the Proton Structure Functions $F_2(x, Q^2)$ and $F_L(x, Q^2)$ with the H1 Detector at HERA,* Dissertation, Berlin, 1997.

[23] J. Riedlberger, *The H1 Trigger with Emphasis on Tracking Triggers,* H1 Internal Note H1-01/95-419.

[24] S. Egli, et al., *Calculating Event Weights in case of Downscaling on Trigger Levels 1-4,* H1 Internal Note H1-04/97-517.

[25] A. A. Glazov, private communication

[26] The H1 Collaboration, *The gluon density of the proton at low x from QCD analysis of $F_2$,* Physics Letters **B 354** (1995), 494-505.

## Acknowledgments

I would like to address special thanks to Josef Žáček[1] supervisor of my diploma thesis for his stimulating interest during the preparation of this thesis and for the possibility of my participation at the H1 experiment. The work in ELAN and SPACAL groups has been a rich and unique experience for me.

Thanks also to Jaroslav Zálešák and Andreas Meyer from SPACAL group for their valuable comments and discussions.

Separately I would like to express my gratitude to Alexandre A. Glazov[2] for his advise and support especially during my presence in IfH Zeuthen, Berlin.

I am indebted to Petr Reimer[3] for many fruitful discussions and comments related (not only) to the analysis of the proton structure function. Together with Josef Žáček he has also helped me to correct the embarrassment in the text of this diploma thesis.

I wish to thank many members and participants of the H1 collaboration, namely M. Klein, M. Taševský, J. Hladký, J. Cvach, J. Chýla, K. Sedlák, V. Arkadov and many others, whose encouragement and support was very valuable for me.

My one month visit at DESY was supported by the grant Foundation of Czech Universities No. 1278 and three one week visits were enabled by the grants GAUK 177/96 and GAČR 202/96/0214. These stays gave me an opportunity to present the results at the SPACAL and ELAN meetings.

The computations were carried out on the Sun work group server *vaigach* (DESY, Hamburg), Silicon Graphics stations *Indigo Entry* and *Indy R5000* (NC[1], Prague) and mainly on the SGI Power Challenge machines *hydra* (IfH, Zeuthen[2]) and *dice2* (DESY, Hamburg).

Finally, I would like to thank my family for the steady support I felt during all my study at Charles University and especially in the time of making this thesis.

[1]Nuclear Center, Charles University, Prague, Czech Republic
[2]DESY, Institute für Hochenergiephysik, Zeuthen, Germany
[3]Institute of Physics, Academy of Sciences of the Czech Republic, Prague